# CHAPTER SIX

## THE CORRELATION OF CRYSTALLOGRAPHY WITH THE RETENTION OF AUSTENITE IN LOW-ALLOY STEELS

### (VI.1) Introduction

The most obvious feature of a martensite transformation is the change in shape, or shape deformation, which reveals itself in the form of a well defined surface distortion when a pre-polished crystal of austenite is allowed to transform to martensite. This macroscopically homogeneous shear strain will induce a large shear stress in the surrounding austenite; there will also be hydrostatic stresses due to the volume expansion or contraction accompanying the change in crystal structure during the martensite transformation.

In addition to the elements that characterise the shape deformation, a habit plane which is the interface plane between the austenite and martensite can also be identified. The induced shear stress in the austenite can be resolved with respect to further potential martensite habit plane variants, enabling the prediction of the most likely martensite plates which can form by optimum coupling with the induced stress system. In this respect, the operative stress system surrounding a martensite plate can be assumed to be disc shaped (108) so that those plates which form with their respective habit plane variants as parallel to each other as the crystallography concerned will allow, while at the same time minimising the total shape deformation involved, will have optimum coupling between their stress fields, thus resulting in a minimisation of strain energy. The autocatalytic burst phenomenon in certain martensite transformations is essentially a manifestation of such coupling.

The role of strain energy in the martensite transformation is clearly critical - indeed, the various features of the transformation can be predicted on a self consistent basis by the principle of strain energy minimisation (57,109). This is also reflected in the general application of the Bain correspondence in the phenomenological theory of martensite. This correspondence is by no means a unique correspondence between the austenite and martensite lattices but appears to be the one involving the minimum displacement of atoms during the transformation. In physical terms the role of strain energy is easy to understand when it is realised that the extent of

the shape deformation strain can be orders of magnitude greater than the local strain arising due to the residual stresses at a dislocation pile-up (108).

It should be noted that if the induced stresses in the austenite reach a magnitude greater than the local flow stress, plastic relaxation must follow. Indeed, it has been shown that the agreement with theory is optimum when account is taken of both the elastic and plastic components of strain (57).

It is clear that the ease of formation of martensite and conversely, the difficulty of retaining austenite will depend to some extent on the strain situations involved. The latter is a function of the martensite crystallography, and it was with this in mind that the present work was undertaken.

## (VI.2) Theoretical Considerations

The prevalent orientation relationships describing the austenite and martensite disposition after transformation can be listed as follows:

| | | |
|---|---|---|
| Kurdjumov-Sachs (KS) | $(111)_\gamma$ // $(011)_{\acute{\alpha}}$<br>$[\bar{1}01]_\gamma$ // $[\bar{1}\bar{1}1]_{\acute{\alpha}}$ | Reference 110 |
| Greninger-Troiano (GT) | $(111)_\gamma$ 0.2° from $(011)_{\acute{\alpha}}$<br>$[\bar{1}01]_\gamma$ 2.7° from $[\bar{1}\bar{1}1]_{\acute{\alpha}}$ | Reference 111 |
| Nishiyama-Wasserman (NW) | $(111)_\gamma$ // $(011)_{\acute{\alpha}}$<br>$[1\bar{1}0]_\gamma$ // $[100]_{\acute{\alpha}}$ | Reference 112 |

The KS and NW relationships are related by a rotation of 5.26° about the $[0\bar{1}1]_{\acute{\alpha}}$ axis. At first sight this appears to be a very small difference, but it will be shown later that it has a profound influence on the martensite-martensite crystallography.

The GT relationship generally refers to BCT martensite, but can also be found with FCC to BCC transformations (113).

Considering the KS orientation relationship first, we note that 24 independent crystallographic variants of martensite can be obtained within a single crystal of austenite. These are listed in table VI.1. The KS relationship has the special property that its variants can be twin related in pairs (114). Speich and Swann (115) elegantly illustrated that six independent variants can be obtained simply by rotation about the pole of

$(011)_{\alpha'}$ // $(111)_{\gamma}$, fig.VI.1. Hence, a group of six variants can be assigned to each of the four independent $\{111\}_{\gamma}$ planes in a given austenite crystal, (table VI.1), thereby generating the 24 variants. Using the terminology of table VI.1, Speich and Swann (115) listed the axis-angle pairs required to obtain variants (2-6) from variant (1) and showed that these could be divided into three pairs of twin-related variants. However, they did not consider the 18 other variants so that it is not known whether additional twin related variants might arise by choosing pairs of KS variants airsing from different groups, as listed in table VI.1. It is important to resolve this problem since it will be shown later that the formation of twin-related variants may be significant to the retention of austenite. The relationships between all 24 variants of KS were computed using Euler's theorem, as quoted in (116).

Euler's theorem states that any displacement of a rigid body which leaves one of its points fixed may be produced by a rotation of the body through an angle of 180° or less about an axis passing through that point. Letting the position of the body be specified by the position of the fixed point "O" and two other points "P" and "Q", such that O,P and Q are not colinear, the initial and final positions of these points (the latter being generated by the rotation operation) can be defined as $O,P_1,Q_1$ and $O,P_2,Q_2$ respectively such that

$$OP_1 = \underline{p}_1$$
$$OQ_1 = \underline{q}_1$$
$$OP_2 = \underline{p}_2$$
$$OQ_2 = \underline{q}_2$$

Euler's theorem then gives

$$\frac{(\underline{q}_2 - \underline{q}_1) \times (\underline{p}_2 - \underline{p}_1)}{(\underline{q}_2 + \underline{q}_1) \cdot (\underline{p}_2 - \underline{p}_1)} = \hat{\underline{u}}(\tan[\xi/2])$$

where $\hat{\underline{u}}$ is a unit vector parallel to the axis of rotation, and $\xi$ is the amount of rotation about the axis $\hat{\underline{u}}$.

Considering variant (1) in table VI.1 as the reference variant and assuming that we wish to obtain the axis-angle pair relating variants (1) and (12), we have

| | | |
|---|---|---|
| $(011)_{\alpha_1}$ // $(111)_{\gamma}$ | $[\bar{1}\bar{1}1]_{\alpha_1}$ // $[\bar{1}01]_{\gamma}$ | Variant (1) |
| $(011)_{\alpha_{12}}$ // $(\bar{1}\bar{1}1)_{\gamma}$ | $[1\bar{1}1]_{\alpha_{12}}$ // $[011]_{\gamma}$ | Variant (12) |

However, before Euler's theorem can be applied, both sets of indices must have a common reference frame, and for the present purposes the indices of variant (12) may be transformed to those of variant (1) via the common austenite lattice. Using the KS relationship**, we find that the $(\bar{1}\bar{1}1)_\gamma$ plane which lies parallel to the $(011)_{\acute{\alpha}12}$ is also parallel to $(-.0865\ -.8996\ .4282)_{\acute{\alpha}_1}$ and similarly, $[1\bar{1}1]_{\acute{\alpha}12}$ corresponds to $[-.5244\ .4065\ .7482]_{\acute{\alpha}1}$.

$$**(hkl)_\gamma = (hkl)_{\acute{\alpha}} \begin{vmatrix} .90825 & -.81650 & -.09175 \\ .79588 & .90825 & -.20412 \\ .20412 & .09175 & 1.20413 \end{vmatrix}$$

$$(hkl)_{\acute{\alpha}} = (hkl)_\gamma \begin{vmatrix} .60550 & .53058 & .13608 \\ -.54433 & .60550 & .06117 \\ -.06117 & -.13608 & .80275 \end{vmatrix}$$

Thus,

$$\underline{p}_1 = 0,1,1 = 0,\ .7071,\ .7071$$
$$\underline{q}_1 = -1,-1,1 = -.5774,\ -.5774,\ .5774$$
$$\underline{p}_2 = -.0865,\ -.8996,\ .4282$$
$$\underline{q}_2 = -.5244,\ .4065,\ .7482$$

and Euler's theorem can be applied to yield the result given in table VI.2. From table VI.2 it is clear that twin related variants cannot be obtained by choosing variants from different groups.

Considering the NW orientation relationship next, an examination of fig. VI.2 immediately reveals that twin-related variants of NW cannot arise. This follows from the fact that the $\{001\}_{\acute{\alpha}}$ poles of a BCC matrix coincide with poles of the $\{122\}_{\acute{\alpha}_t}$ form in the BCC twin. In the NW orientation relationship an $\{001\}_\alpha$ is parallel to an $\{011\}_\gamma$ but there is no $\{122\}_{\acute{\alpha}}$ pole also parallel to another $\{011\}_\gamma$ so that twin related martensite variants are impossible. In fact, figure VI.3 shows that the slightest departure ($\beta$) from parallelism of close packed directions (while maintaining parallelism of closest packed planes) leads to a condition where twin related variants cannot arise. A similar conclusion applies to the GT orientation relationship and we can conclude that no orientation relationship in the Bain orientation region other than KS can lead to the formation of twin related variants of martensite.

Having established the crystallographic necessities, some of the work given below is based on the hypothesis that the formation of twin related variants involves a high degree of mutual accommodation, such that the propensity to retain inter-lath

films of retained austenite is reduced. It will become evident (from the work to be presented below, and from the results of Ch.7) that this hypothesis is firmly based. Moreover, Kelly (117) examined alpha martensite in a high alloy stainless steel and found that the observed crystallographic elements are consistent with twin related laths having shear components of their shape strains that can cancel each other (assuming that the high value of the dilatation parameter he used can be justified).

## (VI.3) The Distribution and Stability of Inter-Lath films of Retained Austenite

In recent years, the study of retained austenite films associated with martensite in low alloy steels has assumed new significance, primarily due to its apparent influence on the mechanical properties of commercially used quenched and tempered ultra-high strength steels (75,92,118). Due to the relatively high $M_s$ temperatures of low alloy martensites, only thin films of inter-lath austenite are retained at room temperature (thickness ~500 Å, ref.107). However, the reasons for the lack of complete transformation are not clear - even cooling to -196°C often fails to finish the transformation (119, Ch.5). Since the films of austenite are, in general, found to be stable even in the thin foils used in transmission microscopy, the problem cannot simply be attributed to constraint effects, although these clearly do have some role (Ch.5).

Since refrigeration fails to give a significant decrease in the amount of retained austenite, Rao et. al. (119) proposed that chemical or thermal stabilisation could be ruled out as possible reasons for the anomalous stability of these films. As far as chemical stabilisation is concerned, we do not expect any partitioning of carbon when martensite is formed by directly quenching from the austenitised condition, since the transformation products reach ambient temperature in a very short period of time. The Mossbauer spectroscopy results of Azevedo and Da Silva (106) confirm that enrichment of austenite does not occur during the quench. In view of these factors, and by a process of elimination, it is thought that mechanical stabilisation could be responsible for the stability of the austenite films (119). The purpose of the present work was to examine this possibility and a number of steels were investigated.

(i) Fe-0.4C-4.0Ni

A microstructure of dislocated lath martensite was obtained on water quenching following austenitisation at 1200°C for 10 min. Examination of over 60 electron micrograph/diffraction pattern pairs revealed that approximately 55% of adjacent martensite units had twin related lattices. The structure appeared to be partitioned by large platelets, with finer martensite in the partitioned areas (figure VI.4). The twin related martensite was found mainly in the partitioned regions and occurred in two distinct formations. In one situation, the adjacent platelets alternated in twin orientation and formed as clearly defined packets and it was found that retained austenite could not be imaged within these regions (figure VI.5). When irregular groups of platelets with only some adjacent martensite units being twin related were observed, retained austenite could be imaged between units in the same crystallographic orientation but only to a very limited extent at the interfaces between twin related units (figure VI.6).

In all cases the retained austenite films were rather discontinuous and it is estimated that the quantity of retained austenite involved is less than 1% . The inhomogeneous distribution of retained austenite can be rationalised if it is considered that the twin related martensite units form in a mutually accommodating manner. In this case, mechanical stabilisation of austenite (which essentially involves the jamming of the austenite-martensite interface by accommodation defects) is expected to be mitigated relative to the situation where adjacent variants form in the same crystallographic orientation, when their shape deformations would be expected to be additive rather than mutually compensating**.

---

** When the laths constituting a packet are in the same orientation, it is likely that the shape deformation of each unit within the packet is identical. There is only one case where the habit plane and orientation relationship of adjacent units can be the same, and yet the shape deformations involved can be different. This occurs in the FCC to HCP transformation where a degeneracy exists so that the operation of any one of a set of three Shockley partials on a given $\{111\}_\gamma$ habit plane generates the HCP lattice. Irrespective of which of the three partials operates, the final lattice obtained will be crystallographically indistinguishable, except for the shape deformation (61). No such degeneracy exists for the FCC to BCC transformation.

Clearly, the compensating effects would be maximised when the twin related platelets can form in regular groups with alternating units. The formation of twin related variants in the regions partitioned by the larger platelets is consistent with the above arguments since such regions would be under the constraint of an already formed rigid frame of martensite. This last point is illustrated in figure VI.7, which is a surface relief image of a pre-polished and transformed specimen (taken using scanning electron microscopy). We notice that the total surface relief is minimised in the regions partitioned by the larger units.

(ii) Fe-0.18C-3.9Mo

Considerable quantities of inter-martensite retained austenite films could be imaged and it was found that the martensite platelets tended to be in the same crystallographic orientation in space (over distances of approximately 10 martensite units at least ), figure V.2. It is probable that very little mutually compensating accommodation is involved in the formation of such groupings so that the residual austenite would be deformed to a greater extent by the resultant unaccommodated strains. This could lead to mechanical stabilisation. However, the films of retained austenite proved to be too fine to be able to easily characterise their microstructure.

(iii) Fe-0.08C-1.1Mn-0.2Si-5.5Ni-14.5Cr-2.1Mo-0.7Nb-1.9Cu

With this alloy the martensite groups again formed in the same crystallographic orientation and the high alloy content allowed the retention of larger quantities of austenite (fig.VI.8). The microstructure of this austenite could be clearly resolved and it was interesting to note that the austenite was heavily faulted, with a dominant fault plane aligned with respect to the martensite habit plane trace, as expected when the austenite absorbs a significant proportion of the accommodation strain. Such extensive faulting can be expected to mechanically stabilise the residual austenite to further transformation.

(iv) Fe-0.31C-2.0Si

Since retained austenite could not be detected after direct quenching, an attempt was made to enhance the retention of austenite by thermal stabilisation. The specimen was austenitised at 1100°C for 5 min followed by a quench to 335°C (a temperature below the calculated $M_s$ of 410°C) where it was held for 1 hour before finally quenching to room temperature. However, retained austenite

could not be detected and it was found that the martensite was in classical lath formation (figure VI.9) with alternate laths being twin related. The lath packets were extremely regular, as illustrated in figure VI.10. These results are again consistent with twin related martensite forming in a mutually compensating manner.

The above results are consistent with mechanical stabilisation being the operative mechanism for the problem at hand, but more direct evidence for the high degree of mutual accommodation between twin related martensite variants can be offered for the Fe-0.4C-4Ni alloy.

In chapter seven it will be demonstrated that the incipient twinning found in mainly dislocated low alloy martensites arises from accommodation effects. Such twins are not intrinsic transformation features. These kinds of twins can also be found in the Fe-0.4C-4Ni alloy. However, it is clear from figure VI.11 that the intensity and distribution of twinning depends critically on the local crystallography. In fig. VI.11, the twinning is extensive when adjacent units are twin related but is absent in the case of the laths marked 'A' and 'B' which are in the same crystallographic orientation. The nucleation of accommodation twinning and the transfer of slip across inter-lath boundaries would certainly be easiest when the adjacent lattices are twin related; this increases the scope for mutual accommodation. Additionally, it is hard to imagine how any retained austenite could exist between twin related laths when it is clear that their lattices are effectively interpenetrating because the twins nucleate in the same orientation as the adjacent lath. This matter will be dealt with in greater detail in chapter seven.

## (VI.4) The Crystallography of Dislocated Martensites

In order to understand the operative deformation systems, accommodation modes and various other factors controlling the extent of transformation to martensite, it is necessary to completely define the crystallography with respect to the phenomenological theory of martensite. While it is noted that for ferrous martensites the theory provides fully satisfactory agreement in only a few cases, the elegance of such precise agreement despite the blatant complexities involved points towards the underlying truths of the theory.

Detailed comparison between experiment and theory requires a self consistent analysis involving more than just the prediction of the habit plane indices (120). However, the lack of adequate quantities of retained austenite in low alloy steels has rendered the determination of such data difficult, if not impossible. The following is a brief review of the available data on the habit plane of dislocated martensite.

(i) The Habit Plane of Dislocated Martensite - A Review

In 1929 Sauveur and Chou (121) identified the habit plane of martensite obtained by quenching 'pure' iron as $\{111\}_\gamma$, simply by comparing the optical microstructure with that of Widmanstätten ferrite. However, it is now established that far greater quench rates are necessary to obtain martensite in pure iron. In 1933 Mehl et. al. (122) found the $\{111\}_\gamma$ habit plane in quenched steels with carbon contents of 0.4-1.3 wt. pct. using single surface trace analysis (optical microscopy). The results are doubtful since it is now known that high carbon steels do not have a $\{111\}_\gamma$ habit plane. Mehl and Smith (123) quenched pure iron from 1300°C into a high pressure radial jet of water and identified the habit plane of the resulting martensite by two surface analysis (optical microscopy) to be $\{111\}_\gamma$. Greninger and Troiano (124) conducted a single experiment on a 0.35C steel and found a $\{111\}_\gamma$ habit plane using the method of twin band vestiges, which relies on the 'ghosts' of prior austenite twins to establish the austenite orientation. Wayman et. al. (125) fast quenched zone refined iron and showed that the relative angles of surface markings, as observed by optical microscopy, were consistent with a $\{111\}_\gamma$ habit plane although a pseudo $\{111\}_\gamma$ habit was not ruled out. The latter concept was first introduced by Bowles (126) and implies that the habit plane is in fact comprised of martensite needles which are parallel to directions of the form $\langle 10\bar{1}\rangle_\gamma$ within a given $\{111\}_\gamma$ plane. He further suggested that the transformation in low carbon steels is characterised by the degeneration of $\{225\}_\gamma$ martensite plates into needles. Kelly and Nutting (127) examined the morphology of martensite in several steels by means of thin film electron microscopy, and found martensite 'needles' parallel to $\langle 101\rangle_\gamma$ directions. Such pseudo-habits may exist in some cases (although confirmatory evidence would be useful), but genuine plates with a $\{111\}_\gamma$ habit must also exist (61).

A criticism that is common to all of the above work is that it fails to take account of the possibility that the lath and packet planes (as observed by optical microscopy) may differ.

Lagneborg (128) characterised the habit plane of lath martensite in 18Cr-8Ni-Fe alloys as $\{225\}_\gamma$. However, Kelly (129) subsequently criticised the crystallographic precision of this work and showed that the habit plane is in fact $\{112\}_\gamma$, using a pseudo-two surface analysis coupled with self consistent crystallography. The results of Kelly were obtained using transmission electron microscopy, and he further demonstrated that the data was consistent with the phenomenological theory of martensite (although a dilatation parameter of 1.8% had to be used).

Bell and Owen (130) implied that since the martensite plates obtained in Fe-N alloys were arranged in a Widmanstätten pattern, they could have formed by shear on $\{111\}_\gamma$ planes. Using single surface trace analysis and electron diffraction, Biswas and Codd (131) claimed that the lath habit in low nitrogen ferrous martensites could be characterised as the $\{110\}_{\alpha'}$ plane, consistent with the observation of (130) if a KS or NW orientation relationship is operative. The shortcomings of single surface trace analysis will be dealt with later, but it is clear that both of the above pieces of evidence are weak.

Schoen et. al. (132) transformed a large single crystal of Fe-Ni containing a nickel concentration gradient so that the transformation terminated at some point where the driving force became inadequate. At this point the martensite laths were embedded in austenite and three surface analysis proved that the unit of 'massive' martensite was a thin platelet with a habit plane within 3° from $\{111\}_\gamma$. It should be noted that the martensite unit concerned here is physically much larger (optically resolvable) than the 0.3μm width laths observed in the more common dislocated martensite found in low alloy steels. Byrans et. al. (133) found that the habit plane of 'massive' martensite in an Fe-22Ni alloy was near $\{111\}_\gamma$. This conclusion arose from the fact that the inter-lath angles measured always fell in a domain specified by the assumption of a $\{111\}_\gamma$ habit plane.

From electron microscopic analysis, McDougall (134) found that an Fe-24Ni-0.1C alloy had a structure of laths with habit planes

parallel to $\{111\}_\gamma$. However, Chilton et. al. (135) obtained a habit plane near $\{123\}_{\acute{\alpha}}$ for Fe-24Ni-0.1C, Fe-4Ni-0.05C and Fe-20Ni-0.03C alloys, using single surface trace analysis based on electron diffraction. These results are incompatible if it is assumed that the operative orientation relationship lies at or between KS and NW.

Bozic and Lucic (136) examined Fe-(0.22-1.68)As alloys, again by a single surface trace analysis/electron diffraction technique, and claimed clustering of the habit plane pole in the vicinity of $\{110\}_{\acute{\alpha}}$. They further considered that there was no systematic variation of habit plane pole with composition; this conclusion is unjustified since the technique cannot resolve such variations.

Similarly, Sarma et. al. (137) examined Fe-5Ni-0.5C, Fe-24Ni-2Mn and Fe-20Ni-6Ti alloys and claimed that the habit plane was $\{123\}_{\acute{\alpha}}$ in each case. These results can be severely criticised since they used only four sets of data (i.e. four great circles, each representing the locus of the habit plane pole on the stereogram) per alloy and it can be readily shown that their data is compatible with other possibilities. Furthermore, their interpretation that the $\{123\}_{\acute{\alpha}}$ habits could have arisen from either the $\{345\}_\gamma$ or $\{557\}_\gamma$ planes (depending on the orientation relationship) is confusing since this does not agree with the Bain correspondence.

Bolton and Petty (138) assumed that the habit plane of an Fe-Mn alloy martensite is $\{110\}_{\acute{\alpha}}$ by observing that the trace of the lath habit plane was parallel to that of ghosts of austenite twins; the lath traces were also parallel to the K2 twin plane on either side of the twin boundary.

In summary, it seems that the existence of a $\{111\}_\gamma$ habit plane in low alloy dislocated martensite has not been definitively demonstrated, particularly for carbon containing martensites. In some cases where the habit has been accurately identified to be near $\{111\}_\gamma$, the martensite is 'massive', and not representative of low alloy dislocated martensite in general.

(ii) Techniques for the Determination of Habit Planes

(a) The Significance of Habit Plane Multiplicity

The multiplicity of the form of the habit plane defines the number of independent habit plane traces observable in any given austenite grain. This kind of an analysis can only be used as a definitive method if the observed multiplicity uniquely

corresponds to a particular form of planes. An example would be the $\{111\}$ planes which are the only planes with a multiplicity of 8 in a cubic system. When optical microscopy is used, the observed multiplicity may be lower than the actual value if the habit plane lies sufficiently near a plane of low order, such that the difference cannot be resolved.

Considering further the example of the $\{111\}_\gamma$ plane, it should be noted that the observation of more than four independent traces rules out a $\{111\}_\gamma$ habit; however, when the observed multiplicity is less than four, this possibility cannot be discounted since there is no reason why all habit plane variants need be operative.

The above analysis is conditional on the existence of only one transformation product (or an easily distinguishable one) with a unique habit plane.

(b) The Measurement of Inter-Trace Angles

This method of defining the habit plane using optical microscopy was put forward by Crocker et. al. (139) and is limited to cases where the habit plane indices are of a low order. It involves the measurement of inter-trace angles formed in the arbitrary plane of section that intersects a set of three independent habit plane variants. Should all the measured angles fall within a domain specified by the indices of the postulated habit, the latter is confirmed. For best results, a sufficient number of critically distributed (eg. with respect to the domain boundaries) situations should be examined.

It was decided to extend the method so that the general case can be examined, bearing in mind that while conclusive results may not be obtained for complex cases, it may be useful to show that the measured angles are consistent with the postulated habit plane. The essentials of the method are presented in figure VI.12, and it should be noted that if the habit plane is known, the method can be iteratively used to calculate the plane of section.

(c) Two Surface Analysis

If the crystallographic orientation of the austenite is known, the observation of traces of the habit plane on two independent surfaces can yield accurate and unique habit plane data. When sufficient austenite is not retained (as is the case for most low alloy steels), the ghosts of prior austenite twins can be used to establish the austenite orientation. Even when the

austenite orientation cannot be determined, two surface analysis can be used to generate a set of data composed of the angles between habit plane variants. If sufficient data of this nature is accumulated, the habit plane indices can be iteratively determined by comparison with the set of angles produced between all 24 (maximum) variants of planes of the form $\{hkl\}_\gamma$, where $\{hkl\}_\gamma$ would be systematically varied (on a computer) until a match is obtained.

(d) Trace Normal Analysis using Electron Diffraction

Only a brief description of this technique is warranted since it is well established and is found in most standard textbooks on applied electron microscopy. The data obtained from electron diffraction and direct imaging are plotted as great circles on a convenient stereographic projection. The great circles represent the loci of the possible positions of the habit plane normal so that their common intersection point (after rotation into a unit stereographic triangle using symmetry operations) gives the actual habit plane normal. The purpose of the present section is to point out certain factors that can lead to misinterpretation and to further develop the method of analysis.

The technique is at its best when the great circles cover a fair range of orientations and are not just repetitive. However, most metallurgical samples are textured, and care must be exercised to avoid the clustering of great circles. When tilting is used, serious errors can arise (140) if the trace measurements are not corrected for projection effects. When a straightforward electron diffraction technique is used, it must be realised that the zone axis can deviate considerably ($\sim 5°$) from the electron beam direction, and care must be taken to use symmetrical diffraction patterns wherever possible.

The method becomes most difficult to interpret when the habit plane is irrational, as is the case for most ferrous martensites. This is because it requires the experimenter to spot the pole which is common to all the great circles, and often the pole concerned may not even be denoted on standard stereograms. In order to partly overcome these difficulties, a computer method was developed which allows the systematic testing of the experimental data such that the total amount of scatter of the great circles from the postulated habit plane pole is minimised. The additional advantage of this procedure is that all stereographic plotting errors are eliminated and the analysis becomes more objective.

The computing procedure involved can be outlined as follows:

The data input consists of $\underline{g}_1$, $\underline{g}_2$, $\theta_1$ and $\theta_2$ where

$\underline{g}_1$, $\underline{g}_2$ = two independent reciprocal lattice vectors obtained from the relevant diffraction pattern,

$\theta_1$, $\theta_2$ = the angles made by the trace normal to the habit plane with $\underline{g}_1$ and $\underline{g}_2$ respectively.

If all the vectors involved are normalised to give unit vectors, the operative zone axis ($\underline{Z}$) is given by

$$\underline{Z} = \hat{\underline{g}}_1 \times \hat{\underline{g}}_2 \quad \text{(The circumflex implies a unit vector)}$$

so that the trace normal vector ($\underline{t}$) can be calculated by the simultaneous solution of the following equations:

$$\hat{\underline{g}}_1 \cdot \hat{\underline{t}} = \cos(\theta_1)$$

$$\hat{\underline{g}}_2 \cdot \hat{\underline{t}} = \cos(\theta_2)$$

$$\hat{\underline{Z}} \cdot \hat{\underline{t}} = (\widehat{\hat{\underline{g}}_1 \times \hat{\underline{g}}_2}) \cdot \hat{\underline{t}} = 0$$

Hence the great circle representing the locus of the possible habit plane poles is given by

$$\hat{\underline{P}} = \hat{\underline{Z}} \times \hat{\underline{t}}$$

We then proceed to systematically guess the real pole of the habit plane, $\{hkl\}$ and calculate the angular deviation $\delta$ of the pole $\{hkl\}$ from the great circle whose pole is given by $\underline{P}$. This is repeated for all 24 variants of $\{hkl\}$, and that which gives a minimum departure $\delta_{min}$ from the great circle $\underline{P}$ is taken to be the best possibility for the particular guessed form. In this manner, a set $D_{hkl}$ which represents the $\delta_{min}$ values for all the experimental data corresponding to the guessed pole $\{hkl\}$ is obtained.

In this way, the procedure is repeated systematically for as many guesses of $\{hkl\}$ as required, so that a new set consisting of values of (the sub-sets) $D_{hkl}$ is generated. That value of $D_{hkl}$ which is the minimum element of the new set then gives the 'best fit' habit plane $\{HKL\}$ consistent with the experimental data.

When a large amount of experimental data is available, the set $D_{HKL}$ can be subjected to statistical analysis, to indicate whether its elements (the various values of $\delta_{min}$ corresponding to each set of experimental data) simply result from random measurement errors.

A precaution built into the program is that it does not

allow the habit plane to lie in the foil plane, since in such a case a habit plane trace would not be obtained.

The actual program is not included in this thesis because at the time of writing, it in fact consists of three separate programs (due to capacity limitations of the mini-computer used) which carry out different stages of the calculations. Thus large amounts of data have to be transferred between programs. In addition, the programs are written in BASIC, and no attempts have been made to optimise the computing time involved.

(iii) Experimental Habit Plane Determinations

(a) Fe-24Ni-0.16C

It is known that retained austenite can be found in this alloy despite its high calculated $M_s$ temperature of 77°C, (134). Optical microscopy revealed the traces of only four different habit planes and it was confirmed that the optically observed habit corresponded to that found by transmission electron microscopy - dark field imaging (using an austenite reflection) revealed only four independent traces of the austenite-martensite interfaces when large areas were examined at low magnification.

Hence the method of Crocker et al. (139) was applied and inter-trace angles formed by the intersection of three habit plane variants (as observed by optical microscopy) with the plane of section were measured. These were then plotted on a ternary angle diagram (figure VI.13) whose sides represent the inter-trace angles. The angles almost completely fell within the domain specified for a $\{111\}_\gamma$ plane, confirming that the habit plane was near to $\{111\}_\gamma$, in agreement with (134). It is therefore thought that the results of Chilton et al. (135) who found a $\{123\}_\alpha$ habit may be ambiguously interpreted; they used single surface trace analysis coupled with electron diffraction to determine their habit planes, and the dangers of the simple form of such an analysis have been outlined earlier.

(b) Fe-25.2Ni-1.9Mn

This alloy has a calculated $M_s$ temperature of 70°C, which compares well with the Fe-24Ni-0.16C alloy with an $M_s$ of 77°C. Both these alloys gave lath martensite (figure VI.14) on water quenching from the austenitising temperature (1200°C for 5 min). Two surface analysis using optical microscopy provided values of inter-packet plane angles. These were found to best fit the set of angles formed between variants of $\{28\ 13\ 10\}_\gamma$, as given in

table VI.3. In one particular prior austenite grain, nine independent packet plane traces could be observed, and by measuring the angles between a reference trace and the other traces, it was possible to show that they were consistent with the above packet plane using the method given in (VI.4.ii.b). These results are presented in figure VI.15.

Single surface trace analysis using electron diffraction pattern/bright field image pairs and the computing technique of (VI.4.ii.d) gave the martensite lath habit plane with a best fit near $\{33\ 18\ 10\}_{\alpha'}$. The results are presented in figure VI.16. It is notable that after transforming all 24 independent variants of $\{28\ 13\ 10\}_{\gamma}$ through the KS orientation variant (1), we find that $\{10\ \bar{1}3\ 28\}_{\gamma}$ transforms to $\{18\ \bar{1}0\ 36\}_{\alpha'}$, indicating that once again the packet and lath planes are equivalent, and that the habit plane may more specifically be $\{10\ \bar{1}3\ 28\}_{\gamma}$ // $\{18\ \bar{1}0\ 33\}_{\alpha'}$.

X-ray analysis indicated that the Fe-25Ni-2Mn alloy contained 21% retained austenite at room temperature while the Fe-24Ni-0.16C alloy contained 16%; both the alloys had been water quenched following austenitisation at 1310°C for 20 min, when $P_{111}$ was found to be zero in both cases. Allowing for an experimental error of 2%, the difference in the retained austenite contents is not large and is consistent with the small difference in $M_s$ temperatures between the two alloys.

The above results suggest that not only is the cross-over point of the free energy surfaces of martensite and austenite similar for both the alloys (as manifested in their similar $M_s$ temperatures), but their behaviour below $M_s$ must also be similar since the amounts of austenite retained at room temperature are approximately the same. The latter point implies that the gradients of the free energy surfaces concerned (with respect to temperature) may be similar for both alloys.

We note that the likeness in behaviour noted above is not reflected in the crystallographic characteristics, since the habit planes of the two alloys have been demonstrated to be very different. It therefore appears that crystallography in itself does not control the extent of transformation, but is simply the route towards the achievement of the required degree of transformation.

The crystallographic characteristics of martensite are related to the operative shear systems for any given alloy so that the

specific crystallography may be expected to vary with the relative strengths of the austenite and martensite involved. This idea was originally proposed by Davies and Magee (141). In the present investigation, the strength of the martensite in the Fe-24Ni-0.16C alloy must be higher than that of the Fe-25Ni-2Mn alloy since the former contains carbon in interstitial solid solution. Since the flow stress of austenite is insensitive to the Ni, Mn and C contents (85,141), a difference in crystallographic behaviour can be expected between the above two alloys.

(c) Fe-0.4C-4Ni

Optical microscopy revealed that the martensite in this alloy had a habit plane multiplicity greater than four. Single surface trace analysis using electron diffraction (VI.4.ii.d) showed that the habit plane was near $\{123\}_{\alpha'}$, figure VI.17. Since a large set of data (60 electron diffraction pattern/bright field image pairs were analysed) had been obtained, the errors (i.e. the set of $\delta_{min}$ values obtained using the best fit computing technique) could be statistically analysed and were shown to follow the Normal cumulative distribution (fig.VI.18), implying that most of the departure of the great circles (fig.VI.17) from the $\{123\}_{\alpha'}$ pole may be due to random errors.

The detailed crystallography of this alloy has not yet been resolved.

## (VI.5) General Summary

It seems that the thin films of retained austenite found between laths of low alloy martensite are mechanically stabilised, by the jamming of the austenite-martensite interface by transformation induced accommodation defects.

The stability and distribution of the films of austenite is a function of the local martensite-martensite crystallography. Inter-lath films of austenite are generally found to be absent when the adjacent variants of martensite form in a mutually accommodating manner, i.e. twin-related.

It has been shown that twin-related variants of martensite which are also variants of the austenite-martensite orientation relationship can only arise when the latter corresponds to the Kurdjumov-Sachs orientation relationship.

Initial results suggest that the behaviour of the transformation below the $M_s$ temperature is not a sensitive function of the habit plane of the martensite, and it is thought that the crystallographic differences probably reflect variations in the relative strengths of the austenite and martensite concerned.

## TABLE VI.1

**The 24 Independent variants of the Kurdjumov and Sachs Orientation Relationship**

| Variant No. | Description | | Group No. |
|---|---|---|---|
| 1 | $(011)_\alpha$ // $(111)_\gamma$ | $[\bar{1}\bar{1}1]_\alpha$ // $[\bar{1}01]_\gamma$ | 1 |
| 2 | (011) // (111) | $[\bar{1}\bar{1}1]$ // $[0\bar{1}1]$ | 1 |
| 3 | (011) // (111) | $[\bar{1}\bar{1}1]$ // $[1\bar{1}0]$ | 1 |
| 4 | (011) // (111) | $[1\bar{1}1]$ // $[\bar{1}01]$ | 1 |
| 5 | (011) // (111) | $[1\bar{1}1]$ // $[0\bar{1}1]$ | 1 |
| 6 | (011) // (111) | $[1\bar{1}1]$ // $[1\bar{1}0]$ | 1 |
| 7 | (011) // $(\bar{1}\bar{1}1)$ | $[\bar{1}\bar{1}1]$ // $[1\bar{1}0]$ | 2 |
| 8 | (011) // $(\bar{1}\bar{1}1)$ | $[\bar{1}\bar{1}1]$ // $[101]$ | 2 |
| 9 | (011) // $(\bar{1}\bar{1}1)$ | $[\bar{1}\bar{1}1]$ // $[011]$ | 2 |
| 10 | (011) // $(\bar{1}\bar{1}1)$ | $[1\bar{1}1]$ // $[1\bar{1}0]$ | 2 |
| 11 | (011) // $(\bar{1}\bar{1}1)$ | $[1\bar{1}1]$ // $[101]$ | 2 |
| 12 | (011) // $(\bar{1}\bar{1}1)$ | $[1\bar{1}1]$ // $[011]$ | 2 |
| 13 | (011) // $(\bar{1}1\bar{1})$ | $[\bar{1}\bar{1}1]$ // $[110]$ | 3 |
| 14 | (011) // $(\bar{1}1\bar{1})$ | $[\bar{1}\bar{1}1]$ // $[011]$ | 3 |
| 15 | (011) // $(\bar{1}1\bar{1})$ | $[\bar{1}\bar{1}1]$ // $[\bar{1}01]$ | 3 |
| 16 | (011) // $(\bar{1}1\bar{1})$ | $[1\bar{1}1]$ // $[110]$ | 3 |
| 17 | (011) // $(\bar{1}1\bar{1})$ | $[1\bar{1}1]$ // $[011]$ | 3 |
| 18 | (011) // $(\bar{1}1\bar{1})$ | $[1\bar{1}1]$ // $[\bar{1}01]$ | 3 |
| 19 | (011) // $(1\bar{1}\bar{1})$ | $[\bar{1}\bar{1}1]$ // $[110]$ | 4 |
| 20 | (011) // $(1\bar{1}\bar{1})$ | $[\bar{1}\bar{1}1]$ // $[101]$ | 4 |
| 21 | (011) // $(1\bar{1}\bar{1})$ | $[\bar{1}\bar{1}1]$ // $[0\bar{1}1]$ | 4 |
| 22 | (011) // $(1\bar{1}\bar{1})$ | $[1\bar{1}1]$ // $[110]$ | 4 |
| 23 | (011) // $(1\bar{1}\bar{1})$ | $[1\bar{1}1]$ // $[101]$ | 4 |
| 24 | (011) // $(1\bar{1}\bar{1})$ | $[1\bar{1}1]$ // $[0\bar{1}1]$ | 4 |

TABLE VI.2

The Axis-Angle pairs relating Martensite lattices which are variants of the Kurdjumov and Sachs Orientation Relationship

| Variant No. | Rotation Axis | | | Rotation Angle/Degrees |
|---|---|---|---|---|
| 2 | .0000 | .7071 | .7071 | 60 |
| 3 | .0000 | .7071 | .7071 | 120 |
| 4 | .0000 | .7071 | .7071 | -70.52 |
| 5 | .0000 | .7071 | .7071 | -10.5 |
| 6 | .0000 | .7071 | .7071 | 49.5 |
| 7 | .3568 | -.1784 | .9170 | 146.4 |
| 8 | -.0750 | -.1667 | .9832 | 180 |
| 9 | -.2901 | -.1485 | .9454 | 31.2 |
| 10 | .8305 | -.1384 | .5396 | 116.7 |
| 11 | .4331 | -.1767 | .8839 | 141.2 |
| 12 | .0000 | -.1710 | .9853 | 173.9 |
| 13 | -.8492 | .4246 | .3139 | 146.5 |
| 14 | -.8563 | -.0432 | .5147 | 120 |
| 15 | -.5774 | -.5774 | .5774 | 109.48 |
| 16 | -.8304 | -.1384 | .5396 | 116.8 |
| 17 | -.4990 | -.6569 | .5653 | 109.8 |
| 18 | .0000 | -.9200 | .3919 | 124.3 |
| 19 | -.7698 | .1492 | -.6206 | 120 |
| 20 | -.4184 | .6423 | -.6422 | 109.47 |
| 21 | .0862 | .9030 | -.4209 | 118.87 |
| 22 | -.8414 | -.3842 | -.3821 | 152.04 |
| 23 | -.8091 | .0567 | -.5849 | 121.8 |
| 24 | -.4987 | .5757 | -.6480 | 121.48 |

Notes

1) Right-handed rotations are taken to be positive.
2) The rotations are relative to variant one (table VI.1) and refer to the martensite lattice.

Table VI.3

Two Surface analysis results on Fe-25.2Ni-1.9Mn alloy

| $(hkl)_\gamma$ | Computed angle between $(hkl)_\gamma$ and $(28\ 13\ 10)_\gamma$ | Measured angle between $(hkl)_\gamma$ and $(28\ 13\ 10)_\gamma$ |
|---|---|---|
| $\bar{2}8\ 13\ 10$ | 119.3 | 117 |
| $\bar{2}8\ 10\ 13$ | 119.8 | - |
| $\bar{1}0\ 28\ 13$ | 78.3 | 78 |
| $10\ 13\ \bar{2}8$ | 80.8 | 81 |
| $\bar{1}0\ 13\ 28$ | 80.8 | - |
| $10\ \bar{1}3\ 28$ | 68.2 | 70 |
| $13\ 28\ 10$ | 38.2 | 38 |
| $13\ 28\ \bar{1}0$ | 53.4 | 51 |
| $13\ \bar{2}8\ 10$ | 84.6 | 85 |
| $\bar{1}3\ 28\ 10$ | 84.6 | - |

Notes

The experimentally measured angles quoted above are those found between the martensite habit plane variants by two surface analysis using optical microscopy. The computed angles are with reference to $(28\ 13\ 10)_\gamma$ . The angles are quoted in degrees and the experimental error is probably $\pm 2°$, mainly due to the difficulty in precisely determining the habit plane trace.

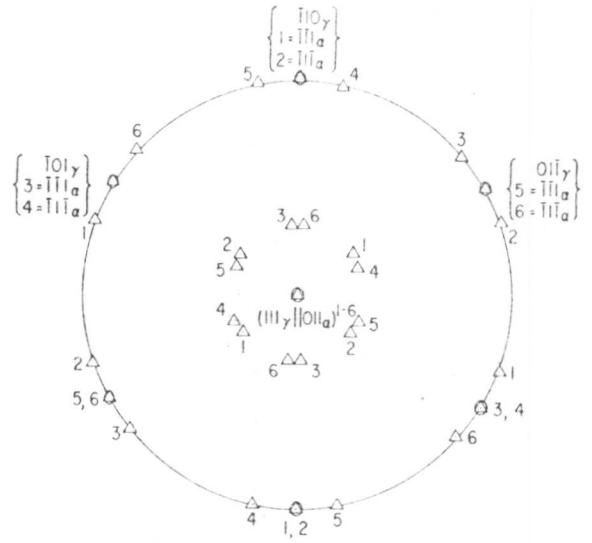

| $\alpha_1$ $\alpha_2$ | ORIENTATION RELATIONSHIP | |
|---|---|---|
| 1-2, 3-4, 5-6 | TWIN RELATED | (70° 32' ROTATION ABOUT $[0\bar{1}1]_\alpha$ OR 180° ROTATION ABOUT $[111]_\alpha$) |
| 1-4, 2-5, 3-6 | SMALL ANGLE | (10° ROTATION ABOUT $[0\bar{1}1]_\alpha$) |
| 1-3, 1-5, 2-4, 2-6, 3-5, 4-6 | LARGE ANGLE | (60° ROTATION ABOUT $[0\bar{1}1]_\alpha$) |
| 1-6, 2-3, 4-5 | LARGE ANGLE | (49° ROTATION ABOUT $[0\bar{1}1]_\alpha$) |

*Kurdjumov–Sachs variants from common* $(111)_\gamma$

Figure VI.1

The Speich & Swann analysis (ref.115) of the Kurdjumov-Sachs orientation relationship.

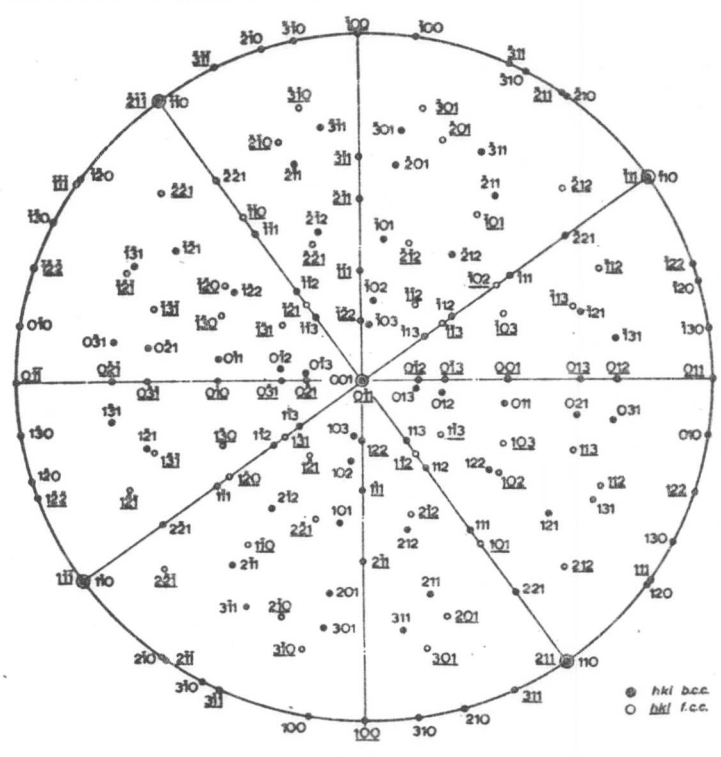

**Stereographic projection representing the N–W orientation relationship between body- and face-centred cubic materials.**
**(001) b.c.c. //(011) f.c.c.**
**(1$\bar{1}$0) b.c.c. //(1$\bar{1}$1) f.c.c.**
**(110) b.c.c. //(2$\bar{1}$1) f.c.c.**

Figure VI.2

Stereogram representing the Nishiyama-Wasserman orientation relationship.

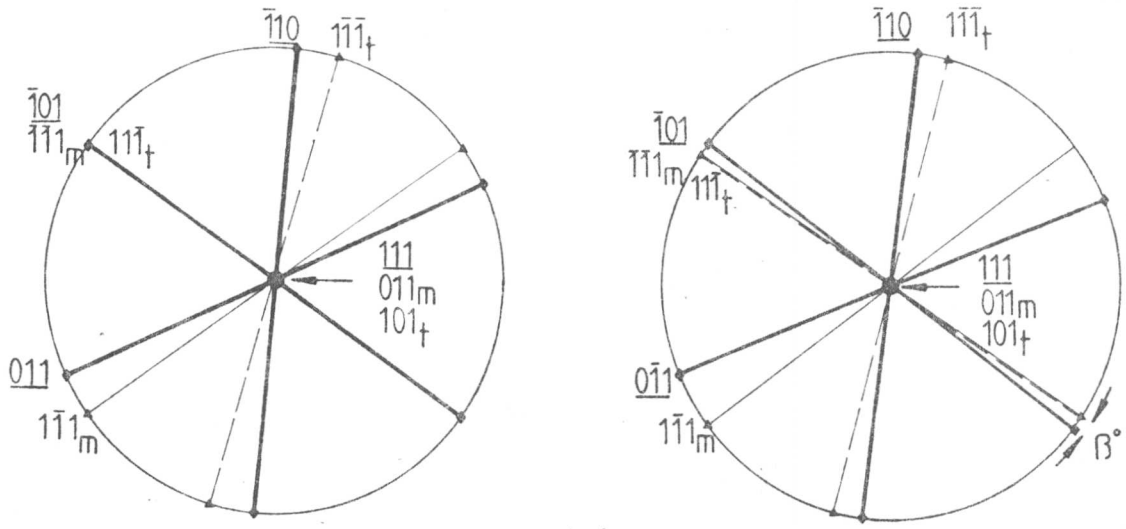


Figure VI.3

Stereograms illustrating how the slightest departure ($\beta$) from parallelism of the close packed directions of austenite and martensite leads to the nonexistence of twin-related martensite variants (assuming that the parallelism of the closest packed planes is maintained).

(a) Two twin-related martensite variants simultaneously in Kurdjumov-Sachs orientation with the austenite.

(b) The martensite variants in this case are still twin-related, but have crystallographically non-equivalent orientation relationships with the austenite.

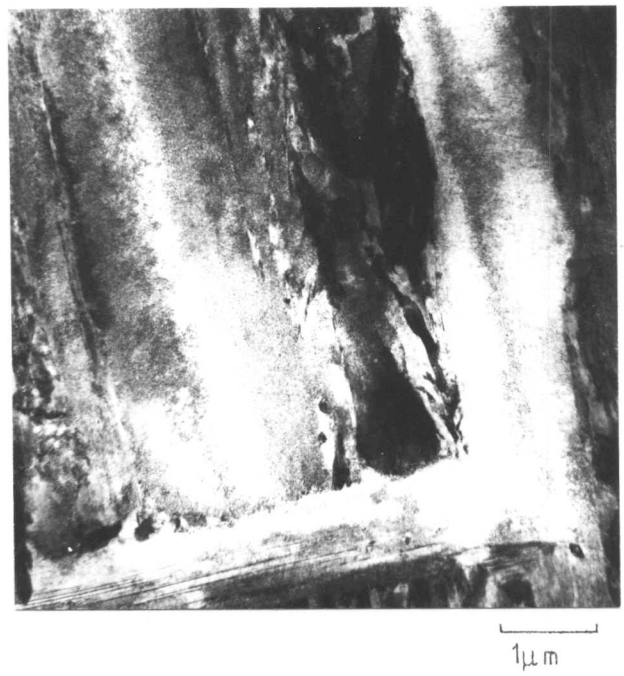


Figure VI.4

Transmission electron micrograph showing the partitioning behaviour of the martensite in Fe-4Ni-0.4C steel.

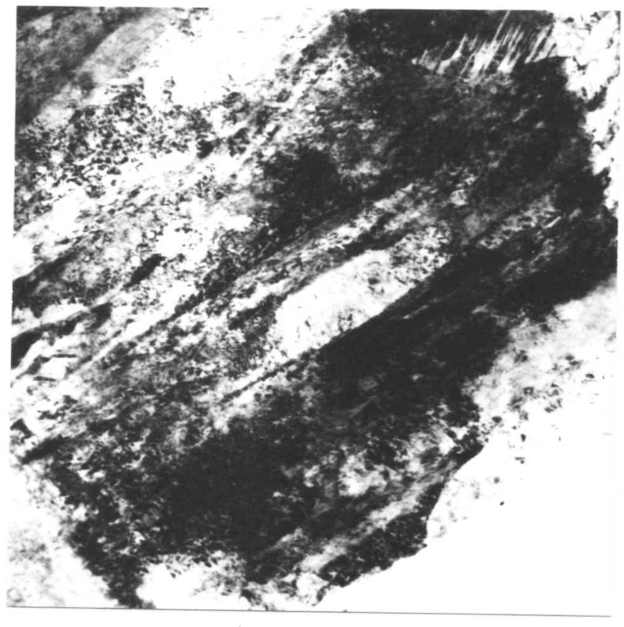


(a)

(b)

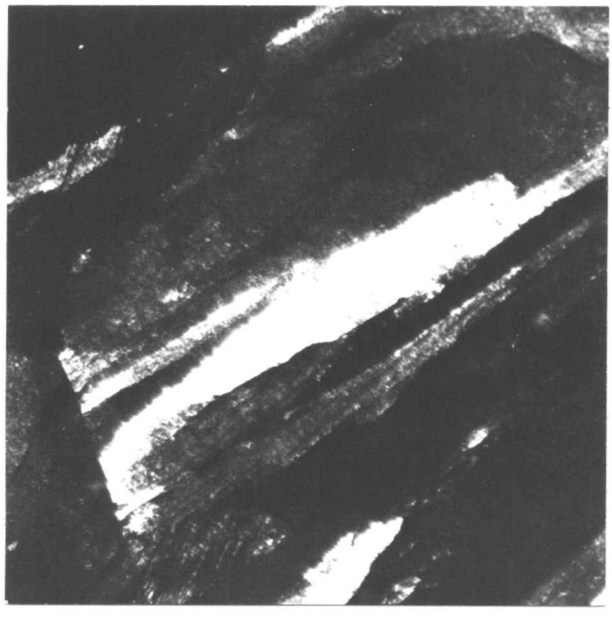

(c)

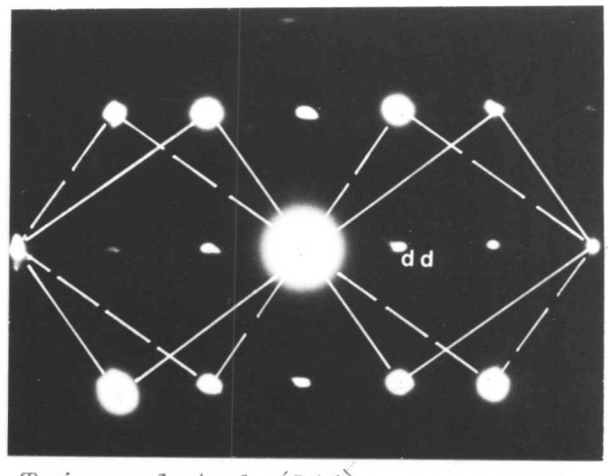


Twin related $\langle 011 \rangle_\alpha$ zones with a relative rotation of 70.52°. (dd = double diffraction)

(d)

Figure VI.5

Fe-4Ni-0.4C alloy, austenitised at 1200°C for 5 minutes and water quenched.

(a) Bright field image.

(b) & (c) Dark field images of twin related martensite variants.

(d) Corresponding diffraction pattern.

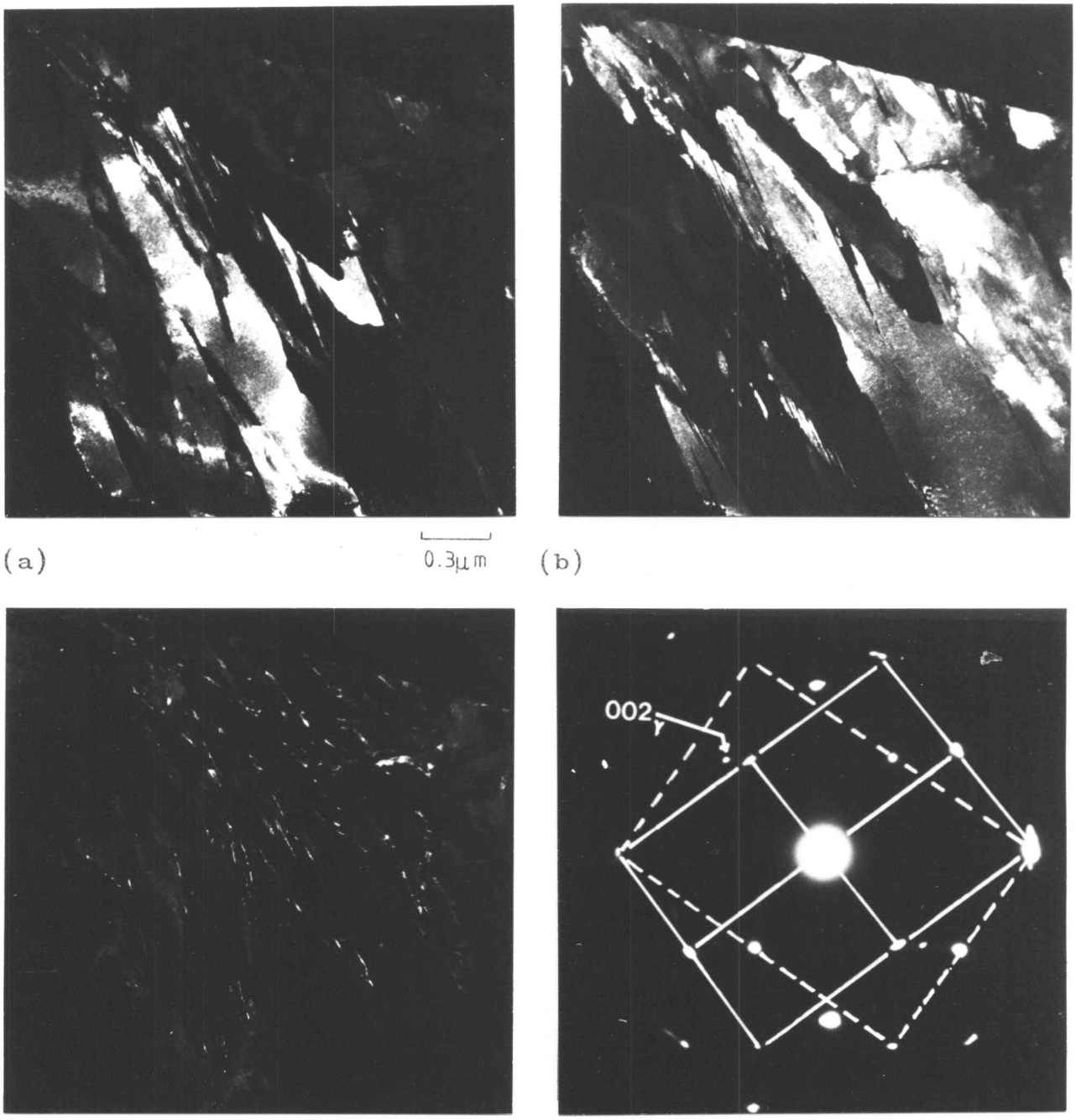


(a) (b)

(c) (d)

Figure VI.6

Fe-4Ni-0.4C alloy, austenitised at 1200°C for 5 minutes and water quenched.

(a) & (b) Dark field images of twin related martensite variants.

(c) Dark field image of retained austenite.

(d) Corresponding diffraction pattern, showing an $\{002\}_\gamma$ reflection in addition to twin-related $\langle 011 \rangle_{\alpha'}$ zones.

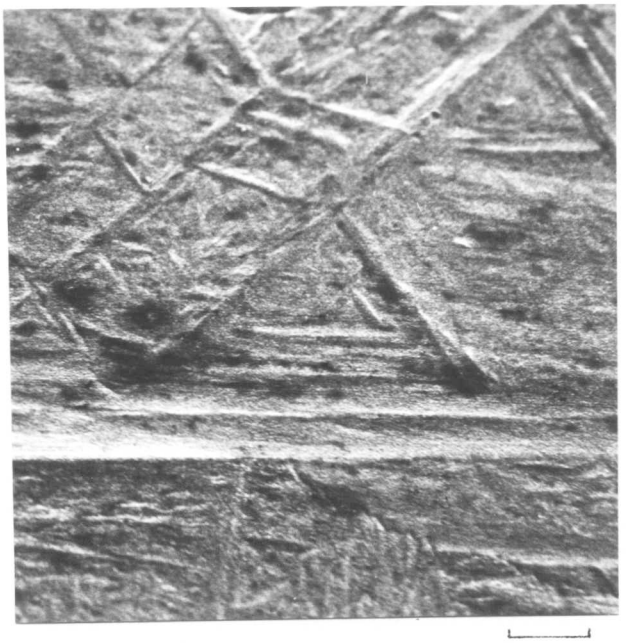


Figure VI.7
Scanning electron microscope image of surface relief due to martensite formation in Fe-4Ni-0.4C alloy.

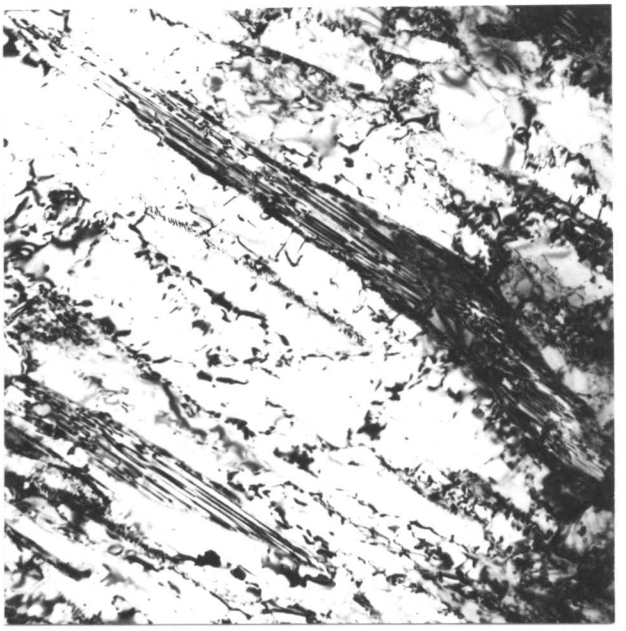


Figure VI.8a
Bright field image of martensite and retained austenite in a high alloy steel (described in the text).

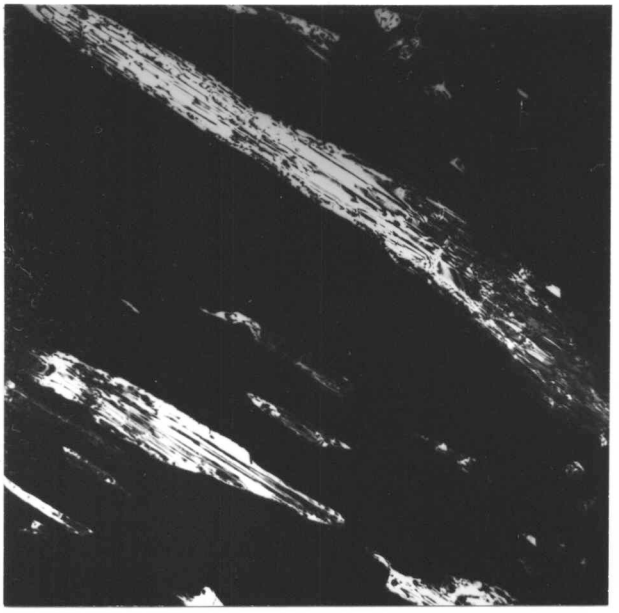

Figure VI.8b
Corresponging dark field image of retained austenite.

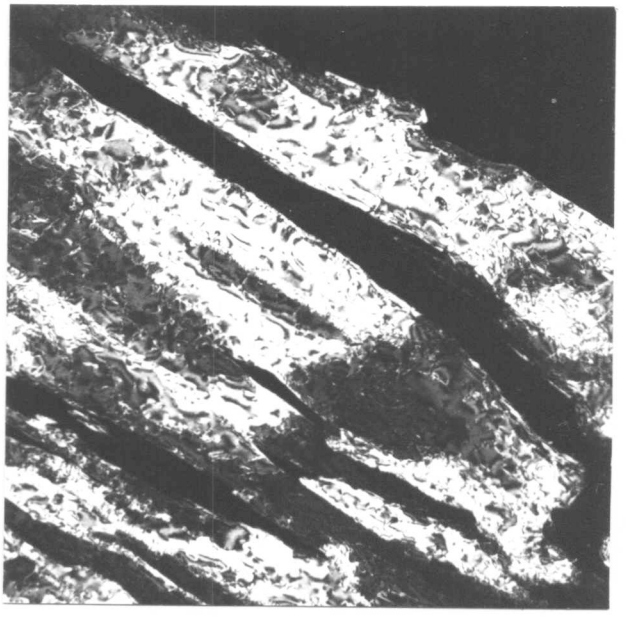

Figure VI.8c
Corresponding dark field image of martensite.

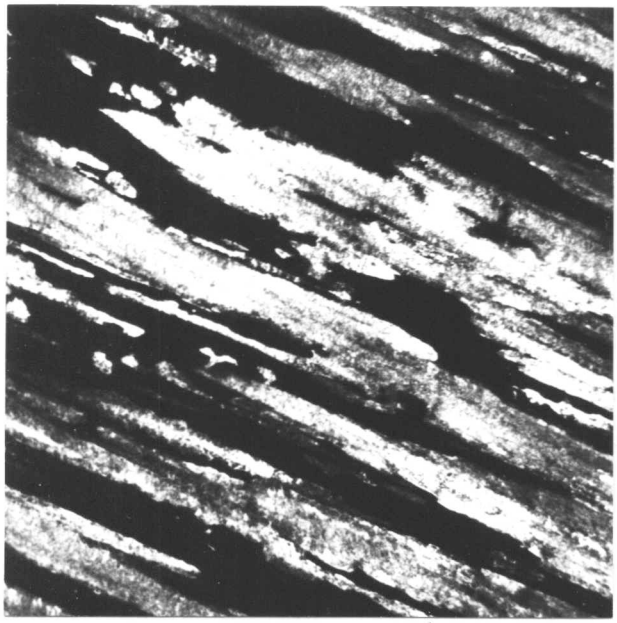

(a)

0.5μm

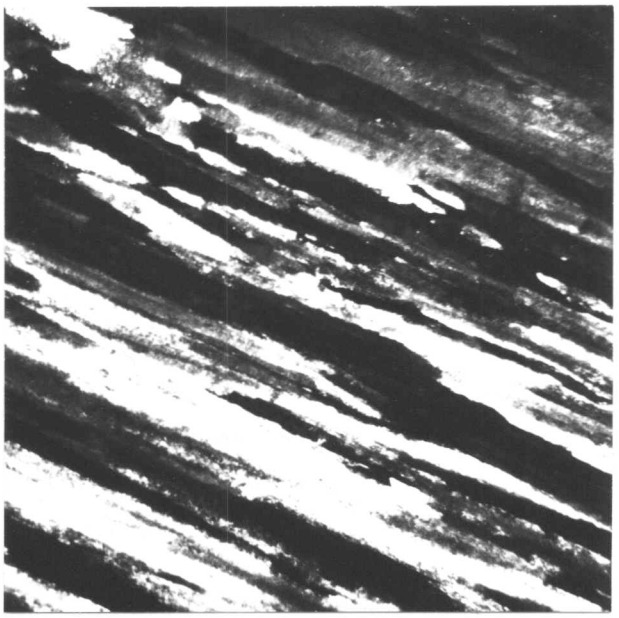

(b)

(c)

Figure VI.9

Fe-0.31C-2.0Si alloy, austenitised at 1100°C for 5 minutes, quenched to 334°C and held at this temperature for 1 hour before finally quenching to room temperature.

(a) & (b) Dark field images of twin-related martensite variants.

(c) Corresponding diffraction pattern showing twin-related $\langle 011 \rangle_{\alpha'}$ zones.

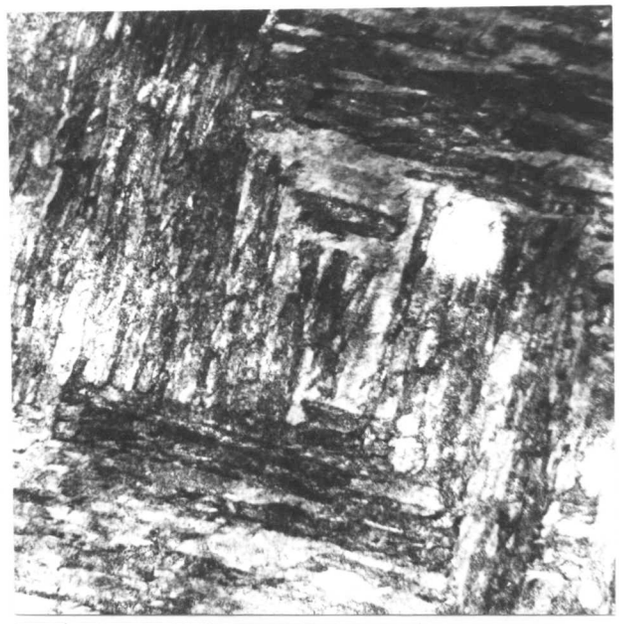

Figure VI.10
Electron micrograph illustrating the nature of twin-related martensite packets in Fe-0.31C-2.0Si alloy, heat treated as given in fig.VI.9.

1μm

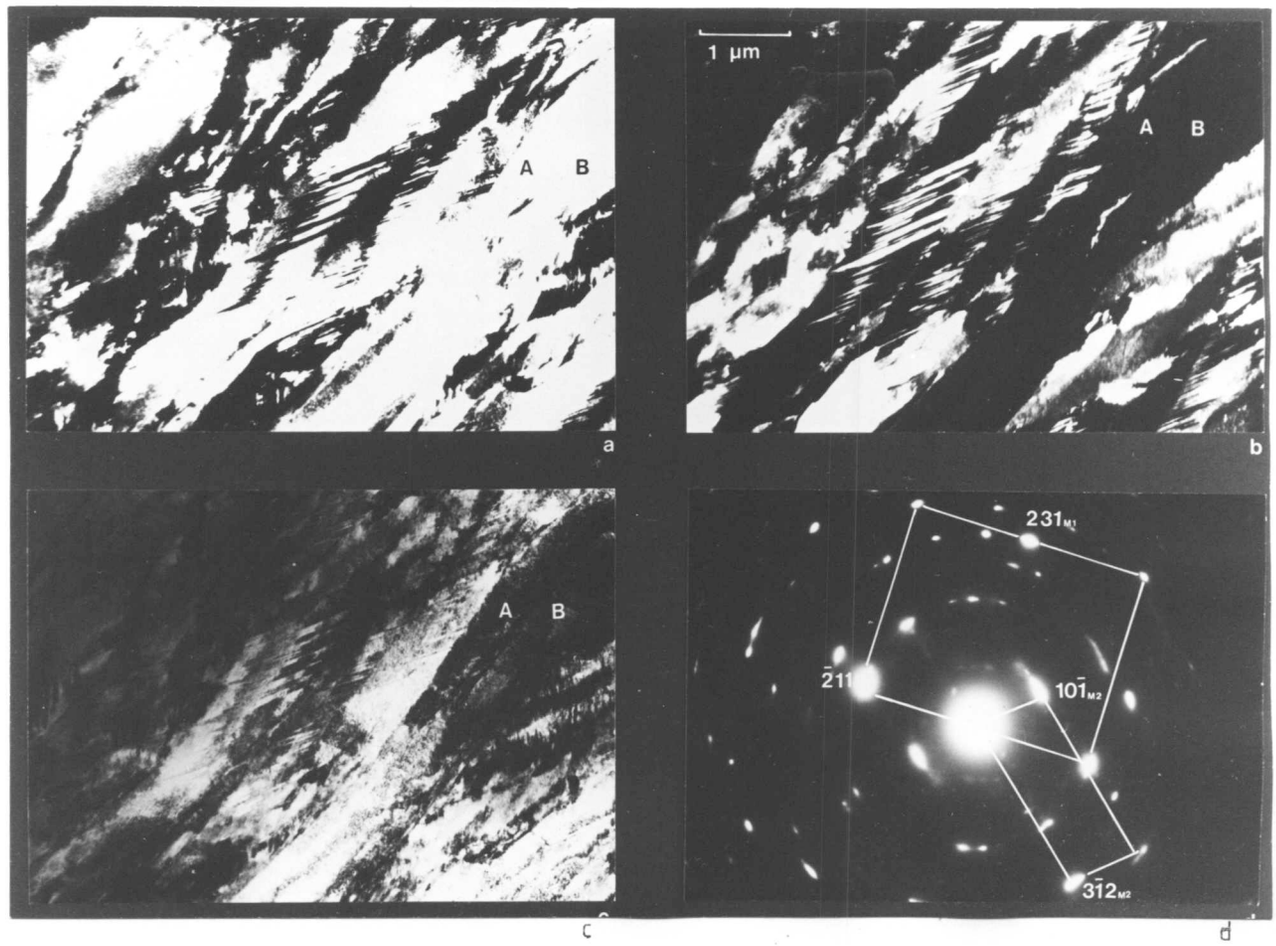


Figure VI.11.
Fe-4Ni-0.4C alloy, austenitised at 1200°C for 5 minutes and water quenched.

(a) & (b) Dark field images of twin-related martensite variants, and of internal twins within the martensite units.

(c) Bright field image. The laths marked 'A' and 'B' are in the same orientation and do not show any twinning.

(d) Corresponding diffraction pattern which can be shown to be consistent with twin-related lattices.

Figure VI.12

Diagram illustrating the solid geometry applicable to the method of inter-trace angle measurement (single surface) for habit plane determination. LMN represents the plane of section and the inter-trace angles are defined by the equations given below. One of the set of distances (a,b,c) can be taken to be unity.

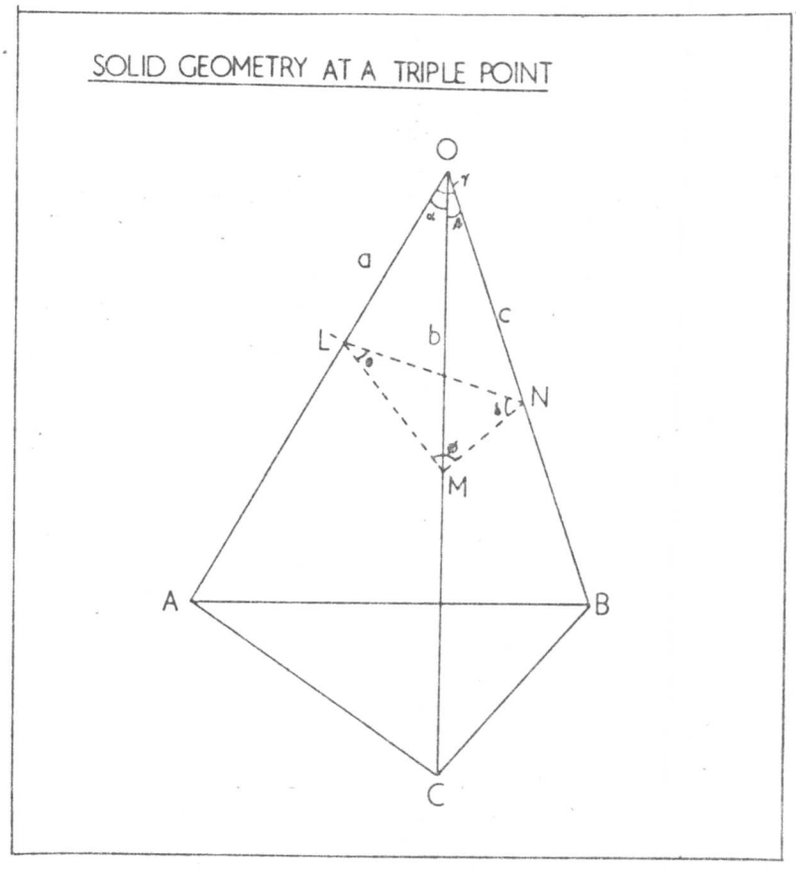


$$\cos\theta = \frac{a^2 - a\cos\alpha - ac\cos\gamma + c\cos\beta}{\left[(1 + a^2 - 2a\cos\alpha)(a^2 + c^2 - 2ac\cos\gamma)\right]^{1/2}}$$

$$\cos\phi = \frac{1 - a\cos\alpha - \cos\beta + ac\cos\gamma}{\left[(1 + a^2 - 2a\cos\alpha)(1 + c^2 - 2c\cos\beta)\right]^{1/2}}$$

$$\cos\delta = \frac{c^2 - c\cos\beta - ac\cos\gamma + a\cos\alpha}{\left[(1 + c^2 - 2c\cos\beta)(a^2 + c^2 - 2ac\cos\gamma)\right]^{1/2}}$$

For the above equations, (b) has been chosen to equal unity.

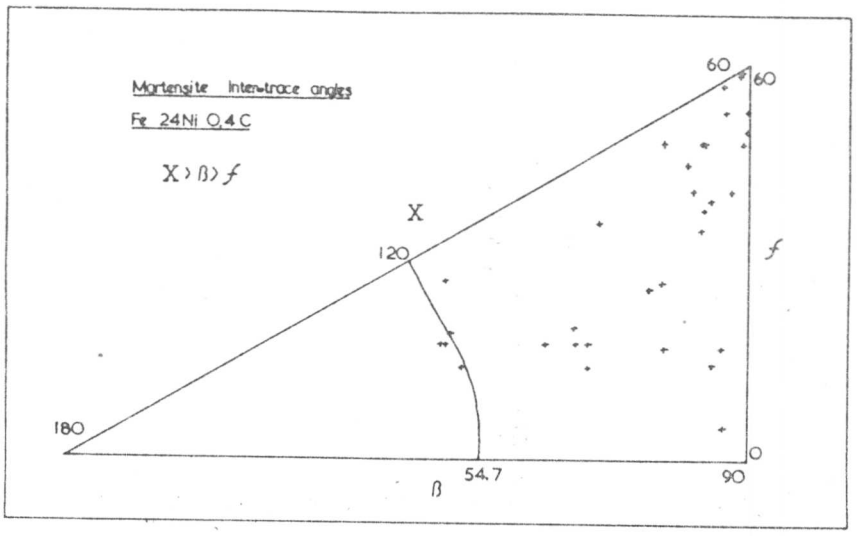


Figure VI.13
Ternary inter-trace angle diagram showing the experimental fit of the martensite habit plane in quenched Fe-24Ni-0.16C alloy with a $\{111\}_\gamma$ plane.

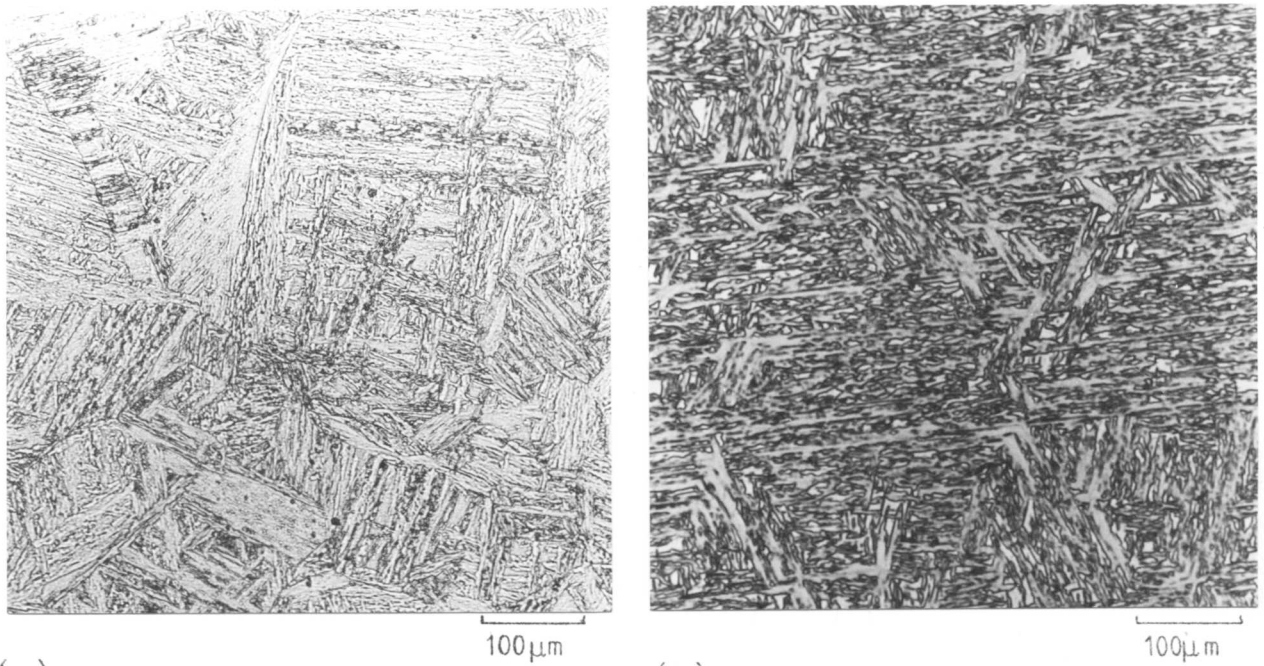


(a) (b)

Figure VI.14
Optical micrographs of lath martensite in (a) Fe-25.2Ni-1.9Mn
(b) Fe-24Ni-0.16C


(a)

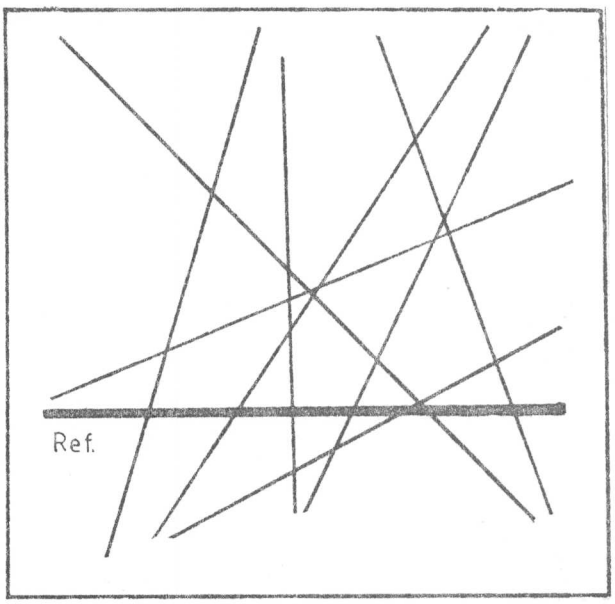


(b)

Figure VI.15

Experimental evidence to show that the inter-martensite trace angles within a prior austenite grain in Fe-25.2Ni-1.9Mn alloy are consistent with a $\{28\ 13\ 10\}_\gamma$ habit plane.

(a) Optical micrograph showing the prior austenite grain under examination.

(b) Diagram showing the relative dispositions of habit plane traces.

The following table lists the results obtained; the angles are quoted relative to the reference trace, which is arbitrarily taken to originate from a $(10\ 13\ 28)_\gamma$ plane.

| Trace | Habit Plane Variant | Measured Angle | Computed Angle |
|---|---|---|---|
| 1 | $10\ 13\ 28$ | - | - |
| 2 | $\bar{1}0\ 13\ 28$ | 47 | 47 |
| 3 | $\bar{2}8\ 13\ 10$ | 89 | 83 |
| 4 | $28\ \bar{1}3\ 10$ | 64 | 66 |
| 5 | $13\ \bar{1}0\ 28$ | 23 | 23 |
| 6 | $\bar{1}0\ \bar{2}8\ \bar{1}3$ | 29 | 33 |
| 7 | $\bar{2}8\ 10\ 13$ | 71 | 76 |
| 8 | $\bar{2}8\ \bar{1}0\ 13$ | 56 | 51 |
| 9 | $\bar{1}3\ \bar{2}8\ \bar{1}0$ | 73 | 77 |

The approximate computed plane of section is $(21\ 39\ 28)_\gamma$

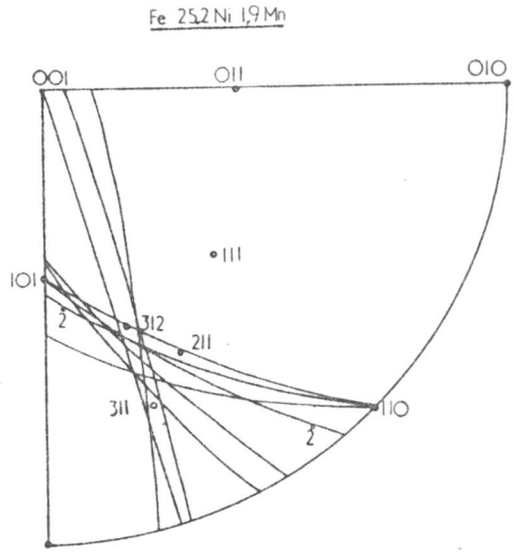


Figure VI.16
Trace analysis on the martensite in the Fe-25Ni-2Mn alloy.

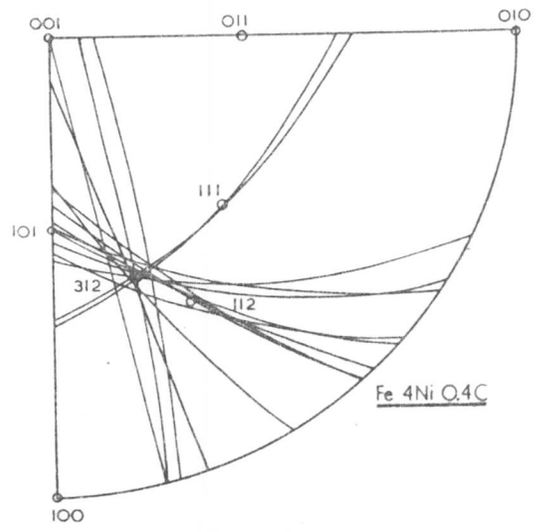


Figure VI.17
Trace analysis on the martensite in the Fe-4Ni-0.4C alloy.

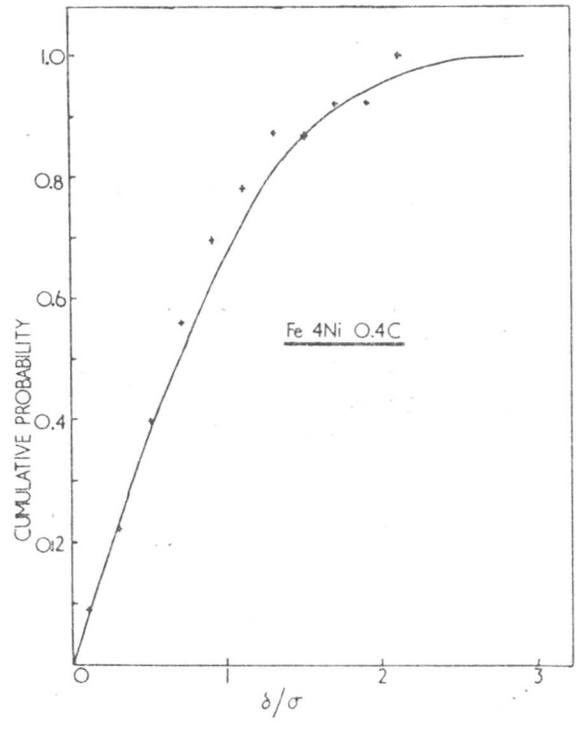


Figure VI.18
A plot of the experimental data (plotted as points) and computed cumulative probability (continuous line) of occurrance of error as a function of the normalised error $\delta/\sigma$ (where $\sigma$ is the standard deviation of $\delta$ ). The plot indicates that the observed errors could essentially be interpreted as measurement errors, of the 'Normal' type.

# CHAPTER SEVEN

## A DIRECT ANALYSIS OF TWINNING IN A LOW ALLOY MARTENSITE

### (VII.1) Introduction

The deformation processes involved in the formation of low alloy martensites appear from microstructural observations to be essentially slip. However, extremely high dislocation densities are generally observed, such that the arrangement of the dislocations is very confused and does not give useful information on the slip systems involved. The fact that the dominant deformation process in low alloy martensite is slip is not surprising since the $M_s$ temperatures concerned are relatively high when compared with fully twinned plate martensites. Despite the high $M_s$, however, incipient twinning can often be observed in low alloy martensites (142-5,Ch.VI). These twins sometimes extend only partially across the martensite units and the inter-twin spacings are generally larger and more variable than those intuitively expected from observations on well-defined plate martensites. It is not apparent whether these twins represent a mode of lattice invariant shear (and hence whether they can be useful in the application of the phenomenological theory of martensite formation) or whether they are simply manifestations of accommodation effects.

It is considered important to resolve the mechanism of formation of such twins, not only because this may lead to a better understanding of low alloy martensites (and their associated retained austenite), but also because they appear to influence the toughness of ultra-high strength steels (142-5). It has been suggested that the twins reduce toughness by reducing the available number of slip systems (142) although this idea is not firmly based since the yield strength does not appear to vary with the propensity of twinning in a given alloy (145). The situation is rather confusing, since the $M_s$ temperature does not correlate with the presence or absence of twinning in mainly dislocated martensites (144). Furthermore, the intensity of twinning seems to vary with the austenitising conditions (145) although this evidence must be treated with caution since such determinations are based on rather qualitative observations from a limited amount of electron microscopy.

It seems important to resolve the mechanism of twin formation first, before attempting to study any interactions of twins with other properties. It was the purpose of the present work

to determine whether the twins can be described as intrinsic transformation features (similar to those found in plate martensites) or whether they result from high velocity impingements between martensite variants.

Unfortunately, it seems that the only method capable of distinguishing between the two cases entails detailed crystallographic analysis with respect to both the parent and the product phases. The lack of adequate quantities of the parent austenite phase, and the scale of the martensite microstructure in low alloy steels has excluded such an analysis in the past. In the present work, a novel method is used to enable the retention of experimentally expedient quantities of austenite, thus enabling a direct analysis of the twins in a low alloy martensite.

## (VII.2) Experimental Method and Techniques

An experimental Fe-0.43C-3.00Mn-2.02Si steel of known transformation characteristics (Ch.1) was used in the present study. The $M_s$ temperature of this alloy is 220°C and isothermal transformation at 350°C results in the formation of upper bainite (Ch.1). The upper bainite in this steel is exceptional in the sense that the high silicon content prevents the formation of carbides. Thus, the carbon which is partitioned into the residual austenite following the formation of bainitic ferrite stabilises the austenite and causes its retention following quenching to room temperature. This characteristic was exploited as described below.

A specimen was austenitised in a dynamic protective argon atmosphere at 1100°C for 20 mins and was then directly quenched into oil at 140°C. After holding at 140°C for 40 s, it was immediately up-quenched into a tin bath held at 350°C for isothermal transformation of some of the remaining austenite to upper bainite. After holding at 350°C for 25 mins, the specimen was finally water quenched. The direct quench to 140°C resulted in partial transformation to martensite, to an estimated extent of 50% by volume. This is because 140°C is below the $M_s$ but well above the '$M_f$' temperature of this alloy. The specimen was first transformed to martensite so that the carbon content of the martensite was the same as that of the alloy. The subsequent up-quench resulted in the transformation of some of the remaining austenite to upper bainite, with the accompanying carbon enrichment of the austenite between the martensite units,

and between the bainite sub-units. Thus, when the specimen was finally quenched to room temperature, the inter-martensite residual austenite was fully retained. Under normal circumstances this would have transformed to martensite.

Specimens for examination by transmission electron microscopy were prepared in the manner described in (I.2). A Philips EM300 transmission electron microscope operated at 100kV was used for this work.

(VII.3) Results and Discussion

The orientation relationship between the martensite and austenite was found by simple electron diffraction to be that of Kurdjumov and Sachs (110), (KS), i.e.

$$(111)_\gamma \;//\; (011)_{\alpha'}$$
$$[\bar{1}01]_\gamma \;//\; [\bar{1}\bar{1}1]_{\alpha'}$$

The above variant will be used as the standard variant in the analysis that follows. While it is noted that simple electron diffraction of this kind cannot give accurate orientation relationships, it will become clear later that the orientation has to be KS. This conclusion comes from the observation of twin-related martensite variants, a situation which has been shown to arise (VI.2) only with the KS orientation relationship.

Owing to the high silicon content of the alloy used, the formation of martensite is not accompanied by autotempering (I.3.i). However, due to the up-quench component of the heat treatment used for the present study, the martensite was found to be tempered, as shown in figures VII.1a,2a.

Single surface trace analysis was carried out to establish the twin plane and its relation to the austenite lattice. The analysis was always in terms of the standard correspondence stated above. The great circle representing the locus of the twin plane pole was plotted consistently and unambiguously with respect to the austenite, martensite and martensite twin lattices. The results are presented in figures VII.1,2.

For martensite twins to be transformation twins, certain symmetry requirements have to be satisfied (61). Assuming that the twins are of type 1 (involving a rotation of 180° about the pole of the twin plane), the twins have to relate adjacent martensite regions whose c-axes are variants of the c-axes of the Bain distortion. This means that the twin plane has to be

a plane of mirror symmetry with respect to the austenite lattice after transforming through the appropriate correspondence matrix. Furthermore, for the twinning system to be considered as an intrinsic transformation inhomogeneity, the twin plane must, in all cases, correspond to the same austenite mirror plane when the analysis is in terms of a standard correspondence. Thus specific Miller indices can be assigned to the twin plane (for the standard variant) and these indices have to be the same (not just of the same form) for every case examined if the twins are to be considered as transformation twins. Substitution into the phenomenological theory easily demonstrates that lattice invariant shears on different planes of the same form give different (crystallographically non-equivalent) solutions.

In figures VII.1,2 the evidence from the diffraction patterns is plotted on stereograms which also have the poles of the austenite and martensite matrix plotted in the standard KS variant. The great circles (A) and (B) represent the observed austenite and martensite matrix zones respectively, (D) represents the possible locus of the twin plane normal and (C) refers to the zone of coincidence. The zone of coincidence is defined as the zone obtained by superimposing the martensite matrix and twin stereograms in the correct relative orientation such that on this zone, twin and matrix poles of the same form are coincident. Furthermore, this zone must also contain all the coincident $\{110\}_{\alpha'}$ and $\{112\}_{\alpha'}$ poles. Assuming that the twin plane will either be $\{110\}_{\alpha'}$ or $\{112\}_{\alpha'}$ and that the twin boundary corresponds to the twinning plane, the intersection of (C) and (D) defines the twin plane. The former assumption takes account of the fact that the $\{110\}_{\alpha'}$ and $\{112\}_{\alpha'}$ planes are the most likely twin planes in BCC lattices (146) while the latter assumption is based on the fact that the energy of a twin boundary is a minimum when the composition plane coincides with the twin plane (147).

In figure VII.1 the twin plane is seen to be $(\bar{1}12)_{\alpha'} \equiv (011)_{\gamma}$ while that in figure VII.2 is $(112)_{\alpha'} \equiv (101)_{\gamma}$. This is despite the fact that they have both been plotted in the standard variant of the orientation relationship. In figure VII.1 the twin is not a variant of KS whereas in figure VII.2 it is. We can therefore conclude that since the twin plane does not uniquely correspond to a particular austenite mirror plane, the twins cannot be an intrinsic transformation feature and must be

attributed to accommodation effects.

Some rather spectacular physical evidence for this can be seen from the micrographs of figures VII.1,2. In fig.VII.1 the martensite matrices of the adjacent martensite plates are not twin related. The incidence of twinning is observed to be low and the twins are fine. On the other hand, in fig.VII.2, the adjacent martensite variants are twin related and dark field imaging shows extensive twinning; often large areas of the laths are twinned. In the latter case, since the two martensite variants are twin related, the nucleation of mechanical twins would be easier, and furthermore, the transmission of deformation across twin related lattices would be easier compared relative orientations. Hence accommodation of transformation strains would be easier for twin related martensite variants.

## (VII.4) Summary

It has been found that the twinning observed in the martensite of an Fe-Mn-Si-C low-alloy steel is an accommodation phenomenon since the twin planes show inconsistent correspondence relative to austenite when analysed in terms of the standard variant of the orientation relationship.

The extent of twinning can be understood on the basis of the above conclusion and upon considering the inter-martensite orientations. It is possible that the intensity of twinning would be reduced if the martensite can be designed to adopt an orientation relationship other than KS.

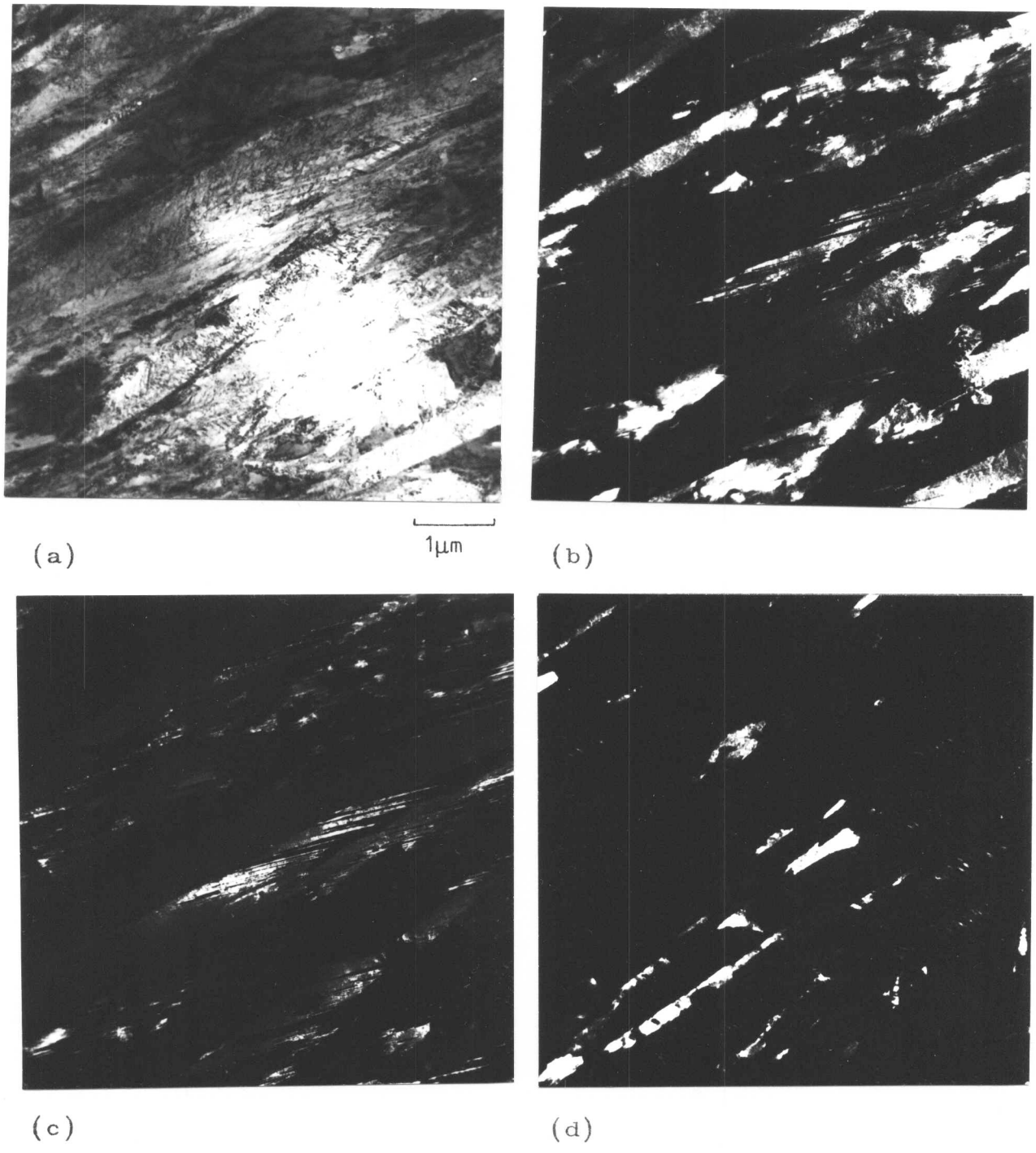


Figure VII.1

(a) Bright field image.

(b) Matrix martensite dark field image.

(c) Martensite twin dark field image.

(d) Retained austenite dark field image.

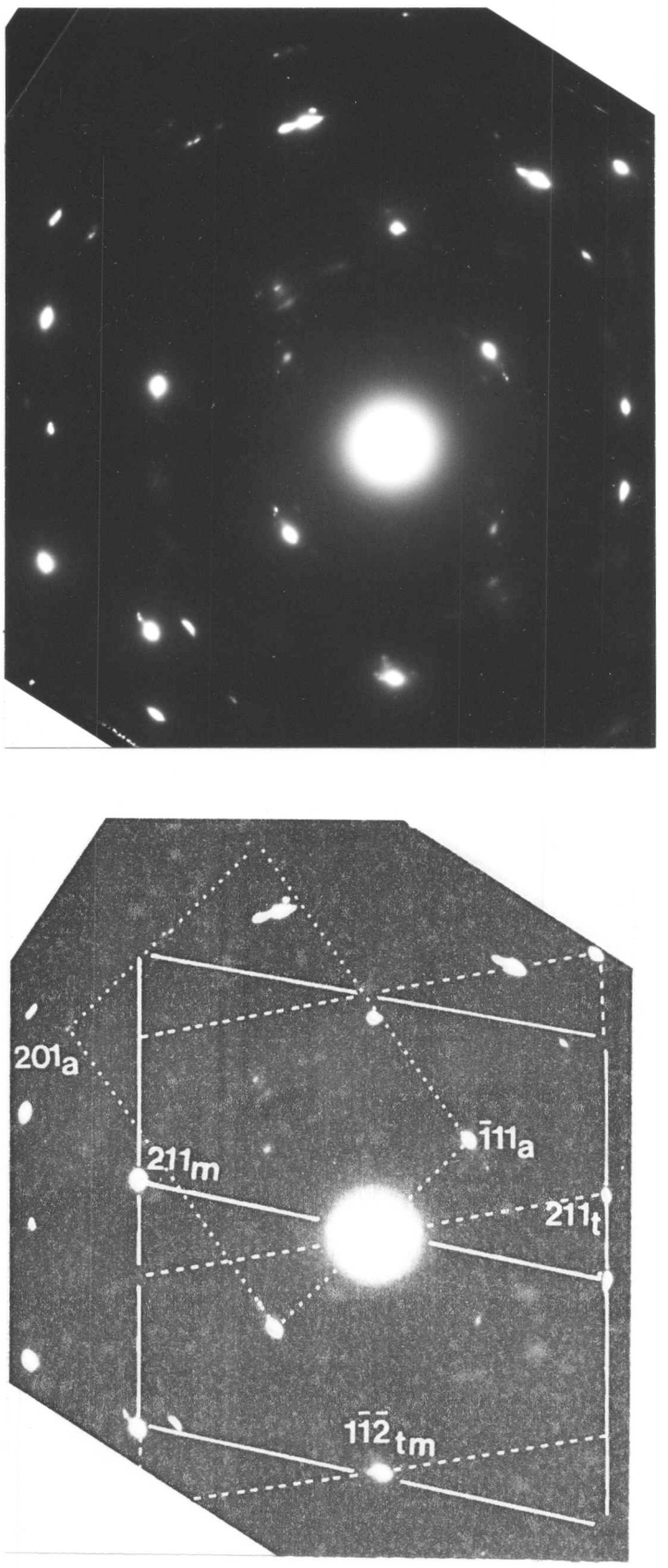


Figure VII.1e.i

Diffraction pattern showing twin-related $\langle 135 \rangle_\alpha$ zones and $[123]_\gamma$ zone.

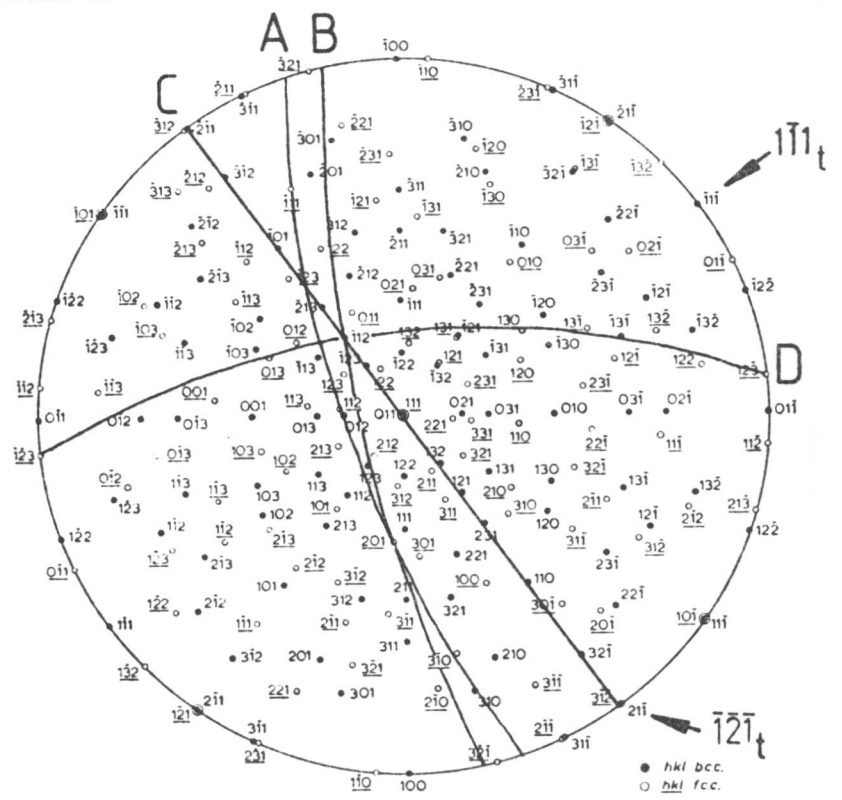


Figure VII.1e.ii

Corresponding stereographic analysis.

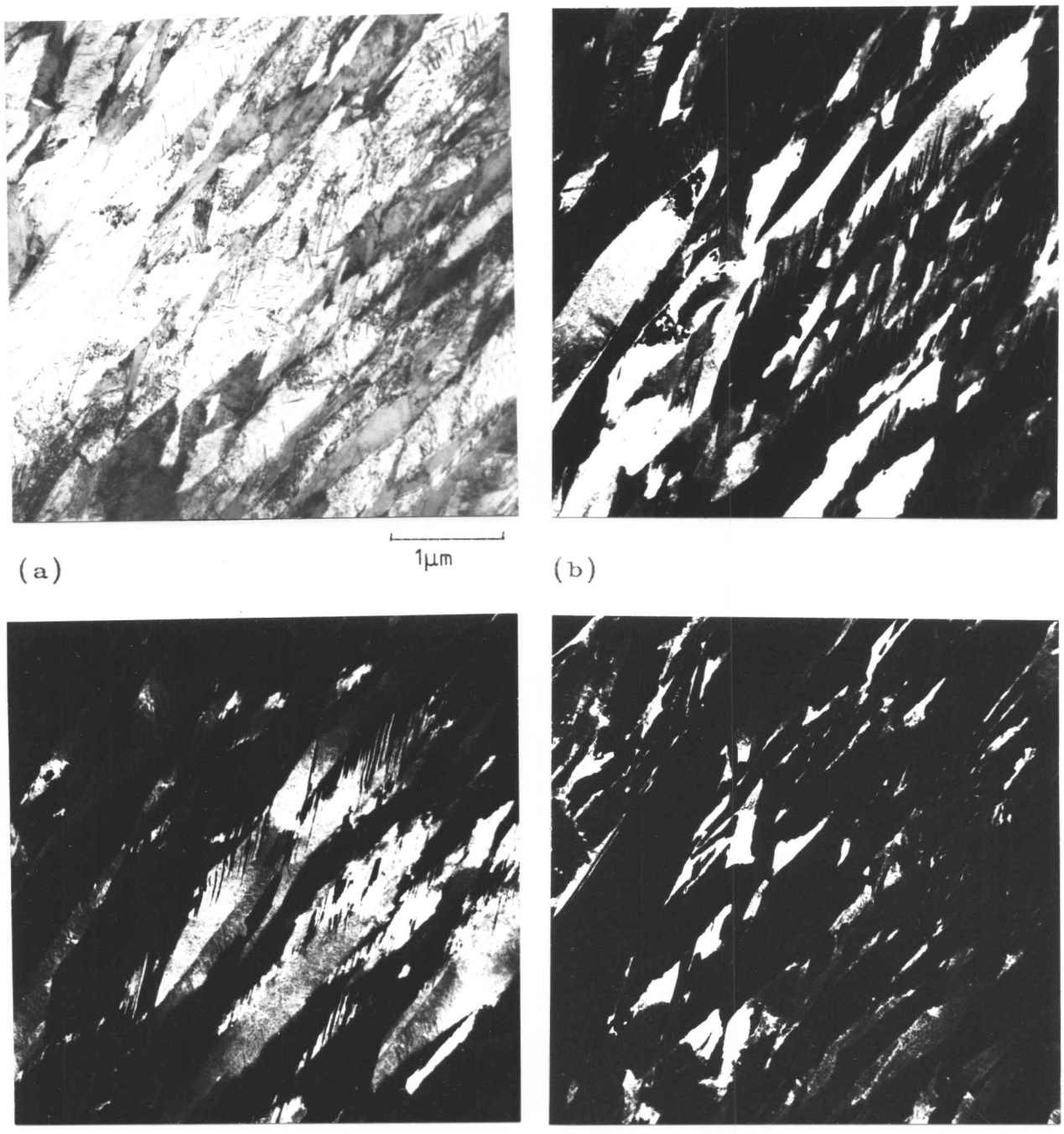


Figure VII.2

(a) Bright field image.

(b) Matrix martensite dark field image.

(c) Martensite twin dark field image.

(d) Retained austenite dark field image.

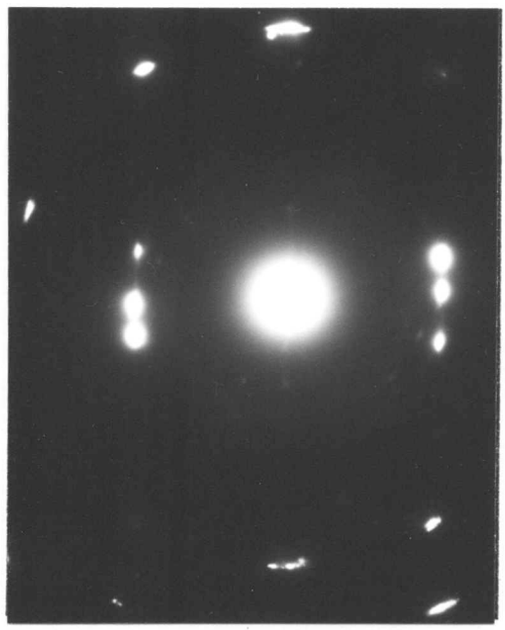

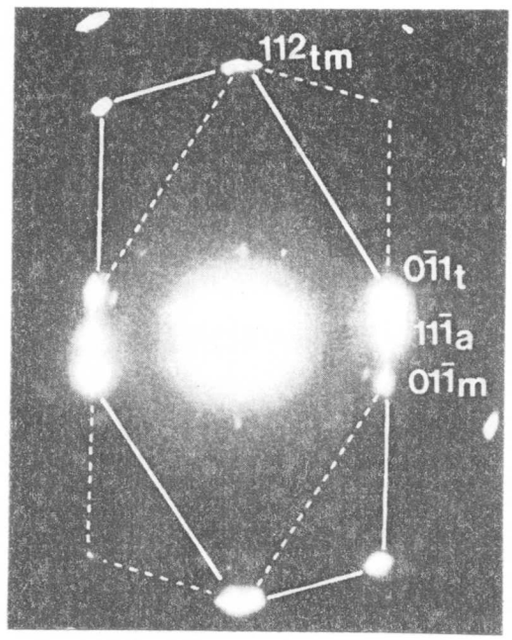


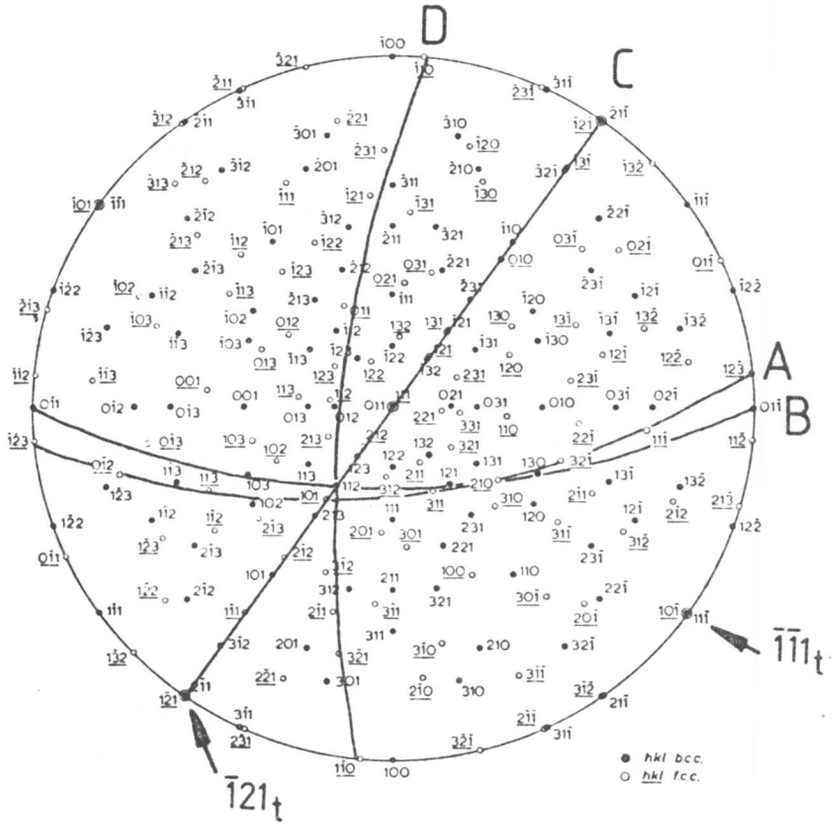


Figure VII.2e

Diffraction pattern showing twin-related $\langle 113 \rangle_{\alpha'}$ zones and corresponding stereographic analysis.

# CHAPTER EIGHT

## AN ANALYSIS OF THE MECHANICAL PROPERTIES AND MICROSTRUCTURE OF A HIGH-SILICON DUAL-PHASE STEEL

### (VIII.1) Introduction

The simple method of mixtures analysis used to describe the strength variations of the silicon upper bainite was shown to be rather inadequate in (III.3.ii). The point was made that a more sophisticated model would be necessary in order to understand the interactions between the various components of the microstructure.

The aim of the present work was to evaluate two available deformation models. Such evaluation was considered necessary because there are some apparent discrepancies (which will become evident later) associated with the application of such models.

An additional difficulty is that such models require very detailed input data, of the type not yet available for the upper bainitic microstructure. Furthermore, for the purpose of model evaluation, it seemed expedient to use a simpler microstructure; since the dual-phase steel microstructure (to be described below) appears to be eligible in this respect and is at the same time of considerable industrial importance, it was chosen to be the test microstructure.

The term dual-phase steels has been used to describe the product of recent process/structure modifications to conventional HSLA steels. They can most conveniently be defined as low-carbon low-alloy ferritic steels with an aggregate microstructure of ferrite and a non-pearlitic hard phase (e.g. martensite). Their potential as superior strength and formability substitutes for current automotive steels in the USA was early realised (148-9) and has provided an incentive for their rapid development and acceptance in this role. This successful application has preceded the acquisition of a complete understanding of the detailed relationships between their process route, microstructure and mechanical properties, although considerable research has been carried out in order to optimise the variables in the strength and formability balance.

Steel composition has been one of the aspects studied, and it appears that the use of high silicon additions ( 2 wt. pct.) results in better combinations of strength and formability (150-3).

In solid solution, silicon not only increases strength, but its presence also raises the tensile stress to yield stress ratio, while at the same time eliminating discontinuous yielding (150). This last point is important in the avoidance of stretcher strain markings during forming operations. Relative to its capability to increase strength, silicon has a minimal detrimental effect on ductility (151). Silicon is also known to retard martensite tempering reactions (23-25) and often eliminates autotempering altogether (Ch.1). This effect should increase the strength of the martensitic component of dual-phase structures since carbon will then remain in interstitial solid solution in the martensite lattice.

The hardenability of dual-phase steels is generally critically balanced in order to achieve the necessary microstructure using continuous production processes, while at the same time being compatible with the weldability, strength and ductility requirements. However, little attention has been paid to the detailed microstructure of the hard phase, which is in turn a function of the hardenability of the residual austenite. In the case of high-silicon heat treatable steels, it has been shown that the best strength and toughness combination is achieved with a homogeneous upper bainitic microstructure (Ch.III). It should be noted that upper bainite in high-silicon steels consists of alternating layers of high-carbon retained austenite and 'interstitial free' dislocated bainitic ferrite (Ch.I). Furthermore, the properties of high-silicon steels are extremely structure sensitive (Ch.III). In the present study the mechanical properties and microstructure of an experimental high-silicon dual-phase steel are examined in detail.

The most important property characteristic of dual-phase steels, at least so far as their application in cold-pressing operations is concerned, is their high strain hardening coefficient. A high strain hardening coefficient, or n-value, stabilises tensile deformation against local instability and results in a greater degree of uniform elongation. In order to test the experimental behaviour of dual-phase steels, and eventually to achieve a predictive capability for structure-property relationships, a working model of the deformation of a composite consisting of two ductile components is required. Before the experimental results of the present work are considered, an evaluation is made of two available deformation models.

(VIII.2) Deformation Models

A model successfully used (154-5) to obtain the deformation parameters of dual-phase steels is that due to Mileiko (156). The use of Mileiko's theory has been stimulated by its capability to predict directly the strain hardening coefficient (the latter being equivalent to the true uniform elongation of a ductile phase) of the composite concerned. The relationship between the volume fraction, V, of the second phase and the mechanical properties of the composite and of the component phases is given by

$$V = \frac{1}{1 + \beta \frac{\varepsilon_c - \varepsilon_m}{\varepsilon_f - \varepsilon_c} \varepsilon_c^{\varepsilon_m} \varepsilon_f} \qquad \text{Equation VIII.1}$$

where $\beta = (\sigma_m \varepsilon_f^{\varepsilon_f} \exp \varepsilon_m) / (\sigma_f \varepsilon_m^{\varepsilon_m} \exp \varepsilon_f)$ Equation VIII.1a

and $\sigma_m$ and $\sigma_f$ are the true tensile strengths of the martensite (or any other hard phase) and ferrite respectively, and $\varepsilon_c$ , $\varepsilon_m$ and $\varepsilon_f$ are the true uniform strains for the composite, martensite and ferrite respectively. The relationship is valid when the true stress/true strain behaviour of the composite and of the component phases can be represented by a power law of the form:

$$\sigma = K \varepsilon^n \qquad \text{Equation VIII.2}$$

where K is the strengthening coefficient.

However, the critical assumptions of this model require, firstly, equal strain distributions in both the hard and soft phases, and secondly, continuity of the phases in the tensile direction. Hence, the conclusions drawn by the application of Mileiko's theory to dual-phase steels have been criticised recently (157), especially as it has been shown (157) that different deductions, particularly with respect to strength/formability ratios, can be made by assuming non-uniform strain in the component phases.

Despite the above setbacks, it is apparent that Mileiko's theory does indeed give reasonable agreement with experimental data on the dual-phase steels examined thus far (154-5). The reasons for this agreement are not clear and it was felt that a more detailed analysis was necessary. The availability of a more general two-phase deformation theory developed by Tomota et al.(henceforth referred to as Tomota's theory, ref. 158)

where the internal stresses produced by inhomogeneous deformation are taken into account allows the detailed examination of the deformation behaviour involved. Furthermore, the latter theory applies to the case where the harder (or softer) phase is randomly distributed as grains of ellipsoidal shape (the random distribution ensures an effect approximating spherical grains) and is therefore more representative of dual-phase steel microstructures. Additionally, the stress and strain distributions can be followed at every stage of the deformation process. By this theory, the applied stress before the onset of plastic deformation in the hard phase is given as

$$\sigma_{33}^{A} = \sigma_f' \left| \frac{\bar{\varepsilon}_p}{1-f} \right| + \frac{f}{(1-f)} \bar{\varepsilon}_p \qquad \text{Equation VIII.3}$$

where $\bar{\varepsilon}_p = (1-f)\varepsilon_p'$ Equation VIII.3a

(Nomenclature listed in table VIII.1)

and the onset of plastic flow in the harder phase is represented by the following set of simultaneous equations:

$$Y(II) = \sigma_f' \left| \frac{\bar{\varepsilon}_{p(II)}}{1-f} \right| + \frac{f}{(1-f)} A\bar{\varepsilon}_{p(II)} \qquad \text{Equation VIII.4}$$

$$Y(II) = \sigma_y'' - A\bar{\varepsilon}_{p(II)} \qquad \text{Equation VIII.5}$$

Further deformation is calculated for small strain increments from the following simultaneous equations:

$$\sigma_f' \left| \varepsilon_{p(II)}' + \delta\varepsilon_p' \right| = \sigma_{33}^{A} - fA[\varepsilon_{p(II)}' + (\delta\varepsilon_p' - \delta\varepsilon_p'')] \qquad \text{Equation VIII.6}$$

$$\sigma_f'' |\delta\varepsilon_p''| = \sigma_{33}^{A} + (1-f)A[\varepsilon_{p(II)}' (\delta\varepsilon_p' - \delta\varepsilon_p'')] \qquad \text{Equation VIII.7}$$

Elastic deformation results in the term $(\sigma_{33}^{A}/E)$ being added to the plastic strain of the alloy.

Thus the complete stress-strain curve can be computed and it follows that so can the strain hardening coefficient when the latter curve (or its segments) can be represented by the empirical equation, $\sigma = K\varepsilon^{n}$. In the analysis that follows, equations of the above form were used to represent the flow stresses of the individual components and of the composite. The strain increment $\delta\varepsilon_p'$ was taken as 0.01 and it was assumed that the modulus is the same for all phases. The yield stresses were taken as the true stress at $\varepsilon_t = 0.002$.

Mileiko's theory has been successfully applied to analyse the deformation of a zero-carbon ferrite/martensite structure in

Fe-3Ni-3Mo (154), and a ferrite/martensite structure in a vanadium HSLA steel, Fe-0.15C-1.5Mn-0.11V, (155). Considering first the data presented in reference (154) for the Fe-3Ni-3Mo alloy, the following deformation parameters can be listed:

$\sigma_y''$ = 705 MPa  $K_m$ = 1113 MPa

$n_m$ = 0.06  $K_f$ = 369 MPa

$n_f$ = 0.24

The results of the inhomogeneous deformation analysis by Tomota's method are plotted in fig.VIII.1 and it is clear that the predictions are essentially the same as those of Mileiko's model. The reason for this becomes apparent from fig.VIII.2, which shows the plastic strain in the ferrite as a function of that in the martensite, calculated using Tomota's theory. It is clear that the plastic strain difference between the two components is very small, so that the equal strain model is applicable. This agreement with Mileiko's theory arises due to the relatively small amount of plastic strain in the ferrite prior to the onset of plastic flow in the martensite.

Similarly, application of the inhomogeneous deformation model to the data of ref.155 for the vanadium HSLA steel showed that the plastic strain difference between the ferrite and martensite components was also sufficiently small to give similar results to those predicted by Mileiko's theory, figs.VIII.3,4. In this analysis the following deformation parameters were used:

$\sigma_y''$ = 1500 MPa  $K_m$ = 2448 MPa

$n_m$ = 0.08  $K_f$ = 690 MPa

$n_f$ = 0.31

The values of the strengthening coefficients were calculated from the tensile strength values quoted in (155), assuming failure by the ductile mode so that $\sigma_{uts} = K n^n$ .

## (VIII.3) Experimental Procedure

A 2kg melt of the experimental alloy was prepared from pure constitutents in a vacuum induction furnace, and the final analysis was Fe-0.04C-0.63Mn-2.01Si-0.1V. The ingot was hot worked down to 8 mm diameter rod by forging and swaging operations.

During austenitising treatments, the specimens were doubly protected by a dynamic argon atmosphere and a proprietary anti-decarburising compound. The heat treatments were carried out in

a resistance heated tube furnace.

Tensile specimens were machined [from heat treated blanks] with a 50 mm parallel length and a 3 mm diameter. They were tested on an Instron testing machine instrumented with a 25 mm gauge length linearly variable differential transformer extensometer. This was attached to the specimen for only a part of the test and the final uniform elongation was measured from 5 mm gauge lengths previously marked on the specimen parallel length, taking care that the measurement was well away from the position of the necked region.

Specimens for transmission electron microscopy were cut from the tensile specimen blanks as 3 mm diameter discs with a thickness of 0.25 mm. The discs were subsequently thinned and electropolished in a twin-jet polishing unit using a 25% glycerol, 5% perchloric acid and 70% ethanol mixture at room temperature and 55V. The foils were examined in a Philips EM300 microscope operating at 100 kV.

Quantitative metallography was carried out on a Quantimet image analysing computer.

(VIII.4) Results and Discussion

(i) Microstructural Observations

The volume fractions of hard phases obtained by various heat treatments are listed in table VIII.2. Using these data, and the fact that the formation of poreutectoid ferrite involves the partitioning of carbon into the residual austenite, the carbon content of the hard phase region was estimated on the assumption that the proeutectoid ferrite contained 0.02% carbon in solid solution. The latter assumption is approximate since the exact carbon content of the ferrite will depend on the cooling rate from the transformation temperature. The hardenability of the residual austenite, which is expected to be a sensitive function of its carbon content, will therefore also be a function of the volume fraction of transformation to ferrite. Hence, microstructural differences can be expected with varying ferrite volume fractions. This is particularly true for the present steel where the very low average carbon content imparts poor hardenability.

Air cooling from the austenitising temperature resulted in a microstructure of proeutectoid ferrite and extremely small islands of fine pearlite, the lamellae of which could be resolved by

transmission electron microscopy. The volume fraction of the pearlitic phase was approximately 0.03. (Fig.VIII.5).

Direct quenching into water or iced-brine from 1130°C (well above the $Ae_3$ temperature) gave up to 23% upper bainite.(Fig.VIII.6). This bainite was similar to that observed in higher carbon silicon containing steels (Ch.I) and consisted of dislocated bainitic ferrite laths separated by discontinuous films of carbon-enriched retained austenite. Additionally, it seemed that the islands of residual austenite transformed into a single crystallographic variant of upper bainite, rather than several variants (partitioning behaviour) as was the more usually observed mechanism in higher carbon steels. The latter observation is probably a manifestation of the fact that the kinetics of bainitic ferrite growth are markedly accelerated by a decrease in carbon content, so that in contrast to the higher carbon silicon steels, the first variant to nucleate will develop rapidly and consume the whole of the austenite region. Furthermore, the particular variant corresponding to the adjacent proeutectoid ferrite will find nucleation relatively easier and will therefore be favoured. This is illustrated in fig.VIII.6 where the bainitic ferrite plate (arrowed) has the same orientation as the adjacent proeutectoid ferrite. The morphology and discontinuous nature of the austenite films is probably due to the low carbon contents involved.

When the quench rate was increased by quenching into agitated iced-brine from a higher austenitising temperature (1310°C), the volume fraction of bainite increased to about 0.35 since there was less time available for the proeutectoid ferrite transformation during the quench, fig.VIII.7.

Quenching from lower austenitising temperatures (970-920°C) into agitated iced-brine resulted in a hard phase microstructure consisting of platelet martensite separated by films of retained austenite. Autotempering was not evident in the martensite, which was occasionally found to be twinned, fig.VIII.8.

The ferrite grain size was measured by lineal analysis and the intersections of test lines with the interfaces between hard phase and proeutectoid ferrite were included in the determinations. It is seen from table VIII.2 that the effective ferrite grain size does not vary markedly despite the wide variation in transformation conditions. In view of this, and the fact that uniform elongation is essentially unaffected by ferrite

grain size (152), the latter is not taken into account in the analysis of mechanical properties that follows.

(ii) Mechanical Properties

The deformation parameters obtained are listed in table VIII.3. The true stress-true strain curves were found to be accurately represented by equation VIII.2. These curves are plotted in fig.VIII.9 and the variations of the strain hardening and strengthening coefficients as a function of the volume fraction of hard phase are plotted in fig.VIII.10. In the case of the air-cooled specimen, use of eqn.VIII.2 is only approximate and leads to an underestimation of flow stress at high strains. However, the disagreement is sufficiently small for the purposes of the following calculations. The data from the air-cooled specimen was taken to be approximately representative of the deformation characteristics of pure ferrite in the present steel since it contained only 3% pearlite.

The first stage of deformation was analysed in terms of eqn.VIII.3 when it was assumed that at $\varepsilon_t = 0.002$, there was zero plastic strain in the hard phase, fig.VIII.11a. This assumption was necessary due to the absence of data for this alloy in the pure bainitic or martensitic states; 100% transformation to these microstructures was impossible due to the low hardenability of the alloy used. By systematically varying $\sigma_y''$, $K_m$, $n_m$, it proved possible to estimate the most likely values of these parameters by noting the set which gave best fit with the experimental composite stress-strain parameters. Thus, the following values were deduced:

| Bainite | Martensite |
|---|---|
| $\sigma_y'' = 1000$ MPa | $\sigma_y'' = 1300$ MPa |
| $K_m = 5200$ MPa | $K_m = 6500$ MPa |
| $n_m = 0.300$ | $n_m = 0.327$ |

The above values are considered to be realistic for the high-silicon microstructures, and compare well with the values obtained for an Fe-0.3C-3Cu-1Si alloy, isothermally transformed at 510°C to give a microstructure of silicon upper bainite and some martensite (this work was done by the present author during the early stages of the investigations of Ch.I, in order to establish a suitable experimental alloy for such investigations). The strain hardening coefficient in the latter microstructure was

found to be 0.48, the strengthening coefficient was 3130 MPa and the yield stress was 980 MPa.

Comparison of the experimental data with the values predicted by Tomota's theory using the above parameters, is illustrated in fig.VIII.11. Using the above deformation parameters, Mileiko's theory was found to overestimate considerably the composite strain hardening coefficients (at f = 0.1, $n_c$ = 0.21, and at f = 0.2, $n_c$ = 0.23). The reason for this can be understood from fig.VIII.12, which shows the variation of plastic strain in the two components. In the present steel, the deformation characteristics of the bainite and martensite on the one hand, and ferrite on the other, are sufficiently different to give extremely inhomogeneous strain distribution. Thus much of the deformation is concentrated in the ferrite. Since the intrinsic strain hardening coefficient of the latter is low, the general composite strain hardening coefficient will be lower than that predicted by an equal strain deformation model. The requirements of Mileiko's theory are clearly not justified with the present steel and agreement is poor.

Tomota's theory, however, gives good agreement with the experimental data and this reflects the more general applicability of the model to dual-phase steels. (It should be noted that while the failure to obtain 100% hard phase microstructures in the present experimental steel prevented the full predictive use of Tomota's theory, the calculated best fitting deformation parameters for the hard phases concerned are realistic.)

From table VIII.3 it is noted that the uniform elongation (as determined by measurements made on the gauge length well away from the necked region) does not in fact correspond to the magnitude of the strain hardening coefficient, but shows a negative correlation. This is attributed to the fact that the hard phases concerned fail prematurely in a non-ductile manner due to the rapid strain hardening.

(VIII.5) Summary

The applicability of Mileiko's theory to dual-phase steels has been compared with that of a more general two phase deformation model due to Tomota et al. Published data on dual-phase steels was found to be consistent with the latter model, with the predicted behaviour also being very similar to that found using Mileiko's theory. The apparently good agreement between the experimental results and the predictions using Mileiko's theory was shown to be due to the approximately homogeneous strain distribution (a necessary assumption of Mileiko's model) in the hard and soft phases of the steels whose data was analysed. The greater applicability of Tomota's theory is clear, not only from its less restrictive assumptions as far as dual-phase steels are concerned, but because by using an experimental steel it was demonstrated that Tomota's theory could be equally applied to situations of inhomogeneous strain distribution whereas that of Mileiko expectedly gave poor agreement.

The microstructure of the hard phases obtainable in the experimental high-silicon dual-phase steel used for the above analysis were also characterised in detail by transmission electron microscopy. Depending on the heat treatment condition the hard phase structures were identified either as martensitic plates separated by thin films of retained austenite, or as carbide-free upper bainitic ferrite plates, also associated with carbon-enriched retained austenite.

TABLE VIII.1

| Symbol | Meaning |
|---|---|
| $\sigma'_y$ | True yield stress for softer phase |
| $\sigma''_y$ | True yield stress for harder phase |
| $f$ | Volume fraction of harder phase |
| $E$ | Young's modulus, taken to be 210 GPa |
| $\upsilon$ | Poisson's ratio, taken to be 0.33 |
| $\varepsilon'_p$ | True plastic strain in softer phase |
| $\varepsilon''_p$ | True plastic strain in harder phase |
| $\varepsilon'_{p(II)}$ | Critical plastic strain in soft phase to start yield in hard phase |
| $\varepsilon_{p(II)}$ | Critical average plastic strain to start yield in hard phase |
| $\bar{\varepsilon}_p$ | True average plastic strain |
| $Y(I)$ | True average stress at the onset of flow in soft phase |
| $Y(II)$ | True average stress at the onset of flow in hard phase |
| $\sigma^A_{33}$ | True applied stress |
| $\delta\varepsilon'_p$ | Strain increment in soft phase |
| $\delta\varepsilon''_p$ | Corresponding strain increment in hard phase |
| $\sigma'_f$ | True flow stress in soft phase |
| $\sigma''_f$ | True flow stress in hard phase |
| $A$ | $E(7 - 5\upsilon)/(10[1 - \upsilon^2])$ |
| $\varepsilon_t$ | Total true strain |
| $n$ | Strain hardening coefficient |
| $K$ | Strengthening coefficient |
| $m$ | Subscript denoting hard phase |

TABLE VIII.2**

| Heat Treatment | (C) | Volume fraction of hard phase | Grain size μm |
|---|---|---|---|
| a) 10 min @ 1130°C, AC | .62 | .03 | 23 |
| b) 10 min @ 1130°C, WQ | .11 | .22 | 16 |
| c) 10 min @ 1130°C, IBQ | .11 | .23 | 14 |
| d) 5 min @ 1300°C, AIBQ | .08 | .33 | 18 |
| e) 10 min @ 920°C, AIBQ | .25 | .09 | 30 |
| f) 10 min @ 970°C, AIBQ | .16 | .15 | 24 |
| g) 10 min @ 935°C, AIBQ | .21 | .11 | 22 |

**Notation

WQ = Water Quenched

AC = Air cooled

IBQ = Iced Brine Quench

AIBQ = Agitated Iced Brine quench

(C) = Carbon content of the hard phase region assuming that the carbon level in the proeutectoid ferrite is 0.02 wt.pct.

Specimen (a) contained pearlite, (b),(c), and (d) contained upper bainite and (e), (f) and (g) contained martensite.

TABLE VIII.3

| | n | K/MPa | UTS/MPa | True uniform elongation | True stress at ε = 0.002/MPa |
|---|---|---|---|---|---|
| a) | 0.066 | 504 | 529 | 0.153 | 337 |
| b) | 0.144 | 956 | 657 | 0.119 | 385 |
| c) | 0.153 | 1042 | 674 | 0.106 | 397 |
| d) | 0.174 | 1322 | 738 | 0.075 | 435 |
| e) | 0.132 | 839 | 629 | 0.142 | 372 |
| f) | 0.165 | 1041 | 659 | 0.102 | 368 |
| g) | 0.156 | 1005 | 656 | 0.102 | 383 |

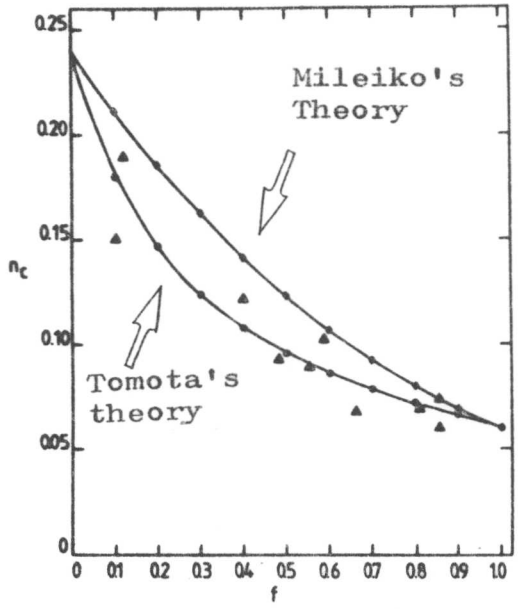


Figure VIII.1
Composite strain hardening coefficient vs. volume fraction of hard phase. The triangular points are from ref.154.

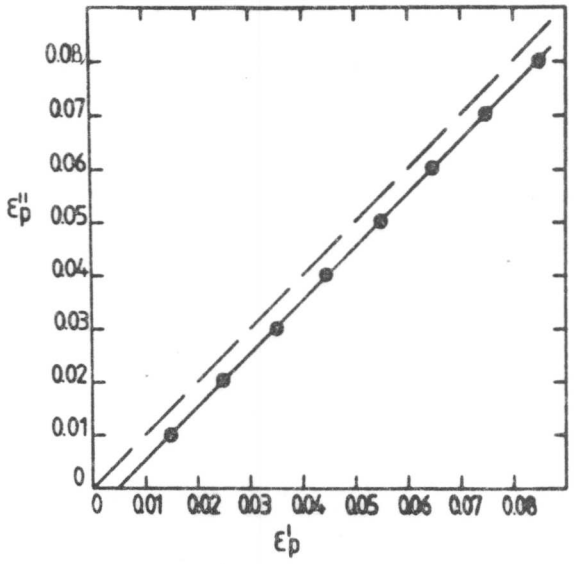


Figure VIII.2
Calculated cumulative plastic strain in the hard phase vs. that in the soft phase. The dashed line represents an equal strain situation.

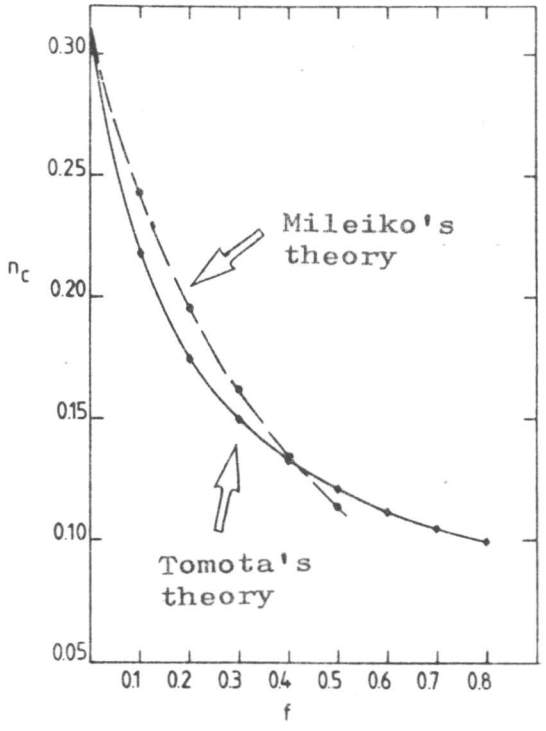


Figure VIII.3
Composite strain hardening coefficient vs. volume fraction of hard phase using the parameters listed in ref.155.

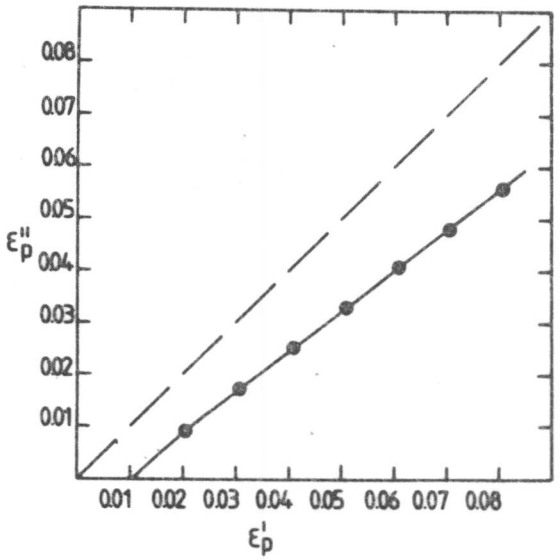


Figure VIII.4
Calculated cumulative plastic strain in the hard phase vs. that in the soft phase. The dashed line represents an equal strain situation.

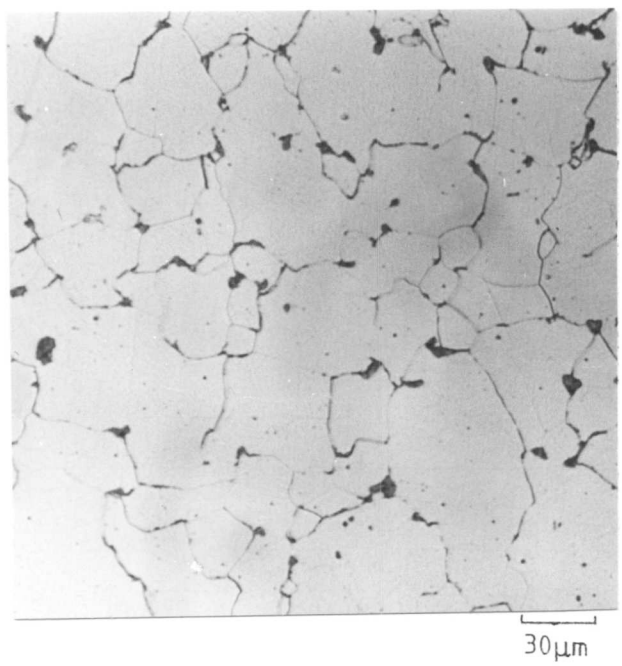


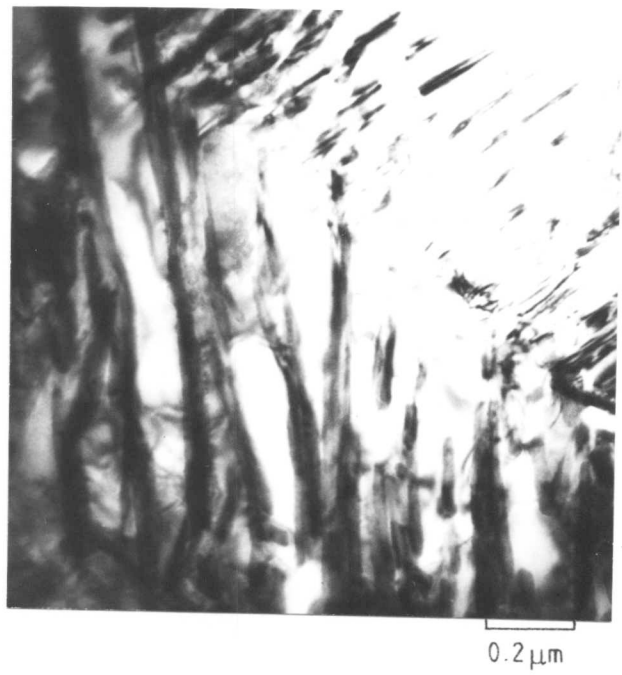


(a) (b)

Figure VIII.5

Air cooled following austenitisation at 1130°C for 10 minutes.

(a) Optical micrograph.

(b) Bright field transmission electron micrograph, showing an island of pearlite.

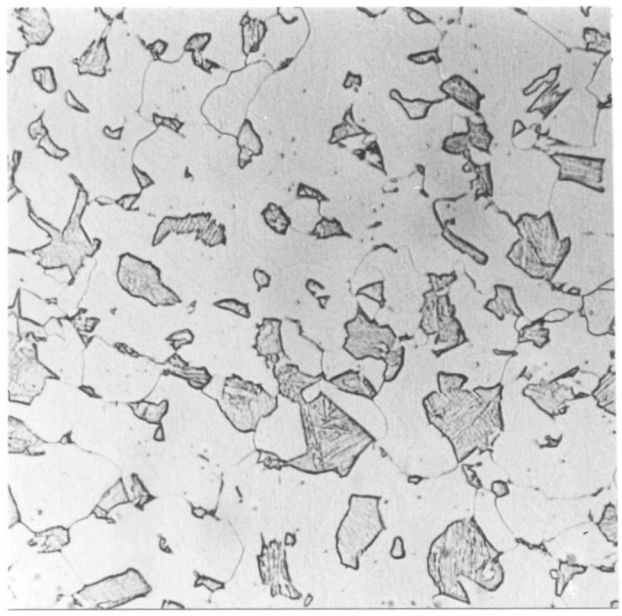


(a)

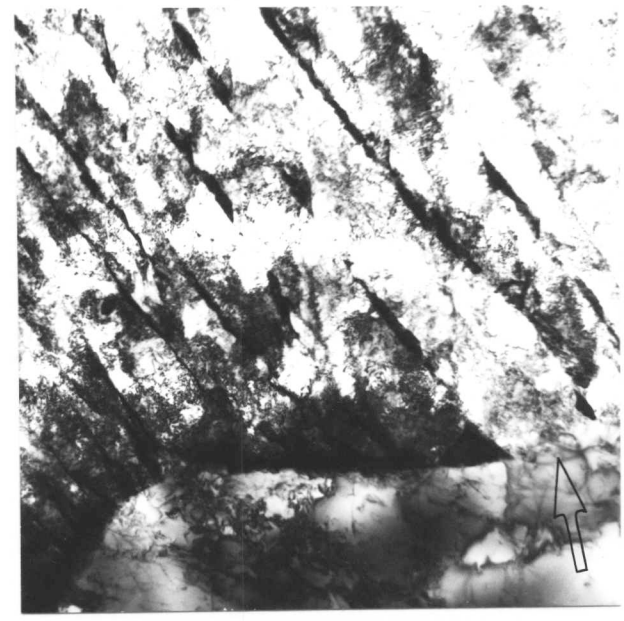


(b)

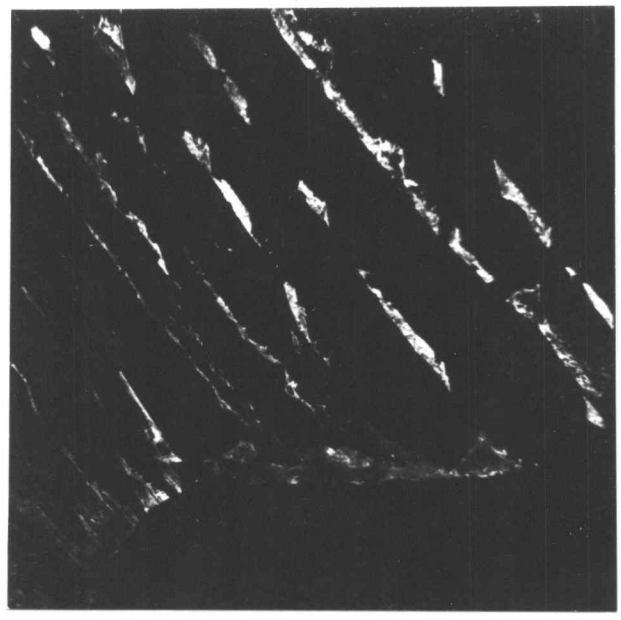

(c)

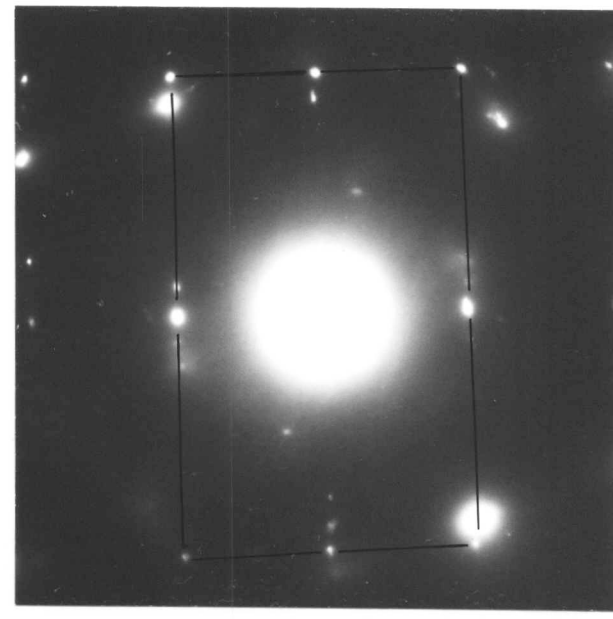

(d)

Figure VIII.6

Water quenched following austenitisation at 1130°C for 10 minutes.

(a) Optical micrograph.

(b) Bright field transmission electron micrograph.

(c) Corresponding retained austenite dark field image.

(d) Corresponding diffraction pattern: a $\langle\bar{1}12\rangle$ austenite zone is outlined.

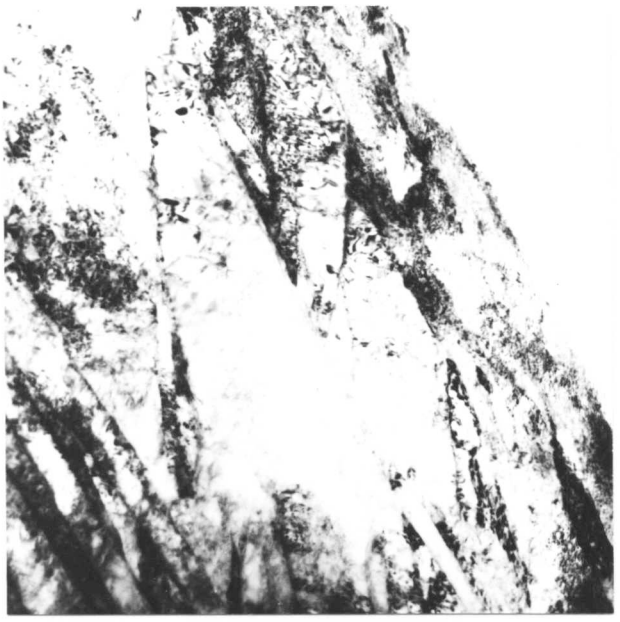

(8c)

(8d)

0.2μm

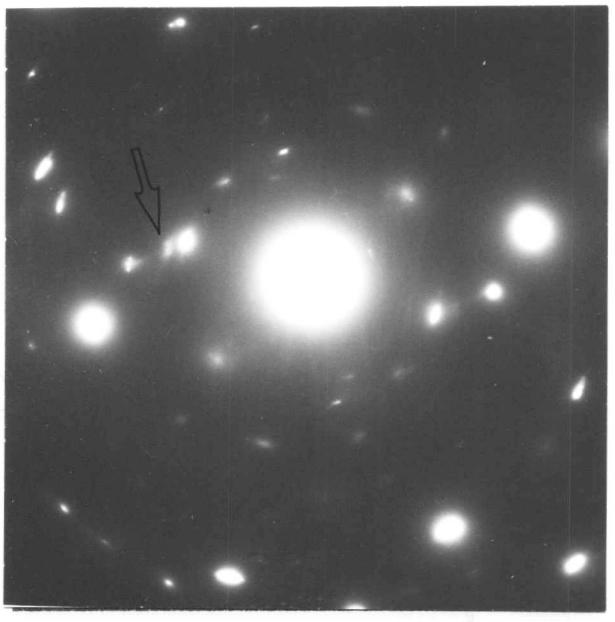

(8e)

Figure VIII.8

(c) Bright field image of an island of martensite.

(d) Corresponding retained austenite dark field image.

(e) Corresponding diffraction pattern. The arrowed spot is a {200} austenite reflection.

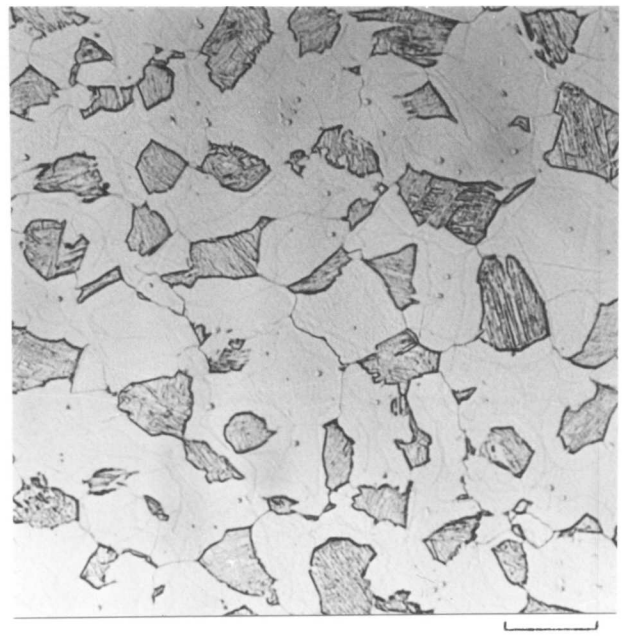


Figure VIII.7

Optical micrograph of specimen austenitised at 1300°C for 10 minutes and quenched into agitated iced brine.

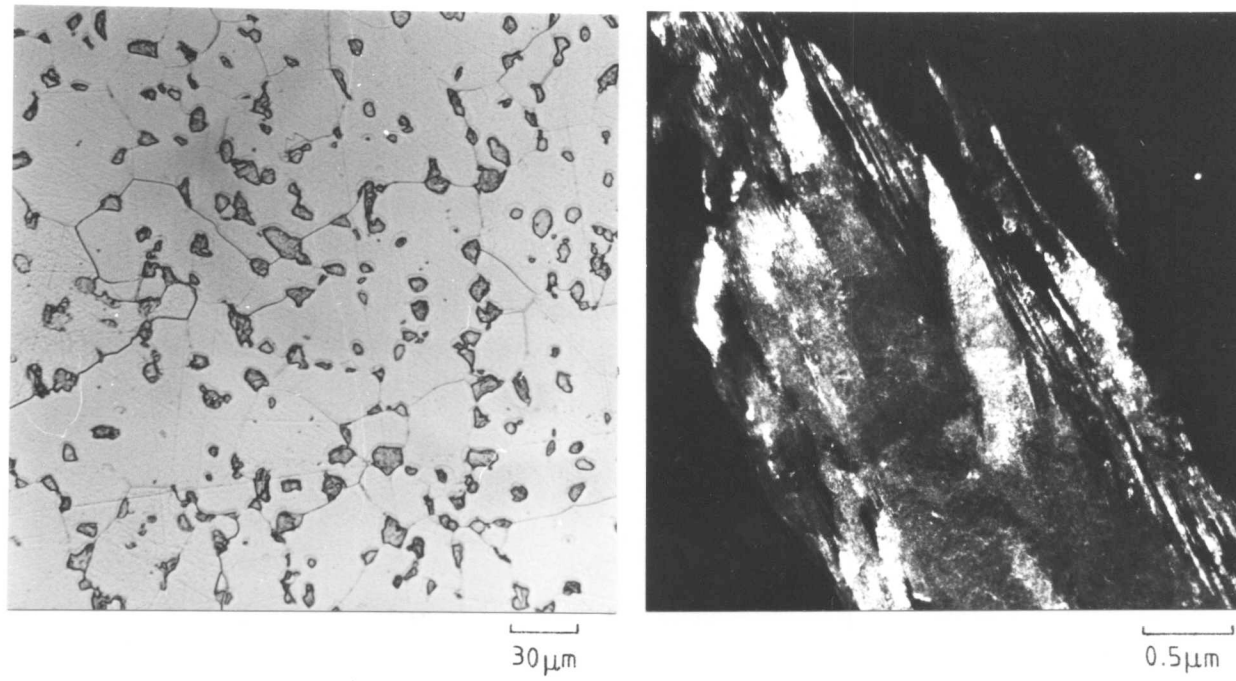


(a) (b)

Figure VIII.8a-e.

Austenitised at 935°C for 10 minutes followed by a quench into agitated iced brine.

(a) Optical micrograph.

(b) Dark field image of twins in martensite.

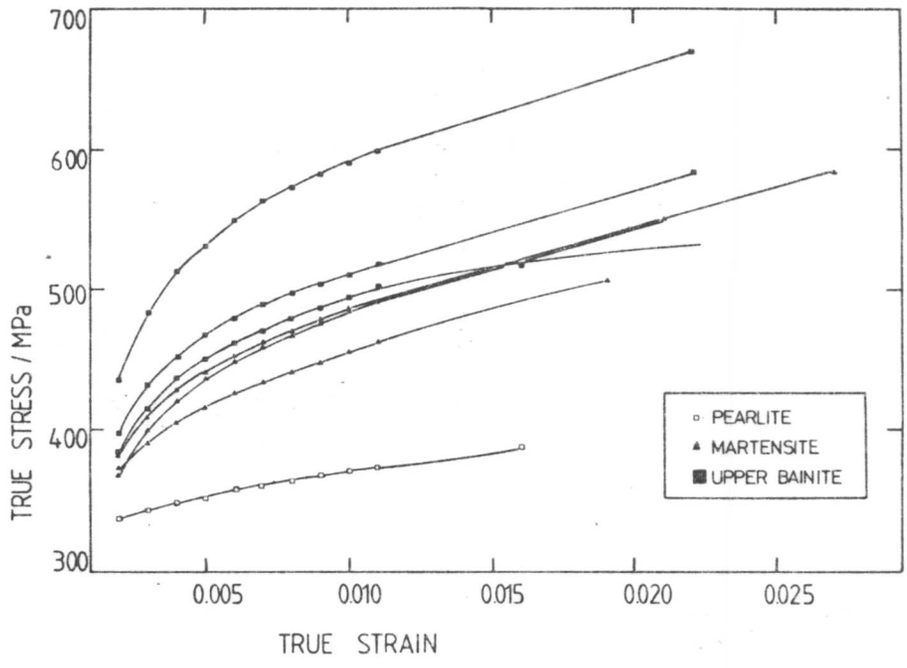


Figure VIII.9
True stress-true strain curves for the various microstructures examined.

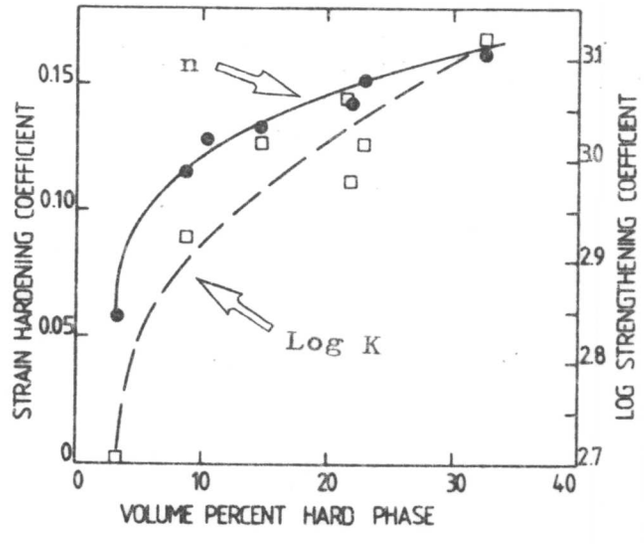


Figure VIII.10
The variations of strengthening and strain hardening coefficients as a function of the volume fraction of hard phase present. The dashed line represents the variation of the strengthening coefficient.

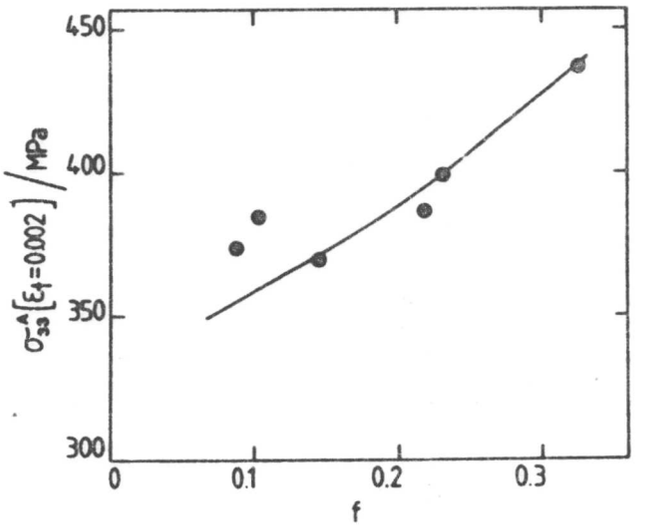


Figure VIII.11a

$\sigma_{33}^{A}$ vs. volume fraction of hard phase. The line is calculated using Tomota's theory.

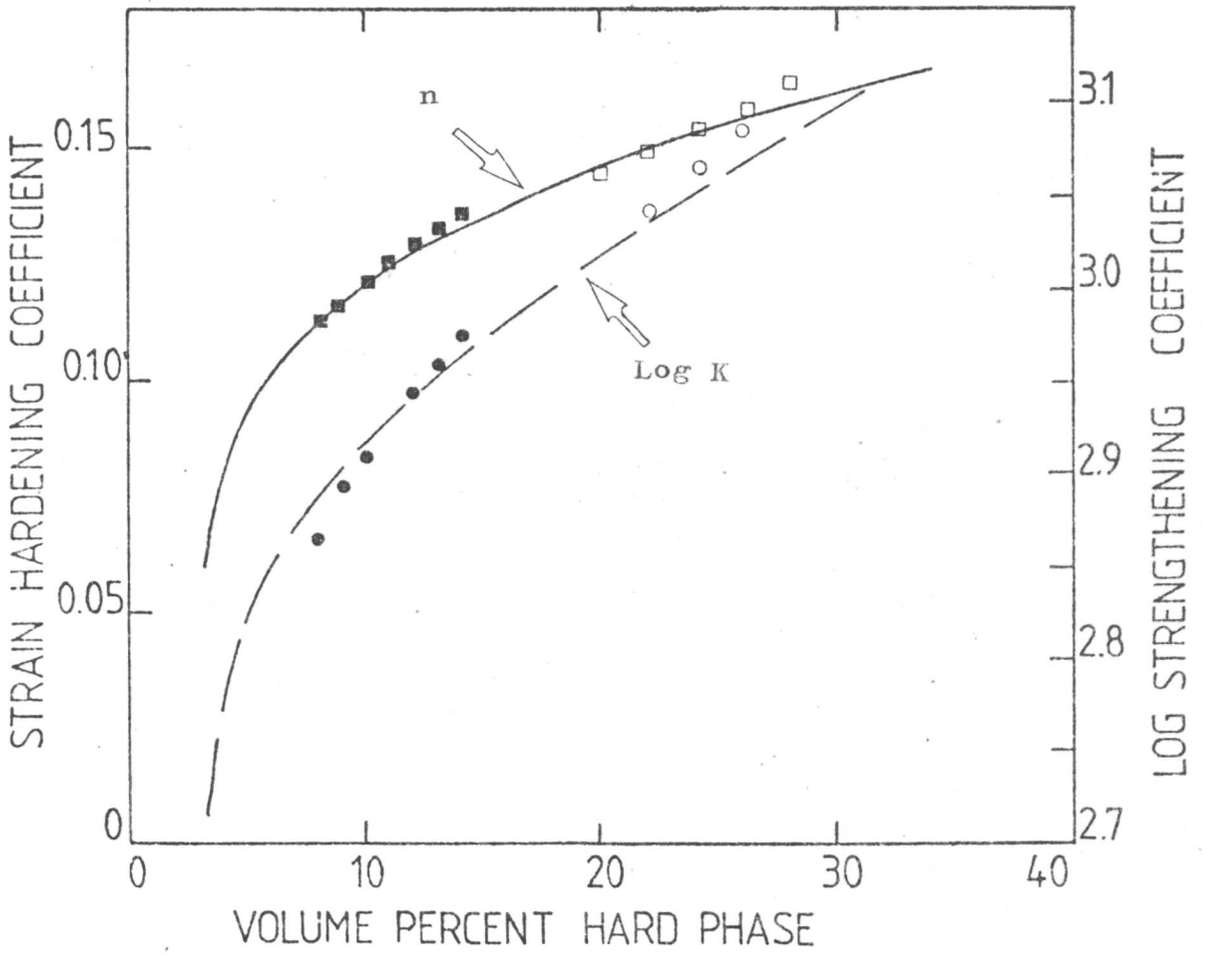


Figure VIII.11b

Best fit calculated values of strengthening and strain hardening coefficients obtained suing Tomota's theory vs. volume fraction of hard phase. The filled points refer to martensite, the open points to bainite and the lines represent the experimental curves from fig.VIII.10.

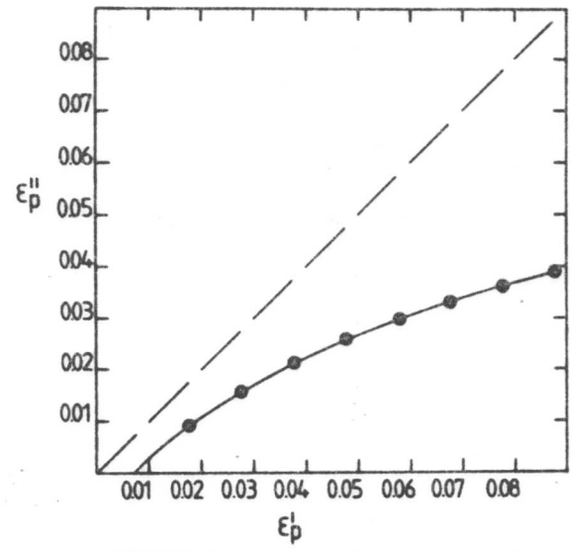


(a)

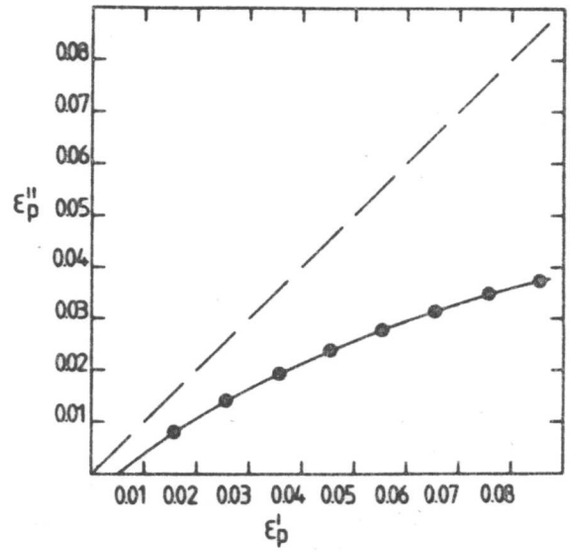


(b)

Figure VIII.12
Calculated cumulative plastic strain in the hard phase vs. that in the soft phase.
(a) Hard phase of martensite.
(b) Hard phase of bainite.

# CHAPTER NINE

## GENERAL CONCLUSIONS AND PROPOSED FURTHER RESEARCH

The bainite and martensite transformations in low alloy steels have been investigated, with the general aim of gaining a better understanding of the associated retained austenite. In this chapter, it is intended to summarise the results obtained and to discuss the implications of the conclusions reached, with respect to future work.

### (IX.1) The Bainite Transformation

An experimental silicon steel was used in a detailed study of the bainite transformation, in an attempt to resolve the controversy surrounding the transformation mechanism, at least to the extent that the results may be usefully applied to the problem of retained austenite. The high silicon level in the experimental alloy ensured the retention of austenite since the post-bainitic partitioning of carbon into residual austenite dominated over reactions involving the precipitation of carbides.

The results obtained were found to be consistently in favour of a displacive transformation mechanism rather than one involving the diffusional migration of disordered ledges on the apparent habit plane (i.e. reconstructive mechanism).

Dilatometry and transmission electron microscopy showed the overlap of distinct ferrite-pearlite and upper bainite 'C' curves; the compatibility of kinetic and microstructural definitions of bainite was also demonstrated. The existence of a well defined $B_s$ temperature and an incomplete reaction phenomenon was confirmed, and the verification of separate C-curves for upper and lower bainite not only indicated different modes of displacive transformation for upper and lower bainite, but also revealed two incubation bays, in addition to that at the $B_s$ temperature, which cannot be explained by any solute drag model.

Microstructural examination indicated that the sheaf of upper bainite (which had the appearance of a plate on the scale of optical microscopy) in fact consisted of smaller displacive sub-units; these were, for the most part of their interfaces, separated by carbon enriched films of retained austenite. The morphology and distribution of the retained austenite, and the scale of the microstructure were found to be inconsistent with growth by the migration of ledges (of the type envisaged

by the reconstructive school) along the planar partially-coherent faces of bainitic ferrite platelets.

In contrast, the basic units of lower bainite were not found to be separated by retained austenite; each macroscopic plate appeared to consist of adjacently nucleated sub-units in parallel formation, such that they terminated at the plate tip in a set of spikes. Often, isolated 'sub-units' could also be found.

The cementite precipitate in the lower bainitic ferrite formed on many variants of the precipitation plane. This observation, together with other crystallographic evidence suggested that the precipitation occurred from a supersaturated ferrite matrix. At the same time, some partitioning of carbon also took place.

The sum of the evidence was subjected to a critical thermodynamic analysis which demonstrated that the results could only be rationalised in terms of a displacive mechanism, with partitioning of carbon occurring <u>after</u> the formation of fully supersaturated bainitic ferrite. It was possible not only to account for sympathetic nucleation, which seems to be a specific characteristic of the bainite transformation, but also to explain uniquely the nature of the incomplete reaction phenomenon. The limited size of the displacive sub-units in upper bainite was explained in terms of the friction stress associated with the motion of the transformation interface.

It seems therefore that the bainite transformation is a displacive transformation which can only occur at a certain degree of undercooling below the $T_o$ temperature. The undercooling required is lower than that associated with the athermal martensite transformation, primarily due to the higher available thermal activation at the $B_s$ temperature, and because of specific differences in nucleation behaviour - i.e. bainite initially nucleates at prior austenite grain boundaries, with subsequent nucleation being sympathetic. The relatively low driving force at the $B_s$ temperature leads to a limited sub-unit size, the limitation coming into force when the chemical free energy change can no longer drive the transformation interface through the myriad of accommodation defects that are found to accompany the formation of bainite. The isothermal character of the bainite transformation arises since new sub-units can only sympathetically nucleate when the carbon concentration in the vicinity of the prior sub-unit (i.e. the carbon build-up resulting from post-

bainitic partitioning) is reduced by diffusion to a sufficiently low level such that displacive transformation is thermodynamically allowed. At a certain degree of transformation (depending on temperature and alloy composition), the carbon content of the austenite will reach a level such that the $T_o$ condition is transgressed, and displacive transformation ceases. This is then the incomplete reaction phenomenon, assuming that carbon depletion by carbide precipitation is prevented. The partitioning of carbon and the precipitation of carbides seem to be competitive reactions in this respect.

The above considerations represent a summary of the current understanding of the bainite transformation. However, it is evident that certain points need clarification. While the upper and lower bainite reactions have been identified as separate reactions, both occurring in a displacive manner, the differences in the mechanisms of displacive transformation are not obvious. It is anticipated that such differences would be manifested in the lattice invariant shears involved, but before these can be deduced, the crystallography of both the transformations needs to be rationalised in terms of the phenomenological theory of martensite. It would also be valuable to characterise the nature of the transformation interfaces, in order to resolve whether an interface glide mechanism or a pole mechanism is operative.

Initial attempts to characterise the surface relief of bainite have proved to be encouraging, although the scale of the sub-units is such that conventional interference microscopy has failed to give definite results. However, the use of dimensionally stable replicas from pre-polished and transformed surfaces may help.

It would be interesting to quantitatively express the growth of an individual sheaf of upper bainite, and compare the theoretical and experimental values of its shape anisotropy.

Finally, the results need to be generalised to steels not containing silicon.

## (IX.2) The Martensite Transformation

Retained austenite was detected in association with martensite in several low alloy steels examined by transmission electron microscopy and X-ray diffraction techniques. The austenite was present mainly as thin films between the martensite crystals.

However, the quantity and distribution of retained austenite varied between different steels. An examination of the inter-martensite crystallography indicated that the differences could be rationalised in terms of the relative orientations of martensite crystals bounding the austenite films. In steels with almost continuous films of inter-lath austenite, the degree of co-operative formation seemed limited in the sense that adjacent martensite units were of the same variant. When limited films of heterogeneously distributed austenite were observed, not only was the incidence of twin-related laths higher, but austenite was not in general observed between such laths. In a steel containing well organised packets of alternating twin-related laths, austenite could not be detected.

Some theoretical crystallography indicated that twin-related martensite orientations can only arise when the exact Kurdjumov and Sachs relationship is operative. However, the factors controlling the generation of any particular orientation relationship are not clear since the full crystallographic theory has not yet been successfully applied to dislocated martensites.

It thus appears that a high degree of mutual accommodation of transformation strains between adjacent variants reduces the propensity to retain inter-lath austenite, so that it is likely that mechanical stabilisation is a key factor controlling the stability of such films of austenite.

Initial results obtained using high alloy dislocated martensites suggest that for approximately the same $M_s$ temperature, the behaviour of the martensite transformation below $M_s$ is not a sensitive function of the habit plane crystallography despite the fact that the manner in which the prior austenite grain is geometrically partitioned depends on the habit plane multiplicity. This work was also found to be consistent with the idea that habit plane variations arise due to changes in the relative strengths of the austenite and martensite phases concerned.

A direct analysis of incipient twinning in a low alloy martensite indicated that such twinning originates from accommodation strains. The twins could not be described as intrinsic transformation features because the twin plane in the martensite was not found to uniquely correspond to a particular plane of mirror symmetry in the austenite, as required by the phenomenological theory. Furthermore, it was clear that the

intensity of twinning was highest when adjacent martensite units were twin-related; such a situation is expected to facilitate the nucleation of twins at the inter-martensite boundaries. Thus the earlier observation that austenite films cannot be readily detected between twin-related laths is not surprising since the lattices of such laths effectively interpenetrate. The interpenetration at the twin-related lath boundaries arises because the 'sympathetically nucleated' twins in a given variant adopt the lattice orientation of the adjacent variant.

The outstanding need as far as the martensite work is concerned is to define the detailed crystallography of low alloy martensites. The lack of adequate quantities of retained austenite and the fine scale of the microstructure have hindered the determination of such data. It is only when a complete set of crystallographic data becomes available that the phenomenological theory can be rigorously applied to obtain information on the transformation shears involved and to enable the calculation of parameters such as the degree of self-accommodation of shape strains as a function of crystallography. The up-quench technique (Ch.7) may help in this respect.

(IX. ) Bainite - Mechanical Properties

It has been established that the silicon upper bainite microstructure can exhibit superior toughness compared with tempered martensites of equivalent or lower yield strengths. The better toughness seems to arise due to a number of factors, including the fact that the microstructure is free from carbides; the latter are generally responsible for enhancing the nucleation of voids and cleavage cracks at the expense of toughness. Retained austenite is found to be beneficial when it is in the more stable film morphology (rather than the blocky morphology). Its presence between bainitic ferrite sub-units is conducive to the periodic deflection of propagating cracks; it is also possible that a TRIP effect operates in the vicinity of the crack tip. The absence of any substantial amount of interstitial carbon in the bainitic ferrite and the ultra-fine 'grain size' resulting from the displacive character of the transformation optimise the overall toughness.

The strength of the silicon upper bainite originates from the transformation induced dislocation structure and the ultra-

fine grain size. The intimate dispersal of films of austenite between bainitic sub-units (in identical orientation) seems to additionally strengthen the overall microstructure by preventing the easy transfer of slip across sub-units within a given sheaf.

It was demonstrated that the toughness is at its best when the ratio of film austenite to blocky austenite is highest. Since this ratio is a function of the volume fraction of bainitic ferrite, it was possible to establish an empirical toughness criterion in which the only unspecified quantity is the volume fraction of bainitic ferrite. However, this quantity is calculable using thermodynamics, assuming that the reaction is allowed to terminate at the isothermal transformation temperature used. Thus the toughness behaviour could, in essence, be predicted from a knowledge of the composition of the steel. This principle was verified for two experimental steels.

While the silicon bainite microstructure seems to provide a viable, cheap and better alternative to the tempered martensite based ultra-high strength steels, it should be noted that the fatigue properties have not yet been examined, although the high ultimate strength to yield strength ratio engenders optimism. In principle, it should be possible to derive a steel composition where the blocky morphology is completely eliminated; such a steel would be expected to exhibit better properties than even the steels examined in the present work.

## (IX.4) Martensite - Mechanical Properties

The microstructure and property changes accompanying the tempering of quenched low-alloy steels have been examined and correlated with the tempered martensite embrittlement (TME) phenomenon. TME was detected in an Fe-Mo-C steel and found to be controlled by the relatively coarser intralath cementite, rather than by the interlath cementite resulting from the decomposition of $<2\%$ retained austenite present as films between the martensite laths. In an Fe-V-C steel containing about 5% interlath retained austenite, TME was controlled by coarsening of the comparatively larger amount of interlath cementite resulting from thermal decomposition of the interlath retained austenite. In both cases fracture was translath, consistent with the crack nucleation role of cementite rather than that of providing an easy fracture path. In an Fe-Mn-Si-C steel containing

negligible retained austenite and fine carbides, TME was not found. Furthermore, embrittlement could not be associated with the transition from ε carbide to cementite.

It would be very interesting to quantify the relative coarsening rates of inter-and intra-lath carbides, as a function of the quantity of retained austenite and the potency of carbide inhibitors (such as silicon). This could then be directly related to the magnitude and shape of any TME troughs.

The extent of the TME effect with respect to tempering temperature is important since there are conflicting requirements of a low tempering temperature (consistent with high strength requirements) and the need to be beyond the TME trough. While ideally TME should be eliminated, another approach might involve modifications such that the TME trough would be extremely narrow and well defined. In this respect, the inter-lath dependence of TME is more desirable, as in the Fe-V-C steel.

# APPENDIX I

## THE IDENTIFICATION OF A NEW CARBIDE IN A SILICON CONTAINING STEEL

Isothermal transformation of an Fe-0.43C-3Mn-2.12Si alloy at 350°C gave a microstructure consisting of a lamellar aggregate of dislocated bainitic ferrite plates separated by films of carbon-enriched retained austenite (Ch.I). Tempering this structure at 500°C for 20 minutes led to the diffusional decomposition of the retained austenite to an unknown carbide phase and ferrite. This microstructure is illustrated in figure I.9a.

The carbide proved difficult to identify using conventional selected area electron diffraction due to the large number of crystallographic variants that contributed to the diffracted intensity from the area selected. The problem could not be simply overcome by using a smaller selected area aperture because the spherical aberration of the objective lens limits the size of such an aperture to approximately 0.5μm, at an operating voltage of 100 kV.

However, if the electron beam is condensed such that only the area of interest is illuminated, the diffracted intensity will arise mainly from that area. In principle, the spot size of the condensed beam is limited only by the resolution of the objective lens (159,160) although in practice the source of diffraction information will be larger due to beam spreading within the foil. For the present purposes, a spot size of 200 Å was found to be sufficient to resolve between the carbide particles (using a Philips EM300 electron microscope, operated at 100 kV).

One disadvantage of the above technique is that it leads to a broadening of the diffracted spots, as observed in the back focal plane of the objective lens. This is because a very small area is being illuminated, and the effect is directly analogous to the X-ray line broadening due to small crystallite size. Nevertheless, this setback did not deter the approximate determination of the crystal structure and parameters.

Some representative diffraction patterns are presented in figure AI.1. The camera constants were calibrated using ferrite reflections, and a set of 'd' spacings and angular relationships were obtained.

A literature search gave the following set of known iron carbides (which could also contain certain amounts of silicon or manganese):

| Crystal Structure | Parameters | Reference |
|---|---|---|
| Hexagonal | a = 11.7 c = 10.8Å | 161 |
| Hexagonal | a = 9.81 c = 8.48 | 162 |
| Hexagonal | a = 6.9 c = 4.8 | 163 |
| Hexagonal | a = 6.4 c = 9.6 | 164 |
| Hexagonal | a = 4.77 c = 4.35 | 165 |
| Hexagonal | a = 2.75 c = 4.35 | 165 |
| Hexagonal | a = 2.76 c = 4.36 | 165 |
| Hexagonal | a = 6.27 c = 21.4 | 165 |
| Orthorhombic | a = 8.8 b = 9 c = 14.4 | 166 |
| Orthorhombic | a = 7.89 b = 4.6 c = 7.2 | 167 |
| Orthorhombic | a = 4.525 b = 5.087 c = 6.743 | 165 |
| Orthorhombic | a = 9.04 b = 15.66 c = 7.92 | 165 |
| Orthorhombic | a = 3.82 b = 4.72 c = 12.5 | 165 |
| Orthorhombic | a = 6.5 b = 7.7 c = 10.4 | 168 |
| Orthorhombic | a = 14.8 b = 11.4 c = 8.5 | 168 |
| Cubic | a = 3.88 | 165 |
| Monoclinic | a = 11.563 b =4.573 c = 5.058 $\beta$ = 97.44° | 165 |
| Hexagonal | a = 6.882 b = 4.54 | (Source unknown) |

Unsuccessful attempts were made to consistently index all available diffraction patterns to each of the above crystal structures. From the number of different low order reflections observed, it appeared that the crystal had a low symmetry, possibly monoclinic, if not worse. Since even the monoclinic structure is difficult to solve, the task was begun by assuming that the crystal had orthorhombic symmetry, but this proved futile, and a computer procedure was adopted with the assumption of monoclinic symmetry. In an attempt to simplify the calculations, it was assumed that the lowest order spacing observed by electron diffraction corresponded to one of the fundamental parameters of the unit cell (b). The other three parameters (a,c,$\beta$) were then systematically varied until a fit was obtained with all the available d-spacing and relative angle data.

The following parameters were thus deduced:

$a = 8.1\text{Å}$ $b = 10.4$ $c = 7.0$ $\beta = 107.2^{\circ}$

The agreement with experimental results is as follows:

| Experimental | Calculated | Error % | Zone axis |
|---|---|---|---|
| (100) 7.73 | 7.73 | - | 011 |
| $(01\bar{1})$ 5.54 | 5.62 | 1.4 | |
| (100)*$(01\bar{1})$ 75° | 75.6° | | |
| (010) 10.41 | 10.41 | - | $\bar{1}01$ |
| (101) 4.22 | 4.44 | 5.25 | |
| (010)*(101) 90° | 90° | | |
| (111) 4.15 | 4.09 | 1.6 | $\bar{2}11$ |
| $(0\bar{1}1)$ 5.74 | 5.62 | 2.2 | |
| (111)*$(0\bar{1}1)$ 67° | 64.3° | | |
| (011) 5.774 | 5.62 | 2.7 | $2\bar{1}1$ |
| $(\bar{1}20)$ 4.18 | 4.31 | 3.1 | |
| (011)*$(\bar{1}20)$ 69° | 71.97° | | |
| (011) 5.79 | 5.62 | 3.2 | $2\bar{1}1$ |
| $(\bar{1}20)$ 4.18 | 4.31 | 3.1 | |
| (011)*$(\bar{1}20)$ 68° | 71.97 | | |
| (011) 5.39 | 5.62 | 4.3 | $2\bar{1}1$ |
| $(\bar{1}20)$ 4.26 | 4.31 | 1.2 | |
| (011)*$(\bar{1}20)$ 71° | 71.97 | | |

Note: All d-spacings are in Å, and (hkl)*(uvw) signifies the angle between the two planes indicated.

While further work would be useful to fully identify the carbide, it can be safely concluded that the above results represent a new carbide, whose detailed composition, relationship to the parent lattice and detailed crystal structure are as yet unknown. Furthermore, the errors involved in the above experiments and calculations are uncertain.

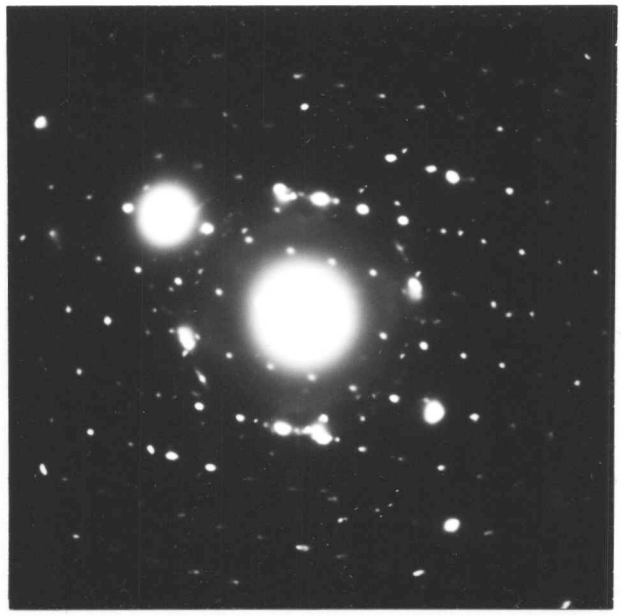

(a)

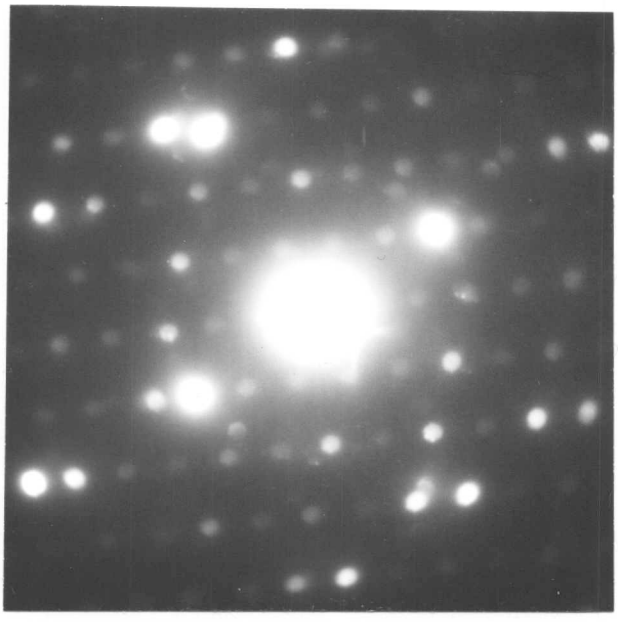

(b)

Figure A1.1

Convergent beam electron diffraction patterns from the carbide obtained after tempering silicon upper bainite at 500°C for 30 minutes.

(a) $[011]$ zone.

(b) $[2\bar{1}1]$ zone.

## APPENDIX II

### THERMODYNAMICS OF DISLOCATED MARTENSITES

Energy can be stored in polycrystalline martensitic specimens in the form of defects, interphase interfaces and coherency strains. Christian (169) considers that the calculated elastic coherency energy should give an approximate upper limit to the stored energy due to dislocations since the plastic deformation that leads to the formation of defects is driven by the coherency stresses.

It has recently been suggested that the energy stored in dislocated lath martensites is considerably greater than that in fully twinned plate martensites (170). The difference in stored enthalpy has been calorimetrically determined to be about 1150 J $mol^{-1}$, giving an absolute stored enthalpy of 1850 J $mol^{-1}$ since that of twinned martensite amounts to 700 J $mol^{-1}$ when both the twin interface energy (~ 100 J $mol^{-1}$, ref.170) and the elastic strain energy (600 J $mol^{-1}$, ref.169) are taken into account. This last value can be somewhat reduced if the plates form in some sort of a self accommodating manner (169), so that the stored enthalpy of lath martensite probably lies between 1250 and 1850 J $mol^{-1}$ (possibly at the higher end of this range since the crystallography of ferrous martensites is incompatible with complete self-accommodation).

In general, martensite transformations involve a certain degree of undercooling below the $T_o$ temperature (as discussed in Ch.II) prior to the onset of transformation at the $M_s$ temperature. This seems to allow the build up of a sufficient amount of driving force to account for the various energy factors discussed above, and perhaps also to provide the activation energy needed to overcome any nucleation barrier**. However, it was intuitively

---

** Christian (171) suggests that we do not know enough about the nucleation process to reach any conclusion about whether an additional appreciable driving force is needed for the nucleation of martensite.

---

felt that the value of stored energy deduced above may be too high when considered in terms of the available driving force, since even for substitutional alloy martensites the latter amounts to about 1260 J $mol^{-1}$ at the $M_s$ temperature. It was therefore decided to scrutinise the available calorimetric data and the results are presented below.

## Results and Discussion

Lee et al. (170) originally calculated the stored energy due to dislocations to be approximately consistent with the observed enthalpy difference between dislocated and twinned martensites. However, their calculations were found to be based on dislocation density values which were misquoted form the work of Kehoe and Kelly (172). Hence the stored energy due to the actual dislocation density was recalculated; additionally, the chemical driving force at $M_s$ was estimated using the thermodynamic procedures of (38,40,41). The specific equations used for the latter calculations were based on the Lacher (42), Fowler and Guggenheim (43) statistics. The results are as follows:

| Composition C | Mn | Si | $M_s$/°K | $-\Delta G$/J mol$^{-1}$ | $\rho$/m$^{-2}$ | E/J mol$^{-1}$ | Ref. |
|---|---|---|---|---|---|---|---|
| 0.01 | | | 830* | 1034 | $5\times10^{14}$ | 10 | 172 |
| 0.04 | | | 815* | 1060 | $8.9\times10^{14}$ | 18 | 172 |
| 0.06 | | | 806* | 1070 | $1.1\times10^{15}$ | 21 | 172 |
| 0.10 | | | 787* | 1061 | $1.6\times10^{15}$ | 31 | 172 |
| 0.022 | 4.3 | 0.95 | 738 | 586 | $3.9\times10^{14}$ | 8 | 86 |
| 0.035 | 4.6 | 0.29 | 703 | 680 | $4.6\times10^{14}$ | 9 | 86 |
| 0.058 | 4.8 | 0.30 | 698 | 630 | $7.1\times10^{14}$ | 14 | 86 |
| (C = 0.02-0.18) | | | 824-749* | 1040-1140 | $1.5\times10^{15}$ | 30 | 173 |
| 0.43 | 3.0 | 2.12 | 493 | 1420 | $5.4\times10^{15}$** | 108 | |

### Notes

1) The compositions are expressed in wt. pct.
2) The $M_s$ temperatures with asterisks are calculated using a regression equation from (174).
3) $\Delta G$ = The Chemical free energy change at $M_s$, calculated as indicated in the text.
   $\rho$ = Dislocation density. The last figure marked (**) is obtained by extrapolating the graph of (172).
   E = Stored energy due to dislocations, assuming that when $\rho = 5\times10^{16}$ m$^{-2}$, E = 1000 J mol$^{-1}$, as in (174).
4) The last column refers to the source of the information.
5) The data from (173) gives the estimated $\rho$ between lath boundaries, with the total being determined by resistivity measurements to be $0.3 - 0.9 \times 10^{16}$ m$^{-2}$ (see Appendix to ref.173).

Before considering the implications of the above data, it is noted that Christian (171) considers that whilst 1260 J $mol^{-1}$ is probably about right for the driving force at $M_s$ for substitutional ferrous alloys, the data of (175-6) indicates an appreciably higher value for interstitial alloys. However, for the low interstitial contents being considered here, the discrepancy between the calculated values (for the Fe-C alloys) and the data of (175-6) amounts (at most) to about 200 J $mol^{-1}$.

After examining the above results, Argent (178) has reconsidered the procedure for the calculation of dislocation densities from stored energy measurements, as follows:

Case 1

Considering the dislocations in BCC iron to be dissociated as

$$\frac{a}{2}[\bar{1}\bar{1}1] \rightarrow \frac{a}{6}[\bar{1}\bar{1}1] + \frac{a}{3}[\bar{1}\bar{1}1]$$

and

$$\frac{a}{2}[111] \rightarrow \frac{a}{6}[11\bar{1}] + \frac{a}{3}[112]$$

and using the Moore and Khulmann-Wilsdorf (179) formula, i.e.

$$E = \frac{\rho\mu b^2}{4\pi K}\left(\ln \frac{R}{r_o} + 1.6n\right)$$

where E is as defined above,

- $\mu$ = Shear modulus, $8.3 \times 10^{10}$ N $m^{-2}$
- b = Burgers vector, $a\sqrt{3}/6$ and $a\sqrt{3}/3$
- a = Ferrite lattice parameter, $2.861 \times 10^{-10}$ m
- R = Outer radius of dislocation strain field, $10^{-6}$ m
- $r_o$ = Inner radius of dislocation strain field, $10^{-10}$ m
- K = 1 for screw dislocations and $(1 - \upsilon)$ for edge dislocations, $\upsilon$ being the Poissons ratio.
- n = Number of dislocations in a pile up, taken to be 20.

The above parameters are more realistic than the ones used in the original calculation (170). Thus, for screw dislocations dissociated in the above manner, the energy per mole per unit dislocation density ($\varkappa$) is found to be $6.61 \times 10^{-14}$ J $mol^{-1}$ $m^2$ compared with the original value of $2 \times 10^{-14}$ J $mol^{-1}m^2$. (Note: $\varkappa = E/\rho$)

Case 2

If the dislocations are not dissociated, but are all of screw character, the value of $\varkappa$ becomes $1.2 \times 10^{-13}$ J $mol^{-1}m^2$, and for undissociated edge dislocations this amounts to $1.7 \times 10^{-13}$ J $mol^{-1}m^2$.

It should be noted that the above formula yields the highest magnitude of dislocation energy for a given dislocation density

when compared with two other available equations (180,181) and hence is most compatible with the fact that the dislocations densities are lower than originally thought by Lee et al. If we now accept the highest value of $\varkappa$ from the above calculations, i.e. $1.7 \times 10^{-13}$ J $mol^{-1} m^{2}$, all the 'E' values tabulated earlier would have to be multiplied by a factor of 8.5. On doing this, it was still found that the energy due to dislocations could not account for the excessive stored energy of lath martensites relative to fully twinned plate martensite. The results in fact strongly support Christian's (169) conclusion that any difference in stored energies of lath and plate martensites is likely to have its origin in the better elastic accommodation of the plates.

Despite this, there are a number of difficulties in accepting the magnitude of the excess stored enthalpy found by Lee et al. Assuming that the entropy of line defects may be neglected, the total stored enthalpy often exceeds the available driving force, as tabulated above. If much of the stored enthalpy (1250-1850 J $mol^{-1}$) is present as elastic energy (since the calculations suggest that the stored energy due to dislocations is rather low), then using the procedure and parameters given in (169), a shear component of the unconstrained invariant plane strain shape deformation of at least 0.26 can be calculated. It is most unlikely that this magnitude of strain can be elastically tolerated in the austenite, particularly since the austenite will have a low flow stress at the relatively high $M_s$ temperatures associated with lath martensites.

It is possible that Lee et al. overestimated the stored energy values since they did not take account of carbide precipitation; many of their electron micrographs of high carbon plate martensites show significant amounts of carbide precipitation. While this would not apply to the Fe-30.3Ni alloy which they also studied, it should be noted that their estimate of stored energy was based on a regression analysis of all the results from many alloys, so that the influence of any one alloy may not be noticeable in the final result**.

---

**Argent (178) believes that for the particular transformation conditions used in the experiments of (169), fully twinned martensite was obtained in the Fe-30.3Ni alloy. The present author had suggested that this particular alloy does not give rise to fully twinned plates, in accordance with (182).

In conclusion it is suggested that the excess stored enthalpy of dislocated lath martensites may be lower than that found by Lee et al. (169), and that the dislocation substructure does not form a major part of the stored energy.

The present analysis does, however, suggest an interesting experiment. $\{225\}_\gamma$ plate martensite has a displacement vector which essentially lies in the habit plane, so that interaction between different variants is minimal, a fact which is reflected in the absence of a burst phenomenon. It would be extremely interesting to compare the stored energy of this martensite with say the fully twinned $\{3\ 10\ 15\}_\gamma$ type martensite which forms in a beautifully self-accommodating manner.

# APPENDIX III

## THE STRUCTURE OF TWINS IN Fe-Ni MARTENSITES

The martensite plates found in Fe-31Ni (wt.pct.) alloys are generally partially twinned (182). The twinned regions correspond to the midrib of the plate whereas the peripheral regions have a dislocated substructure consisting of two sets of screw dislocations aligned along $\langle 111 \rangle_{\alpha'}$ directions (183).

It is found that the composition plane of the twin is a plane of the form $\{112\}_{\alpha'}$, and corresponds to a plane of mirror symmetry in the austenite, as required by the phenomenological theory of martensite when type 1 twinning is involved (182). Additionally, if the composition plane is taken to be the twin plane, substitution into the phenomenological theory generates an invariant martensite habit plane that is consistent with the trace of the observed midrib plane (182).

However, the assumption that the composition plane corresponds to the twinning plane has recently been challenged (184). It has been proposed that the 'twin' in fact consists of a three dimensional stack of $\frac{a}{6}\langle 111 \rangle_{\alpha'}$ partial dislocations, such that the twinning plane (i.e. the plane on which the partials move), is a $\{11\bar{2}\}_{\alpha'}$ plane which is different from the composition plane although it belongs to the same $\langle 111 \rangle_{\alpha'}$ zone. However, the experimental evidence of (184) is based on the assumption that the twinning elements ( $\langle 11\bar{1} \rangle_{\alpha'}$ , $\{112\}_{\alpha'}$ ) can be determined from the observation of symmetry axes relating the twin and matrix lattices. Unfortunately, the intrinsic BCC twin/matrix symmetry allows three variants of $\{11\bar{2}\}_{\alpha'}$ planes, related by a common $\langle 111 \rangle_{\alpha'}$ axis, across which the twin and matrix are related by reflection.

This does not, however, rule out the basic hypothesis of (184) since the twinning elements are as yet undetermined. Nevertheless, any such model would have to explain a) the appearance of a single twin variant per plate, such that the composition plane is uniquely related to the specific martensite habit plane, and b) the driving force behind the formation of such twins.

The twinning element problem could, in principle, be resolved by measuring the shape deformation due to the twins, using dimensionally stable replicas taken from pre-polished and transformed specimens.

## KEY REFERENCES


1. R.F. Hehemann, K.R. Kinsman, H.I. Aaronson: Met. Trans., 1970, vol.3, pp.1077-1093.
2. H.I. Aaronson: 'The Mechanism of Phase Transformations in Crystalline Solids, Institute of Metals Monograph 33, 1968, p.270.
3. 1st Progress Report of Sub-Committee XI, ASTM Committee E-4; Proc. ASTM, 1950, vol.50, p.444.
4. 2nd Progress Report of Sub-Committee XI, ASTM Committee E-4; ibid., 1952, vol.52, p.543.
5. 4th Progress Report of Sub-Committee XI, ASTM Committee E-4; ibid., 1954, vol.54, p.568.
6. L. Habraken: Proc. 4th Int. Conf. on Electron Microscopy, 1958, p.621, Berlin.
7. R.M. Fisher: ibid., p.579.
8. F. B. Pickering: ibid., p.626.
9. K. Shimizu, Z. Nishiyama: Mem. Inst. Sci. Ind. Res. Osaka Univ., 1963, vol.20, p.43.
10. J.M. Oblak, R.F. Hehemann: 'Transformations and Hardenability in Steels' p.15, Climax Molybdenum Company, Ann Arbor, 1967.
11. B.A. Leontyev, G.V. Kovalevskaya: Phys. Met. Metallogr., 1974, vol.38, p.139.
12. N.A. Snurenskaya, L.I. Kogan, R.I. Etin: Phys. Met. Metallogr., vol.41, pp.1019 - 1028.
13. Der-Hung Huang, G. Thomas: Met. Trans., 1977, vol.8, p.1661.
14. N.F. Kennon: J. Aust. Inst. Metals, 1974, vol.19, pp.3 -18.
15. K.R. Kinsman, H.I. Aaronson: Transformations and Hardenability in Steels, p.39, Climax Molybdenum Company, Ann Arbor, 1967.
16. R.F. Hehemann: 'Phase Transformations', p.397, ASM, Metals Park, Ohio, 1970.
17. R. Le Houiller, G. Begin, A. Dube: Met. Trans., 1971, vol.2 p.2645.
18. N.F. Kennon: Met. Trans., 1978, vol.9, pp.57 - 66.
19. G.R. Purdy: Acta Met., 1978, vol. 26, pp.477 - 486.
20. G.R. Purdy: Acta Met., 1978, vol. 26, pp.487 - 498.
21. B. Uhrenius: Scand. J. Met., 1977, vol.6, pp.83 - 89.
22. G.R. Speich: 'Decomposition of Austenite by Diffusional Processes', p.353, Interscience Publishers, New York, 1962.
23. W.S. Owen: Trans. ASM, 1954, vol.46, pp.812 - 829.
24. J. Gordine, I. Codd: J.I.S.I., 1969, vol. 207.1, p. 461.
25. R.M. Hobbs, G.W. Lorimer, N. Ridley: J.I.S.I., 1972, vol.210.2, p.757.

26. M.J. Dickson: J. App. Cryst., 1969, vol.2, p.176, also, Private Communication, Dr. L. Remy, Ecole Nationale Superireure Des Mines de Paris, 91003 Evry Cedex, France. 1977.
27. B.D. Cullity: 'Elements of X-ray Diffraction', 1st Edition, p.334, Addison-Wesley Publishing Co., 1956.
28. G.B. Olson, M. Cohen: Met. Trans., 1976, vol.7, p.1797.
29. Y. Ohmori, R.W.K. Honeycombe: Supp. Trans. ISIJ, 1971, vol.11, p.1160.
30. K.W. Andrews: Acta Met., vol.11, 1963, p.939.
31. B. Jacobson, A. Westgren: Zietschrift fur Physikalische Chemie, Badenstein Anniversary Volume, 1931, p.177.
32. N.C. Law: Ph.D. Thesis, University of Cambridge, England, 1977.
33. H.I. Aaronson, M.R. Plichta, G.W. Franti, K.C. Russell: Met. Trans., 1978, vol.9, p.368.
34. H.I. Aaronson: 'Decomposition of Austenite by Diffusional Processes', p.337, Interscience Publishers, New York, 1962.
35. W.L. Grube, S.R. Rouze: 'High Temperature - High Resolution Metallography', p.313, Gordon and Breach, New York, 1967.
36. S.R. Rouze and W.L. Grube: General Motors Corp., Warren, Mich., Private Communication toe H.I. Aaronson, referred to in (1).
37. K.R. Kinsman, E. Eichen, H.I. Aaronson: Met. Trans. A, 1975, vol.6A, p.303.
38. K.R. Kinsman, H.I. Aaronson: Discussion to ref.10.
39. C. Zener: Trans. AIME, 1946, vol.167, p.a50.
40. H.I. Aaronson, H.A. Domian, G.M. Pound: Trans. Met. Soc. AIME, 1966, vol.236, p.753.
41. H.I. Aaronson, H.A. Domian, G.M. Pound: Trans. Met. Soc. AIME, 1966, vol.236, p. 768.
42. J.R. Lacher: Proc. Cambridge Phil. Soc., 1937, vol.33, p.518.
43. R.H. Fowler, E.A. Guggenhiem: 'Statistical Thermodynamics', p.442 and preceeding, Cambridge Univ. Press, New York, 1939.
44. L. Kaufmann, E.V. Clougherty, R.J. Weiss: Acta Met., 1963, vol.11, p.323.
45. G.B. Olson, M. Cohen: Scripta Met., 1977, vol.11, p.345.
46. G.B. Olson, M. Cohen: Scripta Met., 1975, vol.9, p.1247.
47. A.T. Davenport: Republic Steel Research Centre, Project Report 12051, 1974.
48. L. Kaufmann, M. Cohen: Progress in Metal Physics, 1958, vol. 7, p.165.
49. G.B. Olson, M. Cohen: Met. Trans. A, 1976, vol.7A, p.1897.
50. G.B. Olson, M. Cohen: Met. Trans. A, 1976, vol.7A, p.1905.
51. G.B. Olson, M. Cohen: Met. Trans. A, 1976, vol.7A, p.1915.

52. M. Cohen: Met. Trans., 1972, vol.3, p.1095.
53. H. Knapp, U. Dehlinger: Acta Met., 1956, vol.4, p.289.
54. V. Raghavan, M. Cohen: Acta Met., 1972, vol.20, p.333.
55. D. Maclean: 'Mechanical Properties of Matter', John Wiley and Sons Inc., New York and London, 1962, p.8.
56. H.I. Aaronson, M.G. Hall, D.M. Barrett, K.R. Kinsman: Scripta Met., vol.9, 1975, p.705.
57. M. Shibata, L. Ono: Acta Met., 1977, vol.25, p.35.
58. J.W. Christian: 'Phase Transformations', York Conf., 1979, vol.1, No.11, Series 3, p.1, Inst. of Metallurgists, London.
59. M. Cohen, E.S. Machlin, E.V.G. Paranjpe: 'Thermodynamics in Physical Metallurgy', ASM, 1949, p.242.
60. E.S. Machlin: Trans. AIMME, 1954, vol.200, p.684.
61. J.W. Christian: 'The Theory of Transformation in Metals and Alloys', 1965, Pergamon Press, Oxford.
62. W.S. Owen, F.J. Schoen, G.R. Srinivasan: 'Phase Transformations', p.157, ASM, Metals Park, Ohio, 1970.
63. J.M. Rigsbee, H.I. Aaronson: Acta Met., 1979, vol.27, p.351.
64. J.M. Rigsbee, H.I. Aaronson: Acta Met., 1979, vol.27, p.365.
65. H.I. Aaronson, C. Laird, K.R. Kinsman: Scripta Met., 1968, vol.2, p.259.
66. F.B. Pickering: 'Phase Transformations', York Conf., 1979, vol.2, Series 3, No.11, p.VI.7.
67. D. Bhandarkar, V.F. Zackay, E.R. Parker: Met. Trans., 1972, vol.3, p.2619.
68. D. Fahr: Met. Trans., 1971, vol.2, p.1883.
69. W.W. Gerberich, P.L. Hemmings, V.F. Zackay: Met. Trans., 1971, vol.2, p.2243.
70. S.J. Matas, R.F. Hehemann: Trans. TMS-AIME, 1961, vol.221,p.179.
71. R.I. Entin: 'Decomposition of Austenite by Diffusional Processes', p.295, Interscience Pub., New York, 1962.
72. T. Lyman, A.R. Troiano: Trans. AIME, 1945, vol.162, p.196.
73. T. Lyman, A.R. Troiano: Trans ASM, 1946, vol. 37, p.402.
74. A.T. Davenport: AIME Abstracts - 5th Annual Spring Meeting, University of Pennsylvania, 1973.
75. E.R. Parker: Met. Trans., 1977, vol.8A, p.1025.
76. S.V. Radcliffe, M. Schatz: Acta Met., 1962, vol.10, p.201.
77. N. Ridley, H. Stuart, L. Zwell: Trans. TMS-AIME, 1969, vol. 245, p.1834.
78. R.C. Ruhl, M. Cohen: Trans. TMS-AIME, 1969, vol. 245, p.241.
79. C.S. Roberts: Trans.AIME, 1953, vol.197, p.203.
80. M.G. Lorinski, I.S. Simeonova: Acta Met., 1959, vol.7, p.709.

81. Y. Imai, M. Izumiyama, M. Tsuchiya: Sci. Rept. Res. Inst. Tohoku University, 1965, vol.A17, p.173.
82. D.J. Dyson, B. Holmes: J.I.S.I., 1970, vol.208, p.469.
83. J.M. Moyer, G.S. Ansell: Met. Trans., 1975, vol.6A, p.1785.
84. K.R. Kinsman, E. Eichen, H.I. Aaronson: Met. Trans., 1971, vol.2, p.346.
85. K.J. Irvine, D.T. Llewellyn, F.B. Pickering: J.I.S.I., 1961, vol. 199, p.153.
86. L. Norstrom: Scand. J. of Met., 1976, vol.5, p.159.
87. R.G. Davies: Met. Trans., 1979, vol.10A, p.113.
88. W.C. Leslie, A.S. Keh:'Mechanical Working of Steel II', pp.337-377, Gordon and Breach, New York, 1965.
89. E.R. Petty (Ed.): 'Martensite -- Fundamentals and Technology', Longmans, 1970.
90. T.K. Sanyal, R. Brook: Metal Science, 1975, vol. 9, p.135.
91. R.M. Horn, R.O. Ritchie: Met. Trans., 1978, vol.9A, p.1039.
92. G. Thomas: Met. Trans., 1978, vol.9A, p.439.
93. A.H. Cottrell: TMS - AIME, 1958, vol.202, p.192.
94. B.Uhrenius: Scand. J. Met., 1973, vol.2, p.177.
95. T. Wada, H. Wada, J.F. Elliott, J. Chipman: Met. Trans., 1977, vol.2, p.2199.
96. G.R. Chanani, S.D. Antolovich, W.W. Gerbriech: Met. Trans., 1972, vol.3, p.2661.
97. C.S. Roberts: Trans. AIME, 1953, vol.199, p.203.
98. J. McMahon, G. Thomas: 'Microstructure and Design of Alloys', vol.1, 1974, p.180, London (Metals Society).
99. B.V.N. Rao, G. Thomas: Int. J. Fracture, 1977, vol.13, p.705.
100. J.E. King, R.F. Smith, J.F. Knott: Fracture 77, vol.2, ICF4, Waterloo, Canada, 1977, pp.279 - 286.
101. R.A. Clark, G. Thomas: Met. Trans., 1975, vol.6, p.969.
102. J.E. King, R.F. Smith, J.F. Knott: Int. J. Fracture, 1977, vol.13, p.877.
103. U.H. Lindborg, B.L. Averbach: Acta Met., 1966, vol.14, p.1583.
104. R.E. Dolby, J.F. Knott: J.I.S.I., 1972, vol.210, p.857.
105. J.P. Naylor, P.R. Krahe: Met. Trans., 1975, vol.6A, p.594.
106. A.L.T. Azevedo, E.G. DaSilva: Scripta Met., 1978, vol.12, p.113.
107. N.C. Law, D.V. Edmonds, P.R. Howell: Unpublished research, University of Cambridge, England.
108. J.C. Bokros, E.R. Parker: Acta Met., 1963, vol.11, p.1291.
109. M. Shibata, K. Ono: Acta Met., 1975, vol.23, p.587.
110. G.V. Kurdjumov, G. Sachs : Z. Phys., 1930, vol.64, p.325.

111. A.B. Greninger, A.R. Troiano: Trans. AIME, 1949, vol.185, p.590.
112. Z. Nishiyama: Sci. Rept., Tohoku Univ., 1934, vol.23, p.325.
113. M. Watnabe, C.M. Wayman: Met. Trans., 1971, vol.2, p.2229.
114. J.S. Bowles, J.K. Mackenzie: Acta Met., 1954, vol.2, p.224.
115. G.R. Speich, P.R. Swann: J.I.S.I., 1965, p.480.
116. C.M. Wayman: 'Introduction to the Crystallography of Martensite Transformations', 1964, the Macmillan Co., New York.
117. P.M. Kelly: Acta Met., 1965, vol.13, p.635.
118. G. Thomas: Iron and Steel International, 1973, vol.46, p.2267.
119. B.V.N. Rao, R.W. Miller, G. Thomas: Proc. Int. Conf. Heat Treatment, 1976, the Metals Society, London.
120. D.P. Dunne, C.M. Wayman: Met. Trans., 1971, vol.2, p.2327.
121. A. Sauveur, C.H. Chou: Trans. AIME, 1929, vol.84, p.350.
122. R.F. Mehl, C.S. Barrett, D.W. Smith: Trans. AIME, 1933, vol.105, p.215.
123. R.F. Mehl, D.W. Smith: Trans. AIME, 1934, vol.113, p.203.
124. A.B. Greninger, A.R. Troiano: Trans. AIME, 1940, vol.140, p.307.
125. C.M. Wayman, C.J. Altstetter: Acta Met., 1962, vol.10,p.992.
126. J.S. Bowles: Acta Cryst., 1951, vol.4, p.162.
127. P.M. Kelly, J. Nutting: JISI, 1961, vol.197, p.199.
128. R. Lagneborg: Acta Met., 1964, vol.12, p.823.
129. P.M. Kelly: Acta Met., 1965, vol.13, p.635.
130. T. Bell, W.S. owen: JISI, 1967, p.428.
131. M.G.D. Biswas, I. Codd: JISI, 1968, p.494.
132. F.J. Schoen, J.C. Nilles, W.S. Owen: Met. Trans., 1971, vol.2, p.2489.
133. B.G.Byrans, T. Bell, V.M. Thomas: 'The Mechanism of Phase Transformations in Crystalline Solids', Institute of Metals Monograph 33, 1968, p.181, london.
134. P.G. McDougall: ISI Spec. Rept. 93, 1965, p.164.
135. J.M. Chilton, C.J. Barton, G.R. Speich: JISI, 1970, p.184.
136. B.I. Bozic, R.I. Lucic: Met. Sci. J., 1977, vol.12, p.751.
137. D.S. Sarma, J.A. Whiteman, J.H. Woodhead: Met. Sci. J., 1976, vol.10, p.391.
138. J.D. Bolton, E.R. Petty: Met. Sci. J., 1971, vol.5, p.166.
139. A.G. Crocker, F. Heckscher, M. Bevis: Phil. Mag., 1963, vol.8, p. 1863.
140. T.J. Patrician, H.M. Ledbetter, R.P. Reed: Met. Trans., 1973, vol.3, p.947.

141. R.G. Davies, C.L. Magee: Met. Trans., 1971, vol.2, p.1939.
142. S.K. Das, G. Thomas: Trans. ASM, 1969, vol.62, p.659.
143. G. Thomas, S.K. Das: JISI, 1971, vol.209, p.801.
144. M. Raghavan, G. Thomas: Met. Trans., 1971, vol.2, p.3433.
145. K.H. Khan, W.E. Wood: Met. Trans., 1978, vol.9A, p.899.
146. M. Bevis, P.C. Rowlands, A.F. Acton: Trans. TMS-AIME, 1968, vol.242, p.1555.
147. R. Clark, G.B. Craig: Prog. in Metal Phys., 1952, vol.3, p.115.
148. M.S. Rashid: SAE Preprint 760206, Feb.1976.
149. M.S. Rashid: SAE Preprint 770211, Feb. 1977.
150. P.E. Repas: Seminar on Vanadium Cold Pressing and Dual-Phase Steels, Paper no.2, 1978, West Berlin, Vanitec.
151. R.G. Davies, C.L. Magee: ibid., paper no.3.
152. R.G. Davies: Met. Trans., to be published.
153. R.G. Davies: 'On the Ductility of Dual-Phase Steels', Ford Motor Co., Dearborn, Michigan.
154. R.G. Davies: Met. Trans., 1978, vol.9A, p.451.
155. R.G. Davies: Met. Trans., 1978, vol.9A, p.41.
156. S.T. Mileiko: J. Mat. Sci., 1969, vol.4, p.974.
157. R. Lagneborg: Seminar on Vanadium Cold Pressing and Dual-Phase Steels, Paper no. 5, 1978, West Berlin, Vanitec.
158. Y. Tomota, K. Kuroki, T. Mori, I. Tamura: Mat. Sci. & Eng., 1976, vol.24, p.84.
159. J.M. Cowley: p.27, 'Practical Aspects of Electron Microscopy and Microbeam Analysis', Ed. B.M. Siegel, John Wiley and Sons, 1975.
160. W.D. Riecke: 'Electron Microscopy in Materials Science', 3rd Course of the International School of Electron Microscopy, Eltove Majorana, Int. Centre for Scientific Culture, Eds. V. Valdre, E. Rvedi, 1975, p.81.
161. J.G. Humphreys, W.S. Owen: JISI, 1961, vol.198, p.38.
162. P. Schwaab: Naturwiss: 1954, vol.51, p.356.
163. J. Pomey: Mem. Sci. Rev. Metallug., 1966, vol.63.6, p.509.
164. K.H. Jack: JISI, 1949, vol.163, p.384.
165. 'A Handbook of Lattice Spacings and Structures of Metals and Alloys', 1967, vol.2, p.1339, Pergamon Press.
166. G. Konoval, L. Zwell, L.A. Gorman, W.C. Leslie: Nature, 1959, vol.184, p.1862.
167. N.S. Owen, B.G. Street: JISI, 1962, vol.172, p.15.
168. J.M. Schissler, J. Arnould, G. Metauer: Mem. Sci. Rev. Metallug., 1975, p.779.

169. J.W. Christian: ICOMAT 79, June 1979, Boston, in press.
170. B. Lee, S. Millman, I.L. MacDougall, S.R. Keown, B.B. Argent Metal Science, 1977, vol.7, p.261.
171. J.W. Christian: Private Communication, July 1979.
172. M. Kehoe, P.M. Kelly: Scripta Met., 1970, vol.4, p.473.
174. B.B. Argent: Metal Science, 1976, vol.10, p.409.
175. R.A. Grange, H.M. Stewart: Trans. AIME, 1946, vol.167, p.467.
176. Y. Imai, M. Izumiyama, M. Tsuchiya: Sci. Rep. Res. Inst. Tohoku Univ., 1965, vol.A17, p.173.
177. T. Bell, W.S. Owen: TMS-AIME, 1967, vol.239, p.1944.
178. B.B. Argent: Private Communication, July 1979.
179. J.T. Moore, D. Kuhlman-Wilsdorf: Proc. 2nd Int. Conf. on Strength of Materials, ASM, 1970, p.484.
180. A. Seeger, H. Kronmuller: Phil. Mag., 1962, vol.7, p.897.
181. J.E. Bailey, P.B. Hirsch: Phil. Mag., 1960, vol.5, p.485.
182. R.L. Patterson, C.M. Wayman: Acta Met., 1966, vol.14, p.347.
183. R.L. Patterson, C.M. Wayman: Acta Met., 1964, vol.12, p.1306.
184. M. DeChamps, L.M. Brown: Acta Met., 1979, vol.27, p.1281.